Contactless control of offshore wind turbines during installation
A motion control technique based on magnetic interaction

Atzampou, P.

DOI
10.4233/uuid:8fd5f93a-7ab5-4228-8f58-cf0c4c6f9ff5

Publication date
2025

Document Version
Final published version

Citation (APA)
Atzampou, P. (2025). *Contactless control of offshore wind turbines during installation: A motion control technique based on magnetic interaction*. [Dissertation (TU Delft), Delft University of Technology]. https://doi.org/10.4233/uuid:8fd5f93a-7ab5-4228-8f58-cf0c4c6f9ff5

Contactless control of offshore wind turbines during installation

A motion control technique based on magnetic interaction

Panagiota Atzampou

Contactless Control of Offshore Wind Turbines during Installation

A MOTION CONTROL TECHNIQUE BASED ON MAGNETIC INTERACTION

Contactless Control of Offshore Wind Turbines during Installation

A MOTION CONTROL TECHNIQUE BASED ON MAGNETIC INTERACTION

Dissertation

for the purpose of obtaining the degree of doctor
at Delft University of Technology
by the authority of the Rector Magnificus, Prof.dr.ir. T.H.J.J. van der Hagen,
chair of the Board for Doctorates
to be defended publicly on
Monday 15th of September 2025 at 12:30 pm

by

Panagiota ATZAMPOU

This dissertation has been approved by the

promotor: Prof.dr. A.V. Metrikine
promotor: Dr.ir. A. Tsouvalas
copromotor: Dr.ir. P.C. Meijers

Composition of the doctoral committee:

Rector Magnificus,	chairperson
Prof.dr. A.V. Metrikine,	Delft University of Technology, promotor
Dr.ir. A. Tsouvalas,	Delft University of Technology, promotor
Dr.ir. P.C. Meijers,	Delft University of Technology, copromotor

Independent members:

Prof.dr.ir. A.C. Viré	Delft University of Technology, Netherlands
Prof.dr. J. Awerejcewicz	Lodz University of Technology, Poland
Prof.dr. E. Pavlovskaia	University of Aberdeen, Scotland
Prof.dr. T. Insperger	Budapest University of Technology & Economics, Hungary
Prof.dr.ir. S.N. Jonkman	Delft University of Technology, reserve member

This work is part of the research programme DOT6000-FOX, which is (partly) financed by the Rijksdienst voor Ondernemend Nederland (RVO) under the grant number TEHE119004.

Keywords: non-contact control, magnet-to-magnet interaction, magnetic pendulum, active vibration control, motion compensation, magnetically-induced damping, motion control, magnetic stiffness, PID control, offshore wind turbine installation

Printed by: Uitgeverij U2pi BV. - The Hague

Front & Back: *Aurora Borealis Labradorescence* design by P. Atzampou using A.I.

ISBN

"Now is the time to understand more,
so that we may fear less."
–Marie Curie

Για σένα, Λ.Κ

Contents

Summary

The increasing demand for renewable energy is driving a significant rise in the adoption of offshore wind energy as a formidable means of energy harvesting. To enhance efficiency and reduce the cost of electricity, offshore wind turbines (OWTs) and their supporting structures are being designed with larger dimensions, necessitating installation in deeper waters. These installations are carried out using floating heavy lift vessels, which, however, have the disadvantage of transferring wave-induced motions to the payload, resulting in undesired vibrations of the latter.

A variety of motion compensation and position control techniques have been developed and tested over the years. These include gripper frames for monopiles, as well as manually operated, passive, or active tugger line systems designed to maintain the correct position of suspended OWT components. Indirect methods, such as crane motion control through cart manipulation and heave compensation, have also been implemented to manage motion during installation. However, all these approaches rely on direct contact between mechanical equipment and the payload, often requiring human intervention. These limitations, compounded by the strict error tolerances for installation and the challenging offshore environment, underscore the need for a contactless position control technique for OWT installation.

This thesis introduces the development of a contactless motion control technique for suspended loads during offshore wind turbine installations, providing the groundwork for a novel alternative to customary industry methods. The proof-of-concept is built upon numerical simulations of the interaction between the dynamical system and the contactless controller, complemented by partial validation through scaled laboratory experiments. The investigated concept leverages magnetic interaction, utilising a magnet affixed to the suspended component and an electromagnetic actuator to achieve precise motion control.

Given the complexity of the full-scale system, this research adopts a comprehensive step-wise methodology to effectively devise the new control method. The envisioned full-scale dynamical system is modelled through a series of incremental systems, each acting as a simplified yet analogous representation of the original. These incremental systems are specifically designed to validate the potential of the contactless motion control method, focusing on a reduced number of degrees of freedom in each step to systematically address the challenges of the complete system.

The first two chapters introduce the theoretical foundation of the dynamics and control of the initial incremental model, specifically the lab-scale planar point mass pendulum with moving support. The magnetic interaction is modelled as a dipole-to-dipole interac-

tion, representing the simplest unit to describe the magnetic field geometry. A PID controller is utilized to control this interaction. Numerical simulations are validated against experimental measurements of the forced vibrations, where the electromagnetic actuator excites the system using an alternating harmonic signal. The model demonstrates high predictive accuracy, with minor discrepancies attributed to friction at the pendulum pivot and operational limits of the electromagnet, which can introduce delays and saturation.

A dedicated chapter delves into the controlled response of the planar magnetic pendulum, which is excited by the kinematically prescribed motion of its pivot and controlled via an electromagnetic actuator. Two control modes are explored: enforcing a desired motion with a fixed pivot point and maintaining a fixed global position despite a moving pivot point. Key control parameters are identified as the separation distance between the magnets and the saturation limits of the controller. Performance improves significantly when the magnets operate in close proximity, resulting in reduced errors and less saturation. In the desired motion mode, the system exploits resonance, while the disturbance rejection mode successfully mitigates the unwanted escalation of oscillations. However, the transient response proves more critical in the latter mode, showing the highest error values and saturation levels.

Another critical degree of freedom involves rotation around the vertical axis of the mass (shaft). This vibration mode is modelled as a single-degree-of-freedom magnetic ring, free to rotate around its centre, interacting with an external electromagnetic actuator. The control parameter is the orientation of the magnetic field of the external dipole, fluctuating around a fixed angle with a defined step. A control rule is developed to adjust this fluctuation, enabling the enforcement of a desired motion through various control modes. These include dissipating rotational vibrations via magnetically induced damping and actively controlling rotation. The controller effectively establishes a new equilibrium for the system and introduces magnetic damping that mimics Coulomb friction. An additional crucial parameter is introduced to the control strategy: the ratio of the system's inherent stiffness to the magnetically imposed stiffness.

The next incremental system is designed to address the coupled dynamics and simultaneous control of multiple vibration modes–translational and rotational vibrations– integrating the insights gained from the preceding chapters. This system enhances the lab-scale magnetic pendulum by introducing a rotational degree of freedom around its shaft (longitudinal axis). The equilibrium position of the system depends on both the magnetic interaction and the global position of the suspended mass during the planar motion. The role of the translational actuator is twofold: controlling the planar vibrations and compensating for the attractive forces generated by the magnets involved in the torsional control. Furthermore, this model is more sensitive to instability requiring two actuators of equivalent magnetic field magnitude. In short, the success of the combined control is attributed to the translational actuator's ability to control the separation distance between the interacting magnets.

The concluding chapter presents a full-scale numerical model designed for controlling a suspended OWT tower during installation by a floating vessel. An exemplary control arrangement is devised leveraging the control strategies established in this work. To satisfy the controllability requirements and ensure control efficiency, three actuators are employed: one dedicated to torsional control and two to translational control, strategically positioned along the cylinder's height. The control mode focuses on disturbance rejection, addressing both non-trivial initial conditions and crane tip motion. The system effectively dissipates both planar and torsional rotations, maintaining minimal error relative to the desired reference. Key performance factors include precise tuning of the PID gains and strategic placement of magnet pairs to generate sufficient control torques for different vibrational modes. Notably, the required magnetic forces are comparable to or less than those of conventional tugger line systems, highlighting the feasibility and efficiency of the proposed novel alternative.

The present thesis methodically develops a proof-of-concept contactless motion control technique, utilising non-contact attractive and repulsive forces to enhance the controllability of suspended loads, thereby improving safety and precision during offshore wind turbine installations.

Samenvatting

De toenemende vraag naar groene energie zorgt voor een aanzienlijke groei in het gebruik van offshore windenergie als de methode voor energieopwekking. Om de efficiëntie te verhogen en de kosten van de opgewekte elektriciteit te verlagen worden offshore windturbines (OWT's) en hun funderingen ontworpen met grotere afmetingen, wat installatie in dieper water noodzakelijk maakt. De installatie van dergelijke constructies wordt uitgevoerd met drijvende kraanschepen. Deze schepen hebben echter als nadeel dat ze golfgeïnduceerde bewegingen overbrengen op de last, wat leidt tot ongewenste schommelingen.

Door de jaren heen zijn er verschillende technieken ontwikkeld en getest voor bewegingscompensatie en positieregeling. Hiertoe behoren grijpers voor monopiles, maar ook handmatig bediende, passieve of actieve tuggersystemen. Tuggersystemen zijn ontworpen om de juiste positie van hangende OWT componenten te garanderen. Indirecte methoden zijn eveneens toegepast om beweging tijdens de installatie te beheersen. Voorbeelden hiervan zijn deiningscompensatie en een kraanbewegingsregelaar, die de beweging van de last beheerst door middel van wagenmanipulatie. Al de genoemde benaderingen berusten echter op direct contact tussen mechanische apparatuur en ook zijn er menselijke handelingen nodig. Deze beperkingen, gecombineerd met de strikte fouttoleranties voor installatie en de uitdagende offshore omstandigheden, benadrukken de noodzaak van een contactloze positioneringstechniek voor OWT installatie.

Dit proefschrift introduceert een contactloze bewegingsregelingstechniek voor hangende lasten tijdens het installeren van offshore windturbines. Het vormt daarmee de basis voor een nieuw alternatief voor de methoden die nu gangbaar zijn in de industrie. Het proof-of-concept is gebaseerd op numerieke simulaties van de interactie tussen het dynamische systeem en de contactloze regelaar, aangevuld met gedeeltelijke validatie via geschaalde laboratoriumexperimenten. Het onderzochte concept maakt gebruik van magnetische interactie, waarbij een magneet is bevestigd aan het hangende onderdeel en een elektromagnetische actuator wordt ingezet voor nauwkeurige bewegingsregeling.

Gezien de complexiteit van het systeem op ware grootte hanteert dit onderzoek een stapsgewijze methodologie om de nieuwe regelmethode effectief te ontwikkelen. Het beoogde dynamische systeem wordt gemodelleerd via een reeks incrementele systemen, die elk een vereenvoudigde maar waarheidsgetrouwe representatie van het origineel zijn. Deze incrementele aanpak is specifiek ontworpen om de contactloze bewegingsregeling te valideren. Hierbij wordt in elke stap gefocust op een beperkt aantal vrijheidsgraden om systematisch de uitdagingen van het volledige systeem te doorgronden.

De eerste twee hoofdstukken behandelen de theoretische basis van de dynamica en regeling van het eerste incrementele model, namelijk een geïdealiseerde slinger met een bewegend ophangingspunt op een laboratoriumschaal. De magnetische interactie wordt gemodelleerd als een dipool-dipool interactie. Dit is de eenvoudigste eenheid is om het magnetische veld te beschrijven. Vervolgens wordt een PID-regelaar gebruikt om deze interactie te regelen. Numerieke simulaties worden gevalideerd aan de hand van experimentele metingen van de gedwongen trillingen van de slinger, waarbij de elektromagnetische actuator het systeem aandrijft met een wisselend harmonisch signaal. De voorspellingen van het wiskundige model komen goed overeen met de metingen. De kleine afwijkingen tussen het model en het experiment kunnen worden toegeschreven aan wrijving bij het draaipunt van de slinger en operationele beperkingen van de elektromagneet, zoals vertraging in het signaal en verzadiging van de magneet.

Een apart hoofdstuk behandelt de gecontroleerde respons van dezelfde magnetische slinger. De slinger wordt geëxciteerd door een voorgeschreven beweging van het ophangpunt en wordt geregeld via een elektromagnetische actuator. Twee regelmodi worden onderzocht: het afdwingen van een gewenste beweging met een vast ophangpunt, en het behouden van een vaste globale positie bij een bewegend ophangpunt. Belangrijke regelparameters zijn de afstand tussen de magneten en de verzadigingslimieten van de magneet. De prestaties verbeteren aanzienlijk wanneer de magneten dichter bij elkaar worden gebracht. Dit leidt tot een kleinere fout en minder verzadiging. Als de beweging van de massa wordt voorgeschreven, dan benut het regelsysteem resonantie. Terwijl wanneer de bewegingen onderdrukt moeten worden de regelaar voorkomt dat de amplitude van de oscillatie toeneemt. In het laatste geval blijkt de overgangsrespons echter kritisch met de hoogste foutwaarden en verzadigingsniveaus.

Een andere kritieke vrijheidsgraad betreft de rotatie rond de verticale as van de massa. Deze trillingsmodus wordt gemodelleerd als een magnetische ring met een enkele vrijheidsgraad. Deze ring kan vrij draaien rond zijn middelpunt en wordt beïnvloed door de externe elektromagnetische actuator. In dit geval is de regelparameter de oriëntatie van het magnetische veld van de externe dipool. Deze fluctueert rond een vooraf bepaalde hoek met een gedefinieerde stapgrootte. Er wordt een regelwet ontwikkeld om deze fluctuatie dusdanig aan te passen dat een gewenste beweging kan worden afgedwongen voor de twee regelregimes. Deze omvatten het dempen van rotatietrillingen via magnetisch geïnduceerde demping en het actief voorschrijven van de rotatie. De regelaar stelt effectief een nieuw evenwicht voor het systeem vast en introduceert magnetische demping die vergelijkbaar is met het effect van Coulomb wrijving. Een cruciale parameter in de regelstrategie is de verhouding tussen de inherente stijfheid van het systeem en de magnetisch opgelegde stijfheid.

Het volgende incrementele systeem is ontworpen om de gekoppelde dynamica en gelijktijdige regeling van meerdere trillingsmodi – translatie en rotatie – te analyseren. Hierbij worden de inzichten uit de voorgaande hoofdstukken gecombineerd. In dit systeem wordt aan de magnetische slinger een rotatievrijheidsgraad toegevoegd. Deze rotatie is rond de as van de slinger. In dit geval hangt de evenwichtspositie van het systeem af van zowel de magnetische interactie als de globale positie van de hangende massa tijdens de beweging in een vlak. Hierbij is de rol van de translationele actuator tweeledig: het regelen van de trillingen in het vlak en het compenseren van de aantrekkingskrachten die worden gegenereerd door de magneten die betrokken zijn bij de torsieregeling. Hierdoor is dit model gevoeliger voor instabiliteit. Ter stabilisatie is het nodig dat twee actuatoren met een gelijkwaardige magnetische veldsterkte worden gebruikt. Al met al wordt het succes van de gecombineerde regeling bepaald door het vermogen van de translationele actuator om de afstand tussen de magneten te regelen.

Het laatste hoofdstuk behandelt een numeriek model dat de bewegingen beschrijft van een hangende OWT-toren tijdens installatie met behulp van een drijvend schip. De afmetingen van de toren zijn nu op ware grootte. Op basis van het werk uit de voorgaande hoofdstukken wordt voor dit geval een illustratieve regelconfiguratie opgesteld. Om aan de regelbaarheidsvereisten te voldoen en de efficiëntie te waarborgen worden drie actuatoren gebruikt: één voor torsie en twee voor translatie. Deze actuatoren worden strategisch geplaatst langs de hoogte van de cilinder. De regelingsstrategie richt zich op verstoringsonderdrukking waarbij zowel niet-triviale beginvoorwaarden als kraanbewegingen aan de top worden meegenomen. Het systeem dempt effectief zowel bewegingen in het vlak als rotaties, met minimale afwijking ten opzichte van de gewenste referentie. Belangrijke prestatiefactoren zijn de nauwkeurige afstemming van de PID-coëfficiënten en de strategische plaatsing van magneetparen om voldoende moment te genereren voor verschillende trillingsmodi. Opmerkelijk is dat de vereiste magnetische krachten vergelijkbaar zijn met of lager liggen dan die van conventionele tuggersystemen. Dit onderschrijft de haalbaarheid en efficiëntie van het voorgestelde nieuwe alternatief.

Dit proefschrift ontwikkelt stapsgewijs een proof-of-concept van een contactloze bewegingsregelingstechniek voor offshore toepassingen. Hierin wordt gebruik gemaakt van contactloze aantrekkende en afstotende krachten om de regelbaarheid van hangende lasten te verbeteren. Zo wordt de veiligheid en precisie tijdens de installatie van offshore windturbinecomponenten vergroot.

Preface

This thesis chronicles my initiation into the scientific realm of energy, frequency, and dynamics; the very language of the universe (Nikola Tesla, 1856–1943). Along this journey, I delved into one of nature's most powerful yet unseen forces: magnetism, an omnipresent wonder shaping our world. In doing so, I found myself echoing the belief of Thales of Miletus (c.626/623 – 548/545 BC) that magnets, with their ability to move iron, might possess a kind of life force or animating principle—a notion that resonated deeply with my own animistic perspective. This seemingly telepathic and telekinetic phenomenon is harnessed here as a means of contactless control over the motion of a suspended load.

To develop the proposed technique, I turned to a problem that is deceptively simple yet profoundly intricate—the pendulum, a system that has captivated and perplexed minds for centuries. With due reverence to Galileo Galilei (1564–1642) and the local Christiaan Huygens (1629–1695)—who might well stir in their graves at yet another pendulum study—I found myself oscillating, both literally and figuratively, through countless pendulum configurations, utterly hypnotised by the richness of their dynamics. The pendulum stands as a cornerstone not only in understanding dynamics but also in exploring the control of motion. Naturally, a perfectionist spirit like mine could not resist the urge to impose control upon yet another facet of my life. In this endeavour, I can only hope for success—but I will leave that for the reader to decide.

This work sits at the vent diagram intersection of dynamics, control, and magnetism, crafted to ignite curiosity in a novel, out-of-the-box concept—for what is a truly novel idea if not a fusion of a seemingly unorthodox science-fiction approach? At its core, it investigates magnet-to-magnet interactions for controlling suspended loads, with a targeted application in offshore wind turbine installations.

Dear reader, thank you for your time and attention. Like another Sisyphus, I invite you to accompany me in the steady ascent—pushing the boulder of thought and inquiry uphill, toward a new summit where knowledge gathers a higher potential (Figure 1). My hope is that these pages not only present my findings, but also ignite your curiosity and imagination, drawing you in with an irresistible attractive force...

Panagiota Atzampou
Delft, August 2025

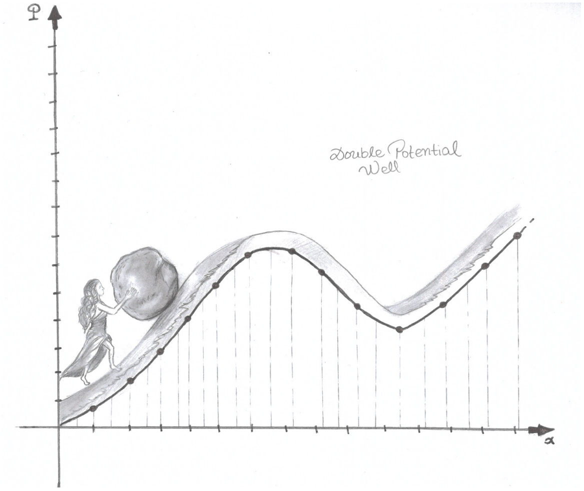

Figure 1: A journey to higher potential.

1

Introduction

The ominous effects of climate change and the subsequent ecological hazards posed by the over-reliance on fossil fuel as the main energy source have driven a paradigm shift towards sustainable and environmentally-conscious energy sources [1]. Renewable energy technology exploits the limitless energy capacity of various natural resources by converting them into useful energy forms, e.g. using mechanical energy to generate electricity [2]. Moreover, renewable sources are strongly coupled with sustainable development as they pertain to energy harvesting from resilient and inexhaustible resources [3].

One of the most promising renewable energy alternatives is wind energy, which stands out due to its social, technical, economic, and environmental advantages [4, 5]. In particular, offshore wind turbines (OWTs) have gained substantial attention and investment over the past decades, owing to the significant energy potential available in the extensive global offshore areas [6]. The open waters facilitate the installation of larger and more numerous turbines per wind park, capitalizing on wind resources that are less turbulent and possess higher energy content compared to their onshore counterparts [7]. Additionally, offshore wind is known for its robustness and consistency, with typical fluctuations remaining within a narrow band, up to 20 % from hour to hour [8]. OWTs are deployed at a minimum distance of 10 km from the shore or at least in 10 m water depth [9], thus eliminating the concern of visual disamenity and auditory nuisance. Strict regulatory constraints regarding land use, wind turbine and farm size that often burden onshore installations are typically less restricting offshore. Furthermore, offshore wind farms (OWFs) can benefit marine ecosystems by acting as artificial reefs, increasing biodiversity and complexity of the benthic and pelagic habitats [10].

Naturally, as an anthropogenic intervention, the deployment and operation of OWFs can also pose environmental challenges [10–12]. Underwater noise generated during the installation phase, particularly monopile driving for bottom-founded OWTs, has direct or indirect negative impacts on several marine fauna species [10]. Mitigation efforts focus on reducing noise pollution through alternative pile driving methods [13] or noise mitigation systems [14]. During operation, electromagnetic fields emitted by cables can interfere with the navigation and orientation of marine animals that rely on geomagnetic cues and can cause local temperature rises, affecting benthic communities [10, 11]. Research is conducted to investigate possible measures to dissipate the EMF radiation exposure by increasing the cable burial depth [15]. Despite these localized environmental impacts that can be reversed to an extent, the global benefits offered by OWFs are substantial and contribute significantly towards the reduction of greenhouse gas emissions and climate change mitigation.

The *Paris Agreement* (2015) is a legally binding international treaty on climate change that aims at limiting global warming to an utmost temperature increase of 1.5°C above pre-industrial levels [16]. This agreement focuses on achieving a global balance between anthropogenic emissions (sources and sinks) of greenhouse gases, so-called net-zero emissions, in the second half of this century. Towards that goal, according to the *European Green Deal*, the European Union (EU) aspires to become the first climate-neutral continent by 2050, setting an exemplary path towards energy transition [17]. The EU has set the strongest ambitions for offshore wind energy, with targets for individual member states to install a total capacity of 29 GW of new offshore wind turbines by 2025 [18]. According to the Offshore Wind Outlook report by the International Energy Agency (IEA) [8], in the Stated Policies Scenario (STEPS, based on the current policy landscape), the EU accounts for nearly 40% of the global offshore market (GL) by 2040, increasing its installed capacity to almost 130 GW (Figure 1.1a). In the Sustainable Development Scenario (SDS, in accordance with the goals of the Paris Agreement), the European Union's offshore installed capacity increases by almost 40% relative to the STEPS, reaching 175 GW by 2040 to promote decarbonisation.

The envisioned robust growth of offshore wind energy in Europe can be facilitated by its enormous technical wind potential, which amounts to approximately 50 000 TWh per year. The global electricity demand is expected to increase significantly from 25 000 to a range of 52 000 to 71 000 TWh by 2050, driven by the growth in energy needs and the widespread electrification of various economic sectors worldwide [19]. With this potential, Europe could significantly contribute to meeting the future global demand solely through offshore wind energy exploitation (Figure 1.1b).

Thus, to meet the environmental goals and satisfy the ever-increasing energy demands, OWTs are installed in deeper waters with greater capacities and, hence, larger dimensions [9] (Figure 1.2). Consequentially, this increase in scale presents a unique set of engineering challenges to installation operations [20].

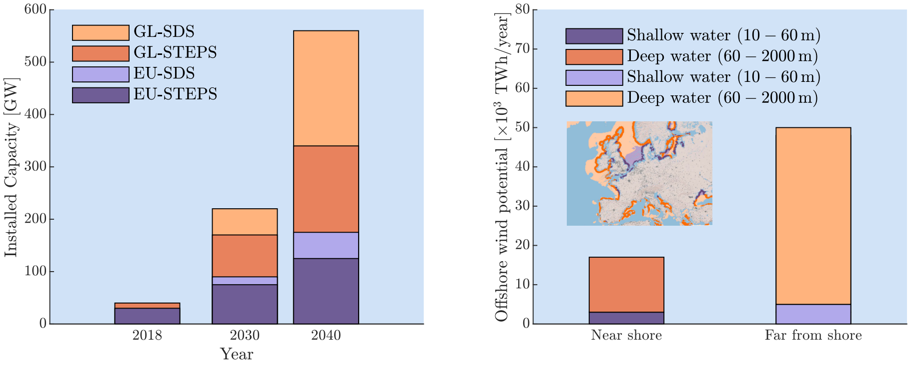

(a)

(b)

Figure 1.1: (a) Installed capacity of offshore wind on global (GL) and European (EU) scale for two scenarios: Stated Policies Scenario (STEPS) and Sustainable Development Scenario (SDS), (b) Annual technical potential for offshore wind in Europe. Near and far from shore regions correspond to distances shorter and greater than 60 km, respectively. Adapted from [8].

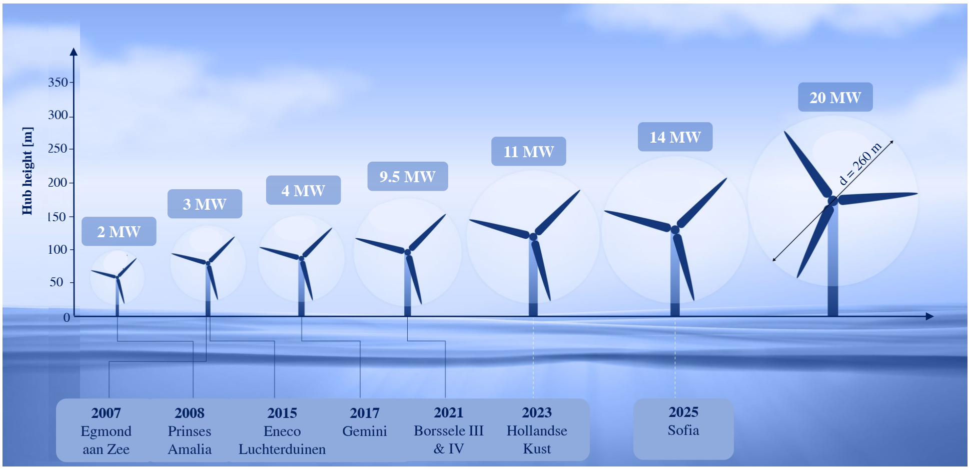

Figure 1.2: Offshore wind turbine size evolution in time. Adapted from [21].

1.1. State of the art in offshore wind turbine installations

A central challenge in offshore wind energy is the installation process, which constitutes a substantial portion of the overall project costs and amounts to a quarter of the overall costs of an OWT deployment [22]. An OWT installation consists of three primary stages according to the structural unit installed [23]:

- **Foundation** Installation procedure depends on the foundation type, either bottom-founded (e.g., monopile installations [24]) or floating, including the transition piece and scour protection;
- **Turbine** Erection of the turbine, either pre-assembled or piece-wise, including the tower, rotor, nacelle, and blades;
- **Transmission equipment** Installation of inner and outer cables to connect the turbine to the offshore substation and the onshore grid.

In order to enhance the appeal and the monetary engagement to OWT deployment project investments, it is imperative to investigate measures to reduce installation costs. This expenditure strongly depends on the efficiency of the operation coupled with the operating constraints imposed by meteorological conditions [12], namely the total duration of a complete and successful OWT installation. Major factors impacting the installation time and workability window include [23, 24]:

- **Installation means**: The capacity and capabilities of means such as vessels and cranes;
- **Installation methods**: The efficiency of methods including the motion control techniques for payload steering.

1.1.1. Offshore wind turbine installation vessels

Jack-up vessels have monopolised the transport and installation of OWTs worldwide [25] (Figure 1.3a). These vessels consist of a buoyant hull with a number of mechanised extendable legs, which are capable of elevating the hull above the sea surface by stationing the vessel on the sea floor [26, 27]. Thus, they ensure a stable working platform for the offshore site even under rough sea conditions [28], limiting the external environmental disturbances to solely wind loads. Jack-up vessels are either towed or self-propelled barges, with the latter, called turbine installation vessels (TIVs), being purposely built for offshore wind farm installations [25]. Despite their advantages, these vessels are constrained by limitations pertaining to the installation depth and lifting capacity [29]. Consequently, an opportunity arises for floating OWT installations.

Different types of floating vessels have been considered for offshore wind turbine installations ([29–31]), with the heavy lift vessels (HLVs) being the most prevalent due to their superior stability, greater load capacity, and enhanced operational flexibility in challenging offshore environments (Figure 1.3b). HLVs, traditionally used in the oil and gas industry [32], can lift loads up to 20 000 tonnes, and thus they are considered well-suited for the deployment of heavy wind turbine assemblies even in demanding installation scenarios [33]. These vessels are often deployed in European offshore wind installation projects to install the foundations, substations, or fully pre-assembled OWTs [23]. Heavy lift vessels fall into two main categories: construction semi-submersibles (primarily used to transport large cargoes); and heavy lift crane vessels (or heavy crane barges to lift cargoes either portside or at offshore locations) [23]. Unlike jack-up vessels, floating installations do not necessitate elevating and retrieving operations, leading to greater time efficiency. To provide an indication, the preloading procedure of Van Oord's jack-up vessel *Aeolus* during the offshore wind turbine installations in the Norther Offshore Wind Farm was estimated to have a duration of approximately 3 hours [34]. HLVs operate on dynamic positioning (DP), which involves maintaining a desirable position by means of control of the vessel's propulsion system [35]. This technology aims to counteract the effects of environmental forces (i.e., waves and currents) on the vessel's position and heading without the requirement for mooring lines [36]. Additionally, the DP system offers the capability to optimize the vessel's orientation to achieve partial wind shielding during the operation.

Given the floating nature of the installation, however, the crane-payload-vessel system remains susceptible to the adverse offshore environment. During the lifting, transporting and assembling stages of the OWT installation, the components are suspended by the crane. Hence, they can oscillate due to direct exposure to wind loads as well as indirect excitation by the wave and current loads on the vessel [37, 38]. The latter excitation is of primary importance for the payload motion [38, 39]. Figure 1.4 illustrates the linear and rotational degrees-of-freedom (DOFs) of the motion of a floating heavy-lift vessel in the sea, which can be translated to crane tip motions, and thus external excitation of the suspended load. Any form of excessive oscillations of the payload are deemed undesirable for such high precision installation operations (alignment of joints during assembly, e.g. bolted flange joints between the suspended tower and the stationary foundation pile), exacting a toll on the overall efficiency [40, 41].

1.1.2. Motion control of suspended loads during offshore installations

In order to subdue the disturbances, a plethora of motion compensation and position control techniques has been employed during OWT installations and has been thoroughly tested *in situ* over the years. These techniques can be classified into two categories:

- **Direct motion control**: The actuation forces are applied on the suspended load directly;
- **Indirect motion control**: The motion attenuation is realized by modifying the parameters or controlling sub-components of the dynamical system.

(a) (b)

Figure 1.3: (a) Jack-up vessel (Van Oord-*Aeolus*) installing an offshore wind turbine with the capacity of 8 MW [42]. (b) Semi-submersible crane vessel (HMC-*Sleipnir*) performing a floating offshore installation [43].

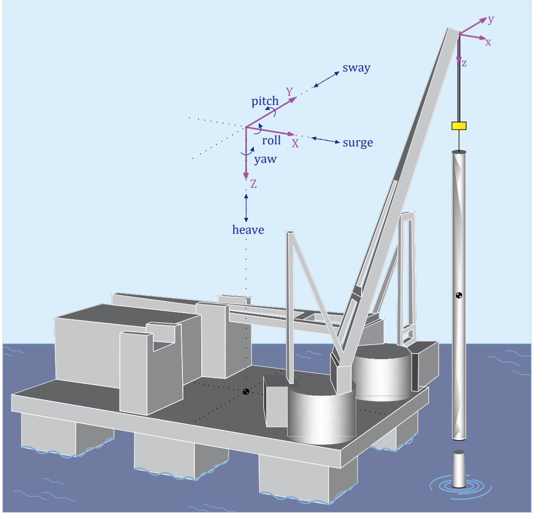

Figure 1.4: Heavy lift vessel linear and rotational motions in the sea. The schematic is inspired by the semi-submersible vessel *Prometheus* designed by Domingos D.F. [44].

Depending on the different components and stages of the installation operation, different techniques are employed. For bottom-founded OWT installations, fixed and motion compensating gripper frames (Figure 1.5a) are considered ubiquitous [33]. To maintain the correct position of a hanging load during the lift or transportation to the installation target, manually manipulated tugger lines attached to the component or active tugger line motion control systems are utilized [45]. Tugger lines are ropes, typically made of steel or synthetic materials, designed to exert purely attractive forces. They require a control tension to prevent slack, ensuring they remain taut and effective. Tugger lines are extensively used in vibration attenuation by controlling key parts of the system, such as the hook block (Figure 1.5b), or to steer the motion of various OWT components during installation, including blades (Figure 1.5c) and the turbine tower (Figure 1.5d).

Alternatively, the motion compensation of the payload has also been introduced indirectly by means of motion control of the crane itself. These methods frequently pertain to the attenuation of the vessel motions through a motion-compensated platform (with limitations on the lifting capacity) [46], crane cart motion manipulation [47] and crane parameter modification to minimize payload pendulation [48].

For floating heavy-lift vessels, horizontal wave-induced motions (surge and sway, see Figure 1.4) are primarily counteracted by the dynamic positioning system. To decouple the undesirable vertical vibration of the payload caused by vertical excitation—whether due to the motion of the floating vessel or during the lift operations—heave compensation systems (HCs) are employed [25, 49]. In principle, heave compensation electronically monitors the vessel's vertical movement and automatically controls the crane winch to counteract this motion. The crane cable is continuously adjusted to keep the payload hovering above the desired installation target. The operator can superimpose command signals on the automatic function, allowing precise control of slow and accurate movements relative to the target [25]. HCs are categorized into passive and active systems. Passive heave compensation (PHC) involves a vibration-isolating device placed between offshore cranes and the suspended load, functioning as a parallel spring-damper sub-system. This type of heave control cannot compensate for relative motion [50]. Conversely, active heave compensation systems (AHC) can reduce heave motion coupling to the payload by over 80% [51, 52]. Active heave control is utilized to enhance the operability of offshore installations under harsh sea conditions [53, 54] or during floating installations, serving a similar purpose to jack-up legs [25].

1.2. Thesis objective & Research scope

All aforementioned methods require either mechanical equipment in direct contact with the payload, or utilize indirect means of control (proposing limiting controllability) or involve active human intervention. These facts, amplified by the delicate nature of positioning OWT components, the small error tolerances and the harsh offshore environment, illuminate the necessity for a direct but non-contact position control technique for OWT in-

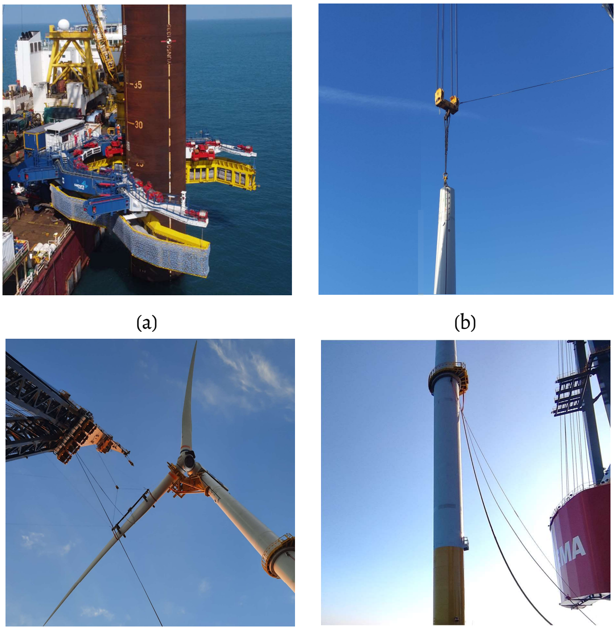

(a) (b)

(c) (d)

Figure 1.5: (a) Motion compensate gripper frame for monopile foundation installations during the Yunlin offshore wind farm project [55], (b) Active tugger line system attached on the hook block during the lift of an OWT tower, (c) Tugger lines attached on the blade during the RNA assembly, (d) Tugger lines (manually operated) attached on the skybox during the installation of an OWT tower [43].

stallations. Such a technique would both contribute to the safety of the crew (by reducing the risk associated with human interventions offshore) and positively influence the duration of the overall procedure, which is—as previously established—a major deciding factor for the efficiency and cost of the operation. Consequently, the main objective of this thesis is formulated as follows:

> **Thesis objective:** The development of the proof-of-concept of a contactless motion control technique for suspended loads during offshore wind turbine installation.

The thesis aims to establish the foundations for a novel alternative to the customary methods used by the industry. The installation is operated by a semi-submersible heavy lift vessel and concerns the installation of the heavy-weight wind turbine components, namely the tower or monopile foundation. The proof-of-concept is built upon numerical simulations of the interaction of the dynamical system and the contactless controller and is partially validated through scaled laboratory experiments.

The proposed control concept consists of two main components: a fine and a coarse control algorithm. The fine control encompasses the main motion mitigation and manipulation technique, which is based on electromagnetic interaction between a permanent magnet arrangement on the payload (the motion of which necessitates control) and an external electromagnetic actuator (or a group thereof) mounted on deck (Figure 1.6a). To optimize the performance of the actuator, a coarse controller is proposed that involves the use of a spatial actuator (i.e. a robotic arm or a drone) to maintain the desired distance from the payload throughout the operation.

The contribution of this study resides in its innovative nature. The proposed method employs a direct, contactless motion control and requires no equipment physically connected to the payload during the operation, hence evading the necessity for potential repair work (i.e. accidental paint coat removal or other light damage). The undertaking of any repairs or refurbishments *in situ* is highly undesirable for the operator, given its adverse implications in terms of both additional time and cost. Electromagnetic interaction facilitates both attraction and repulsion of the load, with the purpose of substantially enhancing the controllability of the system. Furthermore, the method is compatible with floating installation vessels and offers a mechanical advantage, rendering it efficient even underwater.

The envisioned system consists of the semi-submersible vessel, the crane-payload and the contactless motion control technique. The vessel is subjected to an array of environmental loads, namely wind, waves and currents. These loads function as a disturbance to its DP system, prompting corrections to its position for the purpose of maintaining the designated set point. The resultant response of the vessel serves as an external excitation for the crane-payload system, which constitutes the primary sub-system of interest for this thesis. In addition, contingent upon the installation stage (lifting, transporting, or lowering), aerodynamic and hydrodynamic forces are exerted directly on the load. To attenuate any undesired pendulation, the contactless control actuator is activated. Through the electromagnetic interaction of the two magnetic units (namely the actuator and the magnetic arrangement on the load, Figure 1.6a), the controller aims at maintaining a desired motion of the suspended load, always with regard to an efficient and secure assembly. A concise depiction of the data flow within the described system is presented in Figure 1.6b.

The dissertation investigates the efficacy of the contactless technique in controlling the in-plane translational motion (in xz- and yz-plane, see Figure 1.6a) and rotation (around z-axis, see Figure 1.6a) of a suspended load. The primary approach involves the development of numerical models for the simulation of the controlled system, with supplementary calibration and validation through scaled experimental tests. Full-scale measurements are also used as input for the simulations, which are available through the DOT6000-FOX (**F**loating installation **O**ffshore **X**xl wind turbines) project. DOT6000-FOX[*] facilitated the first-ever full-scale testing campaign for the complete assembly of an offshore wind turbine utilizing a floating HLV. Motions of the payload along its vertical axis (z-axis, see Figure 1.6a) are not studied, as they are considered to be effectively mitigated by the active heave compensation system of the crane. This was demonstrated during the exemplary

---

[*] a project subsidized by RVO (Rijksdienst voor Ondernemend Nederland) [56].

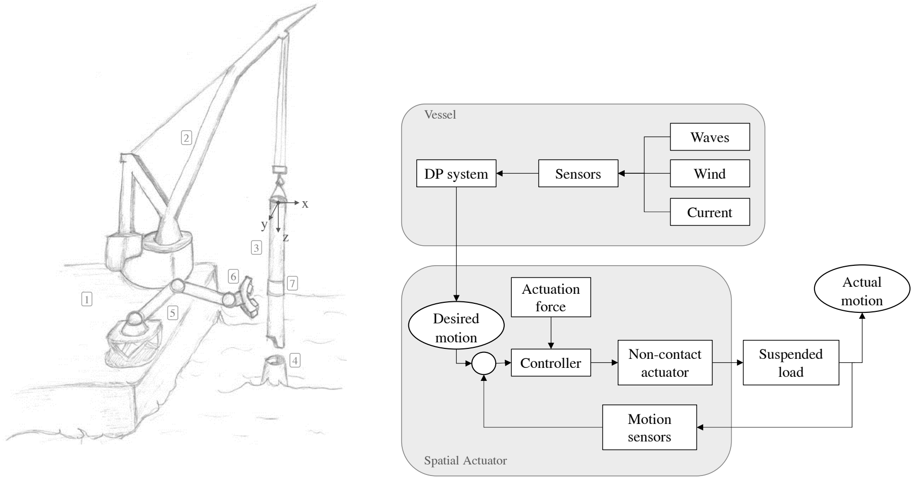

(a) (b)

Figure 1.6: (a) Annotated schematic diagram of an installation of an OWT tower operated by a semi-submersible vessel and the contactless motion control technique proposed in the thesis: 1. Floating vessel deck, 2. Heavy lift crane, 3. OWT tower, 4. Monopile head, 5. Spatial actuator (i.e. robotic arm), 6. Electromagnetic actuators and 7. Arrangement of permanent magnets attached to the tower (i.e. magnetic belt). (b) Block diagram of the vessel-crane-controller system.

offshore DOT6000-FOX campaign, where the crane of the floating HLV (HMC-*Sleipnir*, Figure 1.3b) was equipped with high-speed electronically controlled hoisting winches for active heave compensation [57].

1.3. Thesis outline

Due to the complexity of the full-scale system, and in order to effectively devise the new control method, this research employs a comprehensive step-wise methodology. This approach enhances the understanding of the underlying dynamics of both the controller and the dynamical system. Consequently, the envisioned full-scale dynamical system is represented by several incremental systems, each serving as a simplified, yet analogous, representation of the original system. Each incremental system is designed to demonstrate the potential of the contactless motion control method, with a focus on addressing a reduced number of degrees of freedom (DOF) at a time. A visual representation of the thesis structure is presented in Figure 1.7.

The proof-of-concept initiates with a nonlinear single-degree-of-freedom (SDOF) analogue system of a suspended point mass pendulum, representing a simplified floating crane-payload model. In *Chapter 2*, the theoretical background of the dynamics and control of the contactless control of a planar SDOF magnetic pendulum interacting with an electromagnetic actuator are presented. This chapter serves as the foundation for the control methodology and dynamics explored in the thesis.

In *Chapter 3*, the calibration and validation of the numerical model are elucidated, utilising measurements obtained through an experimental campaign. The experimental setup pertains to a scaled prototype planar magnetic pendulum with a moving support.

The controlled response of the planar magnetic pendulum is elaborated in *Chapter 4*. The pendulum is excited by the kinematically prescribed motion of its pivot and is controlled by an electromagnet. This chapter focuses on the assessment of the efficiency of position control for the pendulum, concurrently exploring various control modes pertinent to the envisaged application, namely desired motion control including the imposition of a desired stationary position over time.

In addition to translational vibrations, the rotational vibration mode becomes significant for suspended loads. This mode pertains to the rotation of the payload around its longitudinal axis (shaft). *Chapter 5* concentrates on the control of these vibrations. This mode of vibration is conceptualized as a SDOF magnetic ring free to rotate around its centre interacting with an external electromagnetic actuator. The designed controller leverages the system's dipole-to-dipole nonlinear dynamics to enforce a desired motion through various control modes, including the extraction of rotational energy by applying magnetically induced damping and active rotation control.

Following the independent analysis of the two most critical vibrational modes of a suspended load, *Chapter 6* explores the coupled dynamics involved in concurrently controlling translational and torsional vibrations. The lab-scale magnetic pendulum is enhanced by incorporating a rotational degree of freedom around its shaft (longitudinal axis). The study emphasizes the magnetic coupling effects and the controllability requirements introduced by this coupling, evaluating control efficiency across various control modes.

In *Chapter 7*, the system studied closely resembles an actual OWT tower installation, consisting of a planar triple pendulum with a suspended hook block and sling rope, supporting a cylinder as the tower payload. This configuration addresses the simultaneous control of multiple vibration modes (translational and rotational), integrating findings from previous chapters. The suspended load, modelled as a rigid body to exclude plastic deformation effects, is subjected to crane-tip-induced oscillations simulating wave-action disturbances. The chapter provides a dual evaluation: first, examining the arrangement of electromagnetic actuators and corresponding permanent magnets; second, assessing the efficiency and controllability achieved by the control system at full-scale. Additionally, realistic disturbance inputs from an offshore measurement campaign are incorporated into the model. This campaign identified the dominant environmental loads and the order of magnitude of the tower's motion during installation. Preliminary estimates of the required actuation forces are also presented, offering a comparative analysis with conventional motion control techniques.

Finally, the thesis concludes with *Chapter 8*, which gathers the main conclusions drawn from this thesis, accompanied by recommendations and indications for further future research.

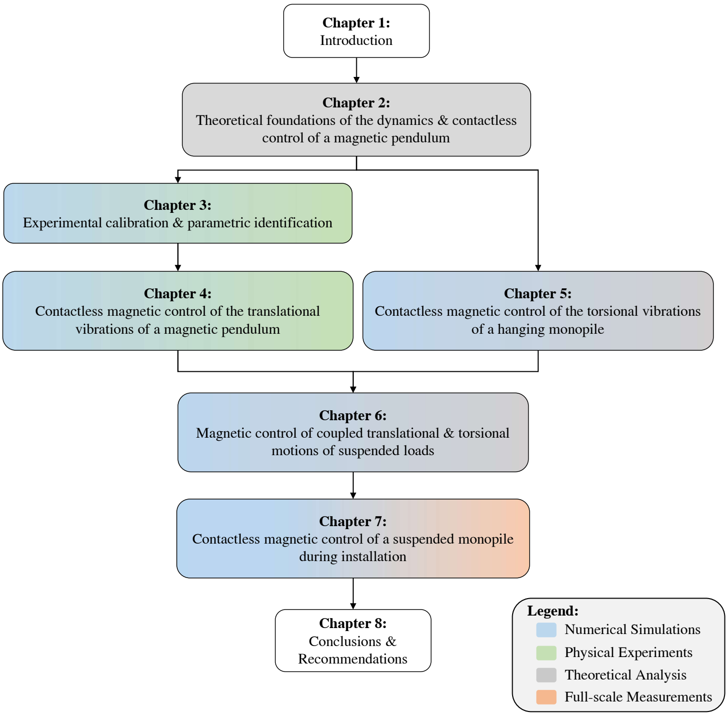

Figure 1.7: Thesis Outline

2

Theoretical foundations of the dynamics and contactless control of a magnetic pendulum

The problem of a suspended offshore wind turbine component on a moving crane vessel can be translated to an analogue of a pendulum with a moving pivot point. In order to develop and design the contactless control technique, a simplified, yet sufficiently accurate, dynamical system is employed. The dynamical system concerns a single-degree-of-freedom (SDOF) magnetic pendulum interacting with an electromagnetic actuator. This magneto-mechanical analogue serves as a proof-of-concept for the envisioned contactless technique, while the set-up, although simplified, incorporates the relevant physical processes that occur during the installation and the magnetic interaction on a smaller scale.

The present chapter establishes the theoretical framework for the dynamics and control methodologies employed in this thesis. First, a review of the current state-of-the-art in pendulum control is presented, identifying existing knowledge gaps and evaluating the technological advancements that have been tested so far. Subsequently, a detailed presentation of the set-up and the derivation of the equations of motion of the magneto-mechanical analogue are provided. Following this, the focus shifts to the development of the control algorithm for the nonlinear electromagnetic actuator, with a comprehensive discussion of its intricacies and design considerations.

2.1. State of the art in magnetic pendulum control

Complex phenomena such as strong nonlinearity and chaotic behaviour can be easily initiated by the magnetic interaction between an external magnetic source and the magnetic pendulum [58]. This interaction has been employed in various engineering mechanisms and devices, leading to systems known as magnetic or magnetically-excited pendula.

Literature abounds with research involving the interaction of magnetically-excited pendula and the nonlinear dynamics they introduce. First, they can function as structural vibration damping devices, e.g. passive [59, 60] and active [61] energy absorbers. Second, chaotic pendula or externally-excited pendula can contribute to energy harvesting through their oscillations [62, 63]. Depending on the manner in which the pendulum mass gains its magnetic properties, magnetic pendula are divided into two main categories: ferromagnetic pendula and pendula augmented with a magnet attached to their mass. Mann studied the dynamic behaviour of a bistable experiment comprised a ferromagnetic pendulum and two permanent magnets [64]. Work has been conducted for magnetic pendula with a permanent magnet mounted to the suspended mass and either a permanent magnet [65] or an electromagnet (solenoid or coil) below the pendulum's equilibrium point [66, 67]. In the latter configuration, a pulsating current signal (repulsing [68] or attractive) is introduced to excite the system. In the present research, the setup and orientation of the two magnets differ from previous studies: the electromagnetic actuator is in line with the mass of the pendulum (rather than below its equilibrium), and the magnetic interaction involves direct magnet-to-magnet interaction (both attraction and repulsion cycles). The proposed actuator utilizes alterations in the magnetic field properties of the actuator as a means-to-an-end for the motion control of the pendulum.

In terms of control, the studies on magnetically-controlled pendula are rather scarce. The topics of these studies range from a two-step controller (using switch on and off conditions) of an attracting magnetic field of a solenoid as external excitation of a mass-pendulum system model [69] to a control technique based on the width of the applied pulse and position sensing of a pendulum [70]. Ida [70] studied a magnetic pendulum of an embedded magnet on the mass and a pulsing coil that repelled the mass at the equilibrium position and attracted it, at the maximum amplitude of oscillation. Fradkov et al. [71] developed a pulse-modulated control law for the excitation and oscillation synchronization of a mechatronic system of two coupled double pendulums via the speed-gradient method. Kraftmakher [72] designed a magnetically-controlled compound pendulum with two permanent magnets mounted into each free tip and two adjacent electromagnets on both sides. The upper magnet received the excitation and the interaction of the magnets on the other end served as a damping restoring torque. For the application of motion compensation and control of a suspended load on a moving base such as a floating vessel, a limited or fixed position for the pendulum mass is not ideal. Thus, the opportunity for a time-varying motion manipulation is highlighted. Additionally, a magnetic controller capable of altering its magnetic properties (e.g., modifying the strength and polarity of the magnetic actuator) would enhance the system's controllability, facilitating both attractive and repulsive forces.

2.2. Spherical pendulum dynamics

Prior to studying the actuation force and developing the control technique, it is essential to derive the equations of motion (EOMs) that describe the free vibrations of the system. Given the complexity of the full-scale problem, which involves many interacting components, a simplified system is adopted to develop the proof-of-concept for the contactless technique. The suspended load on a floating crane is thus represented by a point mass spherical pendulum analogue as shown in Figure 2.1. This configuration is widely used in crane modelling as it yields a simple and compact mathematical model while capturing the essentials of the complex dynamics of the payload motion [73]. In this derivation, a reduced spherical pendulum model is employed, where all external base excitations (motions of the vessel) are translated to the resulting motion of the pendulum's suspension point (crane tip).

To describe the free oscillations of a spherical pendulum in polar coordinates, the Lagrangian formalism is applied. The system, depicted in Figure 2.1b, consists of a load with point mass M and a (inextensible) pendulum arm of length ℓ and total mass m. A spherical joint serves as the pivot point of the pendulum and can be kinematically excited by a prescribed motion $\vec{h}$ with components h_x, h_y, and h_z along the different axes. The unknown state variables of the system are denoted as ψ_x, ψ_y, and ϕ, representing the in-plane angle, the out-of-plane angle (between the equilibrium position of the pendulum system and its position at any given time interval Δt), and the torsional rigid body angle (rotation around the longitudinal axis, similar to the yaw angle in mechanics), respectively [73].

In this study, the pendulum's angular displacement is defined using two sway angles ([74, 75]), as opposed to the conventional representation in literature, which assigns one azimuth angle (around the z-axis) and one sway angle in the plane defined by the azimuth [76, 77]. This alternative angle assignment eliminates the undefined region of the azimuth angle when the sway angle approaches zero, making it more applicable to crane-payload models [73].

The positions of the two components of the system are expressed as

$$\vec{P}_G = \vec{P} + \vec{h} = \begin{bmatrix} \ell \sin(\psi_x) \\ \ell \cos(\psi_x) \sin(\psi_y) \\ \ell \cos(\psi_x) \cos(\psi_y) \end{bmatrix} + \begin{bmatrix} h_x \\ h_y \\ h_z \end{bmatrix}, \tag{2.1a}$$

$$\vec{P}_{r_G} = \vec{P}_r + \vec{h} = \begin{bmatrix} n \sin(\psi_x) \\ n \cos(\psi_x) \sin(\psi_y) \\ n \cos(\psi_x) \cos(\psi_y) \end{bmatrix} + \begin{bmatrix} h_x \\ h_y \\ h_z \end{bmatrix}, \tag{2.1b}$$

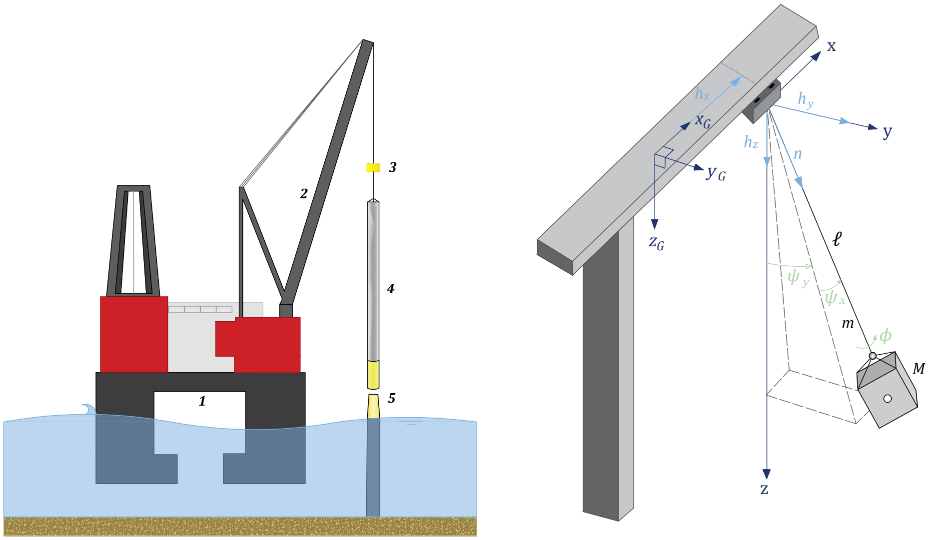

(a)

(b)

Figure 2.1: (a) Annotated diagram of the tower installation: 1. Floating vessel, 2. Heavy lift crane, 3. Lifting block, 4. Wind turbine tower, and 5. Monopile, (b) Schematic diagram of a spherical pendulum.

$$\vec{P}_f = \vec{P}_G + \begin{bmatrix} R\cos(\phi) \\ R\sin(\phi) \\ \ell + h_z \end{bmatrix}, \tag{2.1c}$$

where $\vec{P}$ and $\vec{P}_r$ represent the local position vectors of the centre of gravity (COG) for the point mass and the rod of the pendulum, respectively. $\vec{P}_G$ and $\vec{P}_{r_G}$ denote the global position vectors of the two components, while $\vec{P}_f$ contains the coordinates of the magnet attached on the mass. The scalar n denotes the position along the pendulum arm, measured from the pivot point to the location of the point mass.

The kinetic ($\mathcal{K}$) and potential ($\mathcal{U}$) energy of the dynamical system are given by

$$\mathcal{K} = \frac{1}{2}M\|\vec{P}_G\|^2 + \frac{1}{2}\frac{m}{\ell}\int_0^{\ell}\|\vec{P}_{r_G}\|^2\,\mathrm{d}n + \frac{1}{2}I_z\dot{\phi}^2 \tag{2.2a}$$

$$\mathcal{U} = Mg\left(\ell - \vec{k}\cdot\vec{P}_G\right) + \frac{m}{\ell}g\left(\int_0^{\ell}\left(\ell - \vec{k}\cdot\vec{P}_{r_G}\right)\mathrm{d}n\right) + \frac{1}{2}k_s\phi^2, \tag{2.2b}$$

where $\vec{k}$ represents the unit vector in the vertical direction (z-axis), while I_z denotes the mass moment of inertia of the point mass around the rope's axis, and k_s represent the torsional stiffness of the rope with respect to ϕ.

For the derivation of the equation of motion, the Lagrangian ($\mathcal{L}$) is formulated as

$$\frac{\mathrm{d}}{\mathrm{d}t}\left(\frac{\partial \mathcal{L}}{\partial \vec{q}}\right) - \frac{\partial \mathcal{L}}{\partial \vec{q}} + \frac{\partial \mathscr{R}}{\partial \vec{q}} = 0 \text{ with } \mathcal{L} = \mathcal{K} - \mathcal{U} \text{ and } \vec{q} = \left[\psi_x, \psi_y, \phi\right]^{\mathrm{T}}, \tag{2.3}$$

in which $\vec{q}$ describes the vector of the unknown states of the system and $\mathscr{R}$ is the Rayleigh dissipation function. The evaluation of Equation (7.3) yields the following nonlinear equations of motion:

$$\begin{aligned}
&\left(M + \frac{m}{3}\right)\ell^2\ddot{\psi}_x + \left(M + \frac{m}{2}\right)g\ell\cos(\psi_y)\sin(\psi_x) \\
&\quad = -\left(M + \frac{m}{3}\right)\frac{\ell^2}{2}\sin(2\psi_x)\dot{\psi}_y^2 - \left(M + \frac{m}{2}\right)\ell\cos(\psi_x)\ddot{h}_x \\
&\qquad + \left(M + \frac{m}{2}\right)\ell\sin(\psi_y)\sin(\psi_x)\ddot{h}_y + \left(M + \frac{m}{2}\right)\ell\cos(\psi_y)\sin(\psi_x)\ddot{h}_z,
\end{aligned} \tag{2.4a}$$

$$\begin{aligned}
&\left(M + \frac{m}{3}\right)\ell^2\cos^2(\psi_x)\ddot{\psi}_y + \left(M + \frac{m}{2}\right)g\ell\sin(\psi_y)\cos(\psi_x) \\
&\quad = +2\left(M + \frac{m}{3}\right)\ell^2\cos(\psi_x)\sin(\psi_x)\dot{\psi}_y\dot{\psi}_x - \left(M + \frac{m}{2}\right)\ell\cos(\psi_y)\cos(\psi_x)\ddot{h}_y \\
&\qquad + \left(M + \frac{m}{2}\right)\ell\sin(\psi_y)\cos(\psi_x)\ddot{h}_z.
\end{aligned} \tag{2.4b}$$

The third equation of motion of the system governs the angular position ϕ. It is chosen to be linear and reads:

$$I_z\ddot{\phi} + k_s\phi = 0. \tag{2.5}$$

It is noted that for this configuration of the system, the in-plane rotations and the torsional vibrations are not coupled through inertial or stiffness terms.

The equations of motion of the system can be simplified by geometrically linearizing around the stable equilibrium position of the pendulum. However, the linearized EOMs accurately represent the system's dynamics only when the pendulation amplitude remains within a few degrees. Beyond this range, the nonlinear characteristics of the suspended load become significant, and the nonlinear terms and dynamic complexities arising from mode coupling cannot be neglected [73]. Simulated data on the dynamic response of heavy cargo suspended by a floating crane (e.g., a fully assembled offshore wind turbine) indicate that the maximum translational displacements in 3D space are generally under 1 m, with only heave (vertical displacement) exceeding this limit [38]. Angular displacements are typically a few degrees for rotations around the x- and y-axes and less than 10° for yaw motion (rotation around the z-axis) of the suspended OWT [37, 38]. Consequently, the EOMs of the system can be linearized by omitting higher-order and coupling terms from Equation (2.4). Specifically, assuming the small-angle approximation ($\sin(\vec{\psi}) \simeq \vec{\psi}$ and $\cos(\vec{\psi}) \simeq 1$), the resulting set of linear equations becomes:

$$\left(M+\frac{m}{3}\right)\ell^2\ddot{\vec{\psi}}+\left(M+\frac{m}{2}\right)g\ell\vec{\psi}=-\left(M+\frac{m}{2}\right)\ell\ddot{\vec{h}},\ \text{with}\ \vec{\psi}=\left[\psi_x,\psi_y\right]^{\mathrm{T}}, \tag{2.6}$$

Geometrical linearization around the equilibrium results in the decoupling of the spherical pendulum's motion into two separate planes. In other words, the spherical position of the system is the superposition of the oscillations of the pendulum's planar projections in the two planes (xz- and yz-planes). Therefore, the in-plane oscillations of a simple pendulum driven by its pivot point in the xz-plane can be described by:

$$\left(M+\frac{m}{3}\right)\ell^2\ddot{\psi}+\left(M+\frac{m}{2}\right)g\ell\psi=-\left(M+\frac{m}{2}\right)\ell\ddot{h}_x+\left(M+\frac{m}{2}\right)\ell\psi\ddot{h}_z, \tag{2.7}$$

where h_x and h_z represent the horizontal and vertical pivot motion respectively, and ψ defines the angle of rotation of the pendulum ($\psi_x \equiv \psi_y = \psi$).

The nonlinear equations of motion of the same simple planar pendulum can be deduced from Equation (2.4), assuming $\psi_y = 0$ and $h_y = 0$, yielding:

$$\left(M+\frac{m}{3}\right)\ell^2\ddot{\psi}+\left(M+\frac{m}{2}\right)g\ell\sin(\psi)=-\left(M+\frac{m}{2}\right)\ell\cos(\psi)\ddot{h}. \tag{2.8}$$

In the present derivation, the rod is assumed to be inextensible for the simplicity of the analysis. Furthermore, the mass of the pendulum arm is not neglected, and its contribution is included in the governing equations. For the limiting case where the rod is considered to be massless (when $m = 0$), the in-plane equation of motion reduces to that of a conventional simple pendulum driven by its pivot [78]:

$$M\ell^2\ddot{\psi}+Mg\ell\sin(\psi)=-M\ell\cos(\psi)\ddot{h}. \tag{2.9}$$

As already discussed in the Chapter 1, the external excitation caused by the heave motions of the vessel is not studied, assuming $h_z \approx 0$, as the crane of the floating vessel considered in the present work is augmented by an active heave compensation controller to decouple the suspended load from the vessel heave motion due to wave excitation.

2.3. Planar magnetic pendulum dynamics

The dynamics of a magnetically-controlled planar pendulum is studied to initiate the development of the contactless technique proposed in this research. The system pertains to the planar point mass pendulum as illustrated in Figure 2.2, following the full derivation of its EOMs presented in the previous section. For the design of the contactless controller, two permanent magnets are employed, one attached to the point mass (represented as $\vec{m}_c$) and one at a certain distance away from the equilibrium position (denoted as $\vec{m}_t$). Both magnets are represented by magnetic dipoles; the simplest magnetic component. Combinations of dipoles can satisfactorily emulate the behaviour of any magnet (or geometry of magnets)

[79, 80]. The external dipole is capable of changing its polarity, which is mathematically represented by the orientation angle θ.

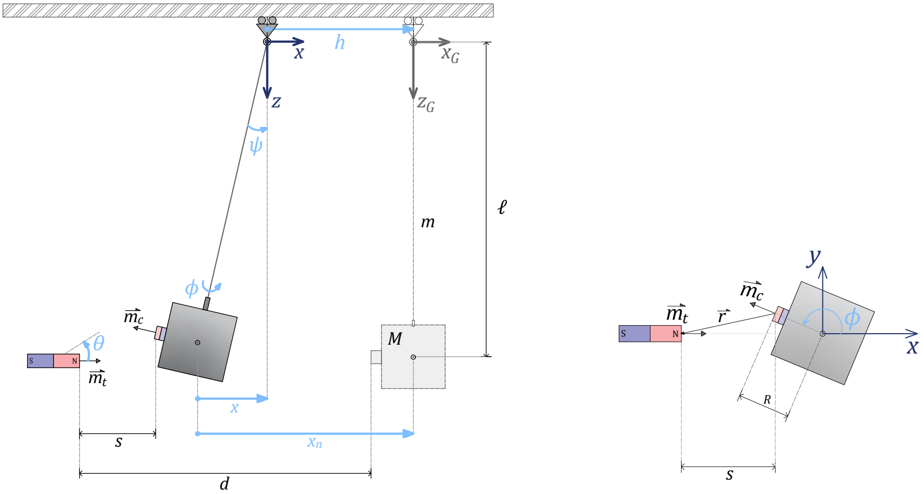

(a) *xz*-plane (b) *xy*-plane

Figure 2.2: Schematisation of a planar magnetically-controlled pendulum.

In addition to the prescribed motion at the pivot point, the mass can be subjected to excitation from other external sources. In offshore operations, the dynamic excitations can be the waves, wind, and ocean currents, which can introduce vibrations of the pendulum by acting either indirectly (through the motion of the crane tip) or directly to the payload. Accounting for these external excitations, the EOMs are now rewritten as

$$\left(M+\frac{m}{3}\right)\ell^2\ddot{\psi}+D_t(\dot{\psi})+\left(M+\frac{m}{2}\right)g\ell\psi=-\left(M+\frac{m}{2}\right)\ell\ddot{h}+T_t \tag{2.10a}$$

$$I_z\ddot{\phi}+D_f(\dot{\phi})+k_s\phi=T_f, \tag{2.10b}$$

with D_t and D_f representing generic dissipation torques active in the pivot joint and the torsional vibrations respectively. Dissipation torques are considered to be (a linear or non-linear) function of the angular velocity. The total external excitation torques are denoted as T_t and T_f and include the contributions of the environmental loads ($T_{f,e}$ and $T_{t,e}$) and magnetic interaction components ($T_{f,m}$ and $T_{t,m}$). The latter components can be computed by

$$T_m=\frac{\partial W_m}{\partial \vec{q}} \text{ with } \vec{q}=\left[\psi,\phi\right]^{\mathrm{T}}, \tag{2.11}$$

where W_m refers to the contribution of the magnetic interaction to the potential energy of the system and is equal to

$$W_m=-\vec{m}_c\cdot\vec{B}_t, \tag{2.12}$$

in which $\vec{B}_t$ is the magnetic field exerted by the external dipole (ED) at the location of the dipole mounted on the point mass (AD) [81] and is computed by

$$\vec{B}_t = -\frac{\mu_0}{4\pi}\vec{\nabla}\frac{\vec{m}_t \cdot \vec{r}}{r^3}. \tag{2.13}$$

The magnetic constant μ_0 is equal to $4\pi \times 10^{-7}$ NA^{-2}, while the vector $\vec{r}$ represents the separation distance between the two dipoles as shown in Figure 2.2b. It is noted that the circumflex ˆ indicates a unit vector and a plain character indicates the magnitude of a vector (e.g. $\vec{r} = r\,\hat{r}$). The magnetic moments of the dipoles are given by

$$\vec{m}_t = M_t \begin{bmatrix} \cos(\theta) \\ \sin(\theta) \end{bmatrix} \text{ and } \vec{m}_c = -M_c \begin{bmatrix} \cos(\phi) \\ \sin(\phi) \end{bmatrix}, \tag{2.14}$$

If multiple dipoles are attached to the point mass, or if there are multiple sources of external magnetic fields, the total magnetic field is the superposition of the individual contributions from the different external dipoles at the locations of the dipoles on the pendulum mass. To establish the basics of magnet-to-magnet interaction, the analysis will focus on the interaction between two dipoles.

The magnetic field generated by the interaction of the magnetic pendulum and the external dipole ($\vec{B}_t$) is illustrated in Figure 2.3. The field lines and their respective directions are represented by arrows, uniform in size, which correspond to normalized values of $\vec{B}_t$ in space. The contour background of the figure indicates the areas of higher magnetic field strength, with its peaks centred at the position of the dipoles. Additionally, white arrows depict the orientation of the magnetic dipoles, with the arrowhead indicating the location of the north pole. Figure 2.3a demonstrates the magnetic field generated when the two dipoles are aligned with negative polarities ($\theta = 180°$). Naturally, if the pendulum was free to oscillate, this configuration would cause the two magnets to attract each other, thus resulting in a negative displacement of the pendulum mass (motion towards the ED). A positive polarity of the ED ($\theta = 0°$), however, would exert repulsive forces on the AD, pushing the mass away from the equilibrium position, as shown in Figure 2.3b.

The additional contribution on the potential energy W_m (substituting Equation (2.13) into Equation (5.4)) upon geometrical linearization ($\sin(\psi) \approx \psi$, $\sin(\phi) \approx \phi$, $\cos(\psi) = \cos(\phi) \approx 1$) reads

$$W_m = \frac{\mu_0 M_c M_t \cos(\theta)}{2\pi(d + h + \ell\psi)^3}. \tag{2.15}$$

Evaluating Equation (2.11) yields an expression for the magnetic torques:

$$T_t = \frac{\alpha M_t \cos(\theta)\ell}{(d + h + \ell\psi)^4} = F_t\ell, \tag{2.16a}$$

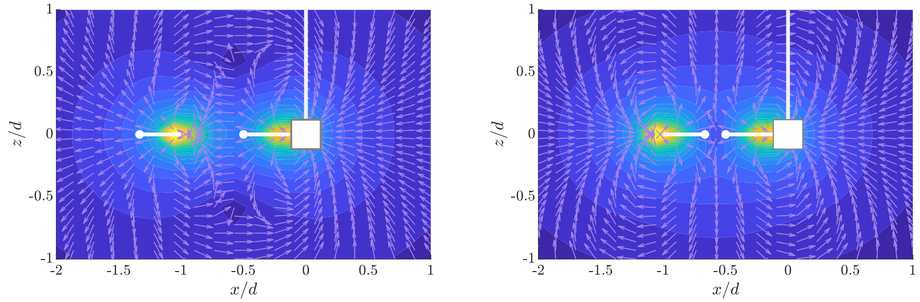

(a) Attraction

(b) Repulsion

Figure 2.3: Spatial distribution of the magnetic field generated by the two interacting dipoles for a static pendulum and different orientations of the ED.

$$T_f = 0, \tag{2.16b}$$

where F_t is the magnetic interaction force and the parameter α can be characterized as a magnetic constant and is expressed as

$$\alpha = \frac{3\mu_0 M_c}{2\pi}. \tag{2.17}$$

Thus, the excitation of the point mass is attributed solely to the torque T_t. Within the realm of small angular displacements, the two degrees of freedom of the system remain uncoupled, even in the presence of the magnetic interaction. For the remainder of this chapter, only the vibrations of the pendulum around its pivot are considered in the derivations.

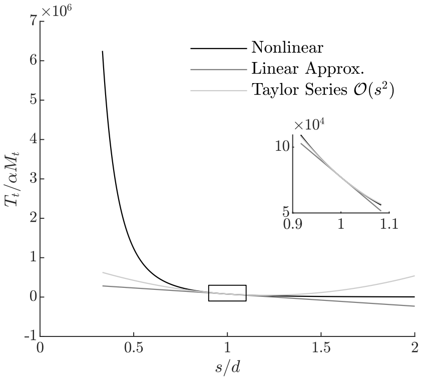

Figure 2.4: Comparison of the magnetic interaction force and a linear approximation formula.

Figure 2.4 illustrates the comparison of the dipole-to-dipole interaction nonlinear torque to the linear approximation formula derived through a Taylor series expansion for a separation distance $s \approx d$. A potential linearization of the electromagnetic torque around the static equilibrium of the pendulum is not fruitful, as such an approximation would significantly decrease the range of applicability. The horizontal displacement bandwidth where the linear model for the electromagnetic torque is still a reasonable approximation of the interaction is too narrow to be sufficient.

2.4. Control design of a magnetically-excited planar pendulum

To control the motion of the pendulum via electromagnetic interaction, a controller algorithm is designed. The PID (proportional-integral-derivative) controller is considered the most common closed-loop feedback controller used in control systems [82]. The basic equation of a PID controller in the time domain [83] is given by

$$c = K_p e + K_i \int e \, \mathrm{d}t + K_d \dot{e}, \tag{2.18}$$

where c and e are the control variables of the system and the error of the measured state from the desired reference, respectively.

The proportional gain (K_p) contributes to the stiffness of the system, providing an overall control action proportional to the error. Increasing the proportional gain decreases the transient response (settling time in control terminology) of the controlled system. However, a high value of K_p can lead to a steady-state error. The derivative gain (K_d) serves as an additional damping term, enhancing the closed-loop stability. It anticipates the future values of the error signal based on its current rate of change, thus improving the transient response. The integral gain (K_i) is crucial for eliminating error accumulation. The integral of the error is proportional to the area under the error curve, causing the control variable (c) to change continuously depending on the sign of the error signal. If c is constant, the error must be identically zero. This follows the principle that if the output of an integrator remains constant over a period, the input must be zero over that same period. Consequently, the integral term ensures that any persistent error is corrected, achieving zero steady-state error. The PID parameters of an exemplary controlled response are defined in Figure 2.5b, while the effects of the tuning of the different gains are presented in Table 2.1.

Table 2.1: Effects of Independent P, I, and D Tuning [84–86]

Tuning action	Rise time	Overshoot	Settling time	Steady-state error	Stability
Increasing K_p	decrease	increase	small increase	decrease	degrade
Increasing K_i	small decrease	increase	increase	large decrease	degrade
Increasing K_d	small decrease	decrease	decrease	minor change	improve

Given the interaction force, either the polarity (equivalent to $c = \operatorname{sgn}(\cos(\theta))$) or the strength of the electromagnetic device ($c = M_t$) can serve as the control variable of the system. The error term e captures the difference between the measured system output (x_n) and the desired positional reference (ξ) and is expressed as:

$$e = \xi - x_n = (\xi - h) - \ell\psi. \tag{2.19}$$

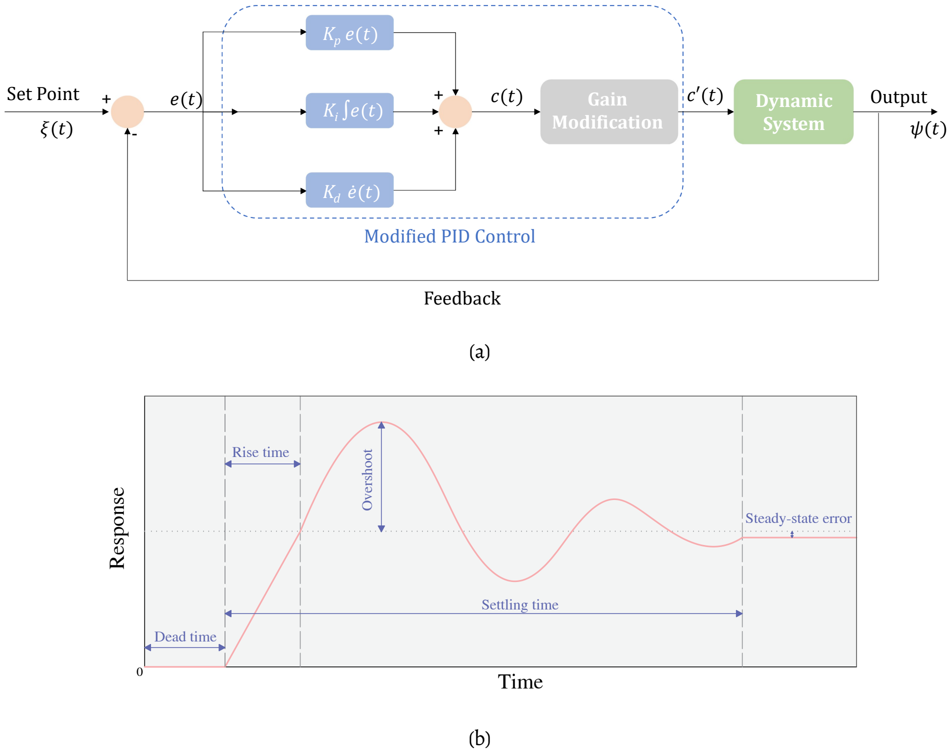

Figure 2.5: Response of a typical PID closed-loop system: (a). Block diagram, (b). Control parameter definition.

However, a conventional PID is designed for linear time-invariant systems (LTI) [87]. Overall, the dynamical system introduces nonlinearity through the distance-dependent nature of the force. In order to work with a consistent linear case without taking a toll on the accuracy and representation of the electromagnetic interaction, an additional path is included in the control algorithm (Figure 2.5a). This path, which bears a similarity to the nonlinear control techniques of feedback linearization [88] or gain scheduling [88], is employed for the sole purpose of replacing the current nonlinear control force with a linear control output for the control. A similar approach is adopted in [87], where a nonlinear PID controller is introduced to improve the performance of the standard linear counterpart by assigning the gains and integral time as prescribed nonlinear functions of the control error.

More specifically, in this case, the control output c is multiplied by a correction factor γ, creating a new control output c', which is used as the updated control variable and is given as

$$c' = K_p'(\psi)\, e + K_i'(\psi) \int e \, \mathrm{d}t + K_d'(\psi)\, \dot{e}, \tag{2.20}$$

in which $K_p'(\psi) = \gamma K_p$, $K_i'(\psi) = \gamma K_i$ and $K_d'(\psi) = \gamma K_d$, where $\gamma = s^4/\alpha$. With this modification, the PID gain parameters are converted from constant values to state-dependent coefficients. Consequently, the controlled equation of motion becomes:

$$\left(M + \frac{m}{3}\right) \ell^2 \ddot{\psi} + D(\dot{\psi}) + \left(M + \frac{m}{2}\right) g \ell \psi = -\left(M + \frac{m}{2}\right) \ell \ddot{h} + \frac{\alpha c'}{s^4} \ell. \tag{2.21}$$

Upon further simplification and evaluation of the modified control output c', the EOM is rewritten as

$$\left(M + \frac{m}{3}\right) \ddot{\psi} + \left[D(\dot{\psi}) + K_d\right] \dot{\psi} + \left[\left(M + \frac{m}{2}\right) \frac{g}{\ell} + K_p\right] \psi = -\left(M + \frac{m}{2}\right) \frac{\ddot{h}}{\ell} + T_t', \tag{2.22}$$

$$\text{with } T_t' = \frac{K_p}{\ell}(\xi - h) + \frac{K_i}{\ell} \int (\xi - \ell\psi - h) \, \mathrm{d}t + \frac{K_d}{\ell}(\dot{\xi} - \dot{h}). \tag{2.23}$$

In this form, it is evident that the state-dependent control gains successfully compensate for the nonlinear relationship between the actuation force and the separation distance between the two dipoles. Moreover, as expected, the PID controller not only introduces an external control torque to the system but also contributes to both the stiffness and damping, further manipulating the system to achieve the desired motion ξ.

2.5. Conclusions

The theoretical foundations supporting the methodologies employed in the thesis are presented in this chapter. First, a short overview of the state-of-the-art in magnetically excited and controlled pendula is reported, identifying the possible contributions to the literature relevant to the present research. In short, the contactless technique envisioned exploits magnet-to-magnet interactions, enabling both attractive and repulsive forces and thus enhancing the controllability of the motion of a suspended object.

Second, a crane-load analogue is studied. This analogue, though simplified, captures the essential dynamics of the real system and is widely used in crane modelling. By applying geometrical linearization to the derived equations of motion, the spherical pendulum oscillations of the mass decouple into two perpendicular planar pendulums with corresponding in-plane rotations around the equilibrium. Additionally, the in-plane and torsional rigid body degrees of freedom are not coupled.

This model is used to further analyse the dynamics of the magnetic interaction. To accurately emulate the interaction between two magnets (one on the pendulum load and one external), each magnet is modelled as a magnetic dipole. Dipoles are the simplest units to describe the geometry of the field of any magnet. For the control of the motion of the mass, a PID controller is developed modifying the strength and polarity of the external dipole as its control variable. Given the inherent nonlinearity of the actuation force, which cannot be circumvented without compromising the representation of the interaction, a modified version of the PID controller with nonlinear state-dependent gains is presented to improve performance. This modification aims to linearize the actuation force in the controlled equation of motion.

Using the knowledge demonstrated in this chapter, an experimental setup and a mathematical model are developed to further investigate and validate the proof-of-concept of the contactless motion control technique. In the following chapters, the results of these models are presented, demonstrating their performance for various control cases relevant to the intended application.

3

Experimental calibration & parameter identification

A prototype of the proof-of-concept system was built to validate the numerical model of the proposed control strategy through experimental tests on a laboratory scale. These measurements offer valuable insights into the accuracy of the simulations, the assumptions made, and the actual nonlinear effects and dynamics of the controlled system.

This chapter provides a detailed description of the experimental apparatus and instrumentation tailored to the design of the proof-of-concept system. The experimental tests focus on the identification and calibration of two forces that are fundamental for the successful control of the suspended load: the dissipative force in the suspension system and the electromagnetic interaction force exerted on the mass. These forces play a pivotal role in shaping the system's dynamics, and their precise calibration is paramount for ensuring the reliability of subsequent analyses.

To validate the calibration and assess the accuracy of the numerical model in representing the system, a control (reference) scenario is meticulously examined. This scenario involves inducing forced vibrations in the planar pendulum through the electromagnetic actuator. The system's response to externally prescribed electromagnetic excitation is recorded and then compared between the results obtained from the numerical model and the experimental measurements.

Part of this chapter has been published in:
P. Atzampou, P. C. Meijers, A. Tsouvalas, and A. V. Metrikine, "Contactless control of suspended loads for offshore installations: Proof of concept using magnetic interaction," *Journal of Sound and Vibration*, vol. 575, p. 118 246, 2024

3.1. Experimental apparatus & equipment

In accordance with the base model presented in the previous chapter for the initiation of the proof-of-concept of the technique, a lab-scale experimental campaign was designed. More specifically, the set-up, as illustrated in Figure 3.1a, consists of an immobile crane-shaped frame (representing the offshore crane), an inflexible aluminium rod of mass (m) that serves as the arm of the pendulum of length ℓ (equivalent to the crane cable and hook) and an aluminium solid cube for the pendulum mass M (analogue to the OWT suspended payload). The hanging load is modelled as a point mass, restrained to oscillate in one plane; thus, the apparatus resembles the problem of a single-degree-of-freedom (SDOF) pendulum. The wave-induced vibrations of the floating vessel-crane system are described by an external excitation through the motion of the pivot point of the pendulum h.

The same set-up is considered in both experimental and numerical simulations (Figure 3.1). The simulated configuration is presented schematically in Figure 3.1b and shows the global fixed axes $\left(x_G, y_G\right)$ and the moving with the pivot axes $\left(x, y\right)$ of the system as well as the positive assumed directions for the angular (ψ) and linear (x, x_n) displacements. Note that $x = \ell \sin(\psi)$. Due to the moving suspension point, the motion of the mass of the pendulum is characterized by two horizontal displacements; one from the equilibrium position given by x (the unknown state of the system) and one derived from the global reference system $x_n = x + h$. The initial distance d and the time-variant separation distance $s = d - x_n$ between the EM and PM are defined in Figure 3.1b. Table 3.1 summarizes the important parameters of the set-up.

The actuation of the system comprises a holding electromagnet (*Eclipse Magnetics* EM65-24V-DC) at a constant initial distance from the target suspended load. In order to achieve both attraction and repulsion conditions for the oscillations, a neodymium permanent magnet (N52 Ø15x3 mm) (PM) is attached and positioned at the centre of the side of the cube closest to the electromagnet (EM) as presented in detail in Figure 3.1a. The dipole moment of the PM in this arrangement is aligned with the EM, generating an attractive force on the PM when a positive voltage is applied to the EM.

Regarding the components of the experimental apparatus, a USB development board (Teensy 3.6) is utilised as a microcontroller for the control algorithm, while the data are logged using data acquisition software developed in-house by the technicians of Stevin-lab II (TUDelft). Moreover, the software enables the real-time modification of the control parameters, whereas the time series of the measured output and input signal of the electromagnet as well as the control variable are recorded with a sampling rate of 20 Hz. A pivot point linear (translation) actuator is designed in-house by DEMO (Dienst Elektronische en Mechanische Ontwikkeling) and it is used to apply prescribed horizontal excitation to the pendulum's hinge.

For the regulation of the voltage input of the electromagnet, an H-bridge electronic circuit is employed, whereas the power supply box has indicators for the voltage and intensity of the electricity generated. Lastly, for the purpose of tracking and logging the pendula-

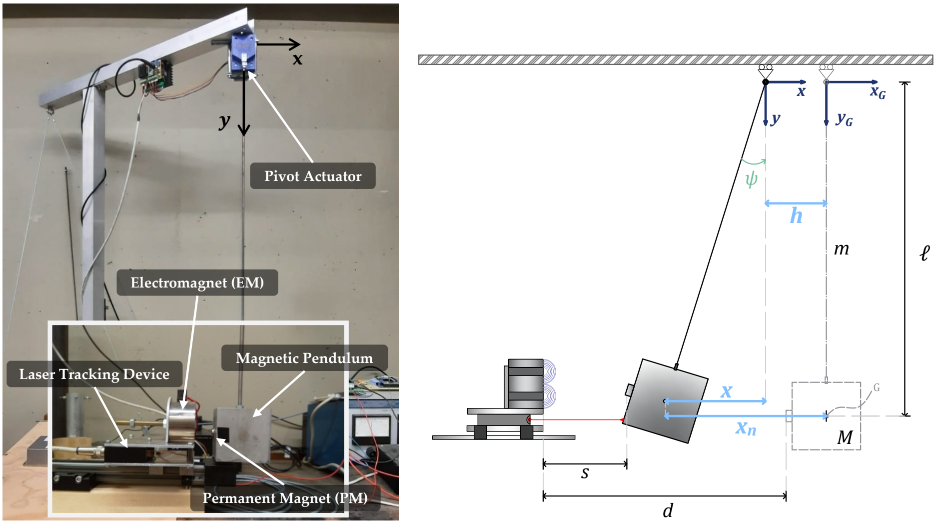

(a)

(b)

Figure 3.1: (a) Annotated photograph of the physical model. (b) Schematisation of the numerically simulated pendulum with a moving pivot point.

tion of the point mass, a laser distance measuring device is employed (*Altheris* FDRD603-100) with the sampling rate of 20 Hz and measurement accuracy of 5 μm. The pointer of the laser is aimed at the centre of the hanging mass, and the displacement from its equilibrium position is measured with the positive horizontal axis facing the EM as shown in Figure 3.1b as positive x-axis orientation.

The development of the magnetic field exerted by the electromagnet is measured through a Hall-effect magnetic field sensor (*Honeywell* SS491B). Figure 3.2 presents the schematic placement of the sensor (8 mm from the edge). The sensor measures one of the components of the magnetic field ($\vec{B}$), while the orientation of the sensor is calibrated such that $\vec{B}_h$ has the same positive direction as the $\vec{B}$ field generated by the EM by a positive voltage.

Table 3.1: Set-up dimensions and parameters.

ℓ [m]	M [kg]	m [kg]	Cube Size [mm]	PM Size [mm]	EM Size [mm]
1.04	0.9382	0.1868	70 x 70 x 70	Diameter = 15 Thickness = 3	Diameter = 65 Thickness = 35

In order to simplify the simulation of the system the following assumptions are made: 1) The arm of the pendulum is an inextensible rod restraining the mass from oscillating in-plane; 2) the displacement of the mass is small compared to the length of the pendulum, resulting in the small angle approximation ($\sin(\psi) \approx \psi$). Therefore, the unknown degree

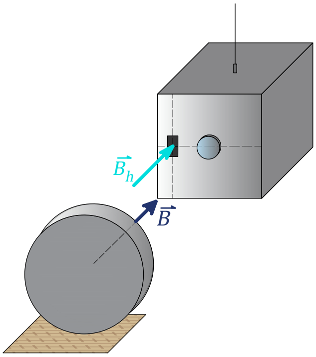

Figure 3.2: Hall sensor placement and orientation.

of freedom of the system corresponds to the translation of the mass in the horizontal axis, i.e. $x = \ell\psi$. The EOM of the planar magnetic pendulum, as derived in the previous chapter (Equation (2.10a)), is reformulated to its linear form as follows:

$$\left(M + \frac{m}{3}\right)\ddot{x} + \left(M + \frac{m}{2}\right)\frac{g}{\ell}x = -\left(M + \frac{m}{2}\right)\ddot{h} + \Sigma F, \tag{3.1}$$

where the horizontal displacement of the pendulum mass x is now the unknown degree of freedom, and ΣF corresponds to the summation of the external non-conservative forces acting on the pendulum. The undamped natural frequency (ω_n) of the dynamical system amounts to

$$\omega_n = \sqrt{\frac{M + \frac{m}{2}}{M + \frac{m}{3}}\frac{g}{\ell}} \approx 3.12\,\mathrm{rad/s}, \text{ and } f_n = \frac{\omega_n}{2\pi} \approx 0.496\,\mathrm{Hz} \tag{3.2}$$

where the numerical values in Table 3.1 are considered and the gravitational acceleration is equal to $g = 9.81\,\mathrm{m/s^2}$.

3.2. Parametric calibration of the nonlinear forcing

The external forces (ΣF) present in the dynamical system under consideration are a result of the action of the damping force (D) at the pivot point hinge and the electromagnetic interaction force between the two magnets (F). The calibration of the forces against experimental data is discussed in this section. It is noted that the torque which would be generated due to the aerodynamic forces is not considered an additional external disturbance for this initial investigation due to the specifics of the physical experimental set-up. These forces are not expected to have a significant influence on the control outcome as the pivot point motion is the dominant external excitation of the system.

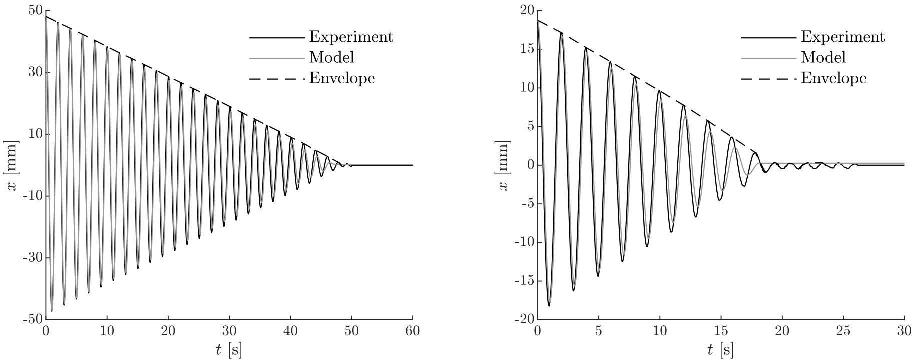

(a) $x(0) = 50$ mm (b) $x(0) = 20$ mm

Figure 3.3: Damping calibration of numerical simulations against experimental data for different initial distances $x(0)$.

3.2.1. Dissipative force

The metal hinge-type suspension pivot point of the pendulum introduces a source of energy dissipation for the system. In the numerical simulations, this dissipation is accounted for as an active external force acting on the suspended mass. This damping force is described by the Coulomb's friction formula and has the following form [90],

$$D = \frac{T_{fr}}{\ell} = -\mu \operatorname{sgn}(\dot{x}), \tag{3.3}$$

where T_{fr} is the frictional moment at the hinge and μ corresponds to the kinetic friction.

Coulomb friction is a nonlinear dissipative force and its action depends on various factors [91]. These factors pertain to the state (lubricated or dry) of the system and the relative time and temperature of the measurement, as well as the frequency and amplitude of the oscillation. In addition, kinetic friction introduces memory effects, namely, friction may depend on the history of the movement itself. The simulation of friction with high accuracy is a tedious stand-alone task and involves experiments with little reproducibility [91]. Additionally, such a damping force results from the specific experimental mechanical components (i.e. the hinge-type connection), and it is not an important feature of the real applications offshore. Hence, the dissipative force given by Equation (3.3) will be used in this work, as it is the simplest model that can sufficiently emulate the observed behaviour of the system.

Free vibrations can be used as exemplary cases, where important system parameters are identified quantitatively. The damping force in the numerical simulations is calibrated against experimental data. Figure 3.3 demonstrates a typical damped vibration measured in the lab for two cases of initial positions. The time trace of the motion displays an evident linear decay of the damped oscillation. Such a linear envelope indicates the presence of Coulomb's friction in the system [90].

The calibration of the damping coefficients is performed by releasing the pendulum mass from different initial positions ($x(0) \in [10, 50]$ mm) and recording the response. Then, the free vibration time series is compared to the corresponding signal provided by the numerical simulation, while the coefficients are tuned using a grey box non-linear system identification algorithm in MATLAB, and the empirical trial and error method. Three iterations of free vibrations for each initial position are performed, and the mean values are deduced to obtain better representative constants. Further validation is provided by the formula derived by Torzo and Peranzoni [90] for the case of a simple pendulum under sliding friction given by

$$\mu = \Delta\psi \frac{M\ell g}{2}, \tag{3.4}$$

where $\Delta\psi$ represents the slope of the linear envelope of the decay in units rad/s, M and ℓ the mass and the length of the pendulum respectively and g the gravitational acceleration. The value of $\Delta\psi$ is extracted from the coefficient of the linear approximation of the linear decay envelope. The calibration of the friction yields the constant value $\mu = 0.005$ kg m/s^2. The overall convergence ratio between the model prediction and the actual measurement is derived as $fit(\%) = (1-\kappa)$, where κ represents the normalized root mean square error (NRMSE) and amounts up to 80 % and 50 % for $x(0) = 50$ mm and 20 mm, respectively. This difference in efficiency is evident in Figure 3.3b where the simulations predict a slightly more damped response in terms of amplitude and a misfit in phase as the motion approaches zero amplitude. Moreover, the small amplitude oscillations around the equilibrium point observed in the experimental data are not captured by the model. A different friction model may provide a better fit for these small amplitudes. Nonetheless, simulations using the simple Coulomb friction model give satisfactory results compared to the measurements (Figure 3.3a). It is expected that, for the controlled vibrations, the exact representation of the damping is not critical in obtaining the desired result due to the compensation of the PID controller provided that oscillations are not of extremely low amplitude.

3.2.2. Electromagnetic force

The external excitation acting upon the pendulum results from the interaction between two magnets; one magnet of fixed polarity and strength (PM) and one electromagnet (EM). A series of experimental data was collected to derive a function to represent this interaction. More specifically, the electromagnet was set at different initial distances from the pendulum mass while both cycles of attraction and repulsion were investigated. In this section, the derivation and validation of the empirical experimentally-derived formula is shown.

Assuming that the PM can be approximated by a magnetic dipole $\vec{m}$, the force $\vec{F}$ on the PM (resulting from the magnetic interaction with the EM) is given by the gradient of the magnetic energy [92]:

$$\vec{F} = \nabla \left(\vec{m} \cdot \vec{B}\right), \tag{3.5}$$

in which ∇ represents the gradient operator, $\vec{m}$ is the dipole moment of the PM, and $\vec{B}$ is the magnetic field of the EM at the location of the PM. Assuming that the displacement of the pendulum is small compared to its length, the motion is restricted to the x-axis. Furthermore, the dipole moment $\vec{m}$ is assumed to be aligned with the x-axis. Hence, only the force component along this axis is relevant for the dynamics of the system. Using these assumptions, the force F_x is given by

$$F_x = \frac{\mathrm{d}}{\mathrm{d}x}\left(m_x B_x\right), \tag{3.6}$$

in which m_x is a time and space invariant constant representing the unknown strength of the PM. Given the relatively complex geometry of the EM, creating a model for the magnetic field B_x is not a trivial task. Therefore, the spatial variation of the field is determined from measured data. Figure 3.4 presents the magnetic field measured by the Hall sensor for different separation distances s, where $s = d - x$. A fit to the data for three distinct values of supply voltage V (Figure 3.4) shows that the field can be modelled as follows:

$$B_x = \frac{\alpha' V}{s^2}, \tag{3.7}$$

in which $V = RI$ denotes the static voltage which is directly proportional to the current I in the coil of the magnet. Note that, the electrical resistance R of the coil can be merged into the fitting parameter α', thus substituting the magnetic field into the force expression yields

$$F_x = \frac{\mathrm{d}}{\mathrm{d}x}\left(m_x \frac{\alpha' I}{s^2}\right) = -2m_x \frac{\alpha' I}{s^3} = \frac{\alpha J}{s^3} = \frac{\alpha J}{(d-x)^3}, \tag{3.8}$$

where J is the (instantaneous) voltage output, and α is a model constant accounting for the strength of the PM, the strength and geometry of the EM. The tolerances that accompany Equation (3.8) pertain to the minimum and maximum initial relative distance, where the formula is efficiently representative of the nonlinear phenomenon. This distance range translates to $d \in [25, 75]$ mm. Figure 3.4 shows the comparison between the experimental data set and the mathematical approximation formula.

As a result of the self-inductance L of the magnet, the current in the EM will not be proportional to the supplied voltage V. To account for this effect, the current in the EM is modelled as an elementary RL circuit [93]:

$$\dot{J} = \frac{1}{\tau}(V - J), \tag{3.9}$$

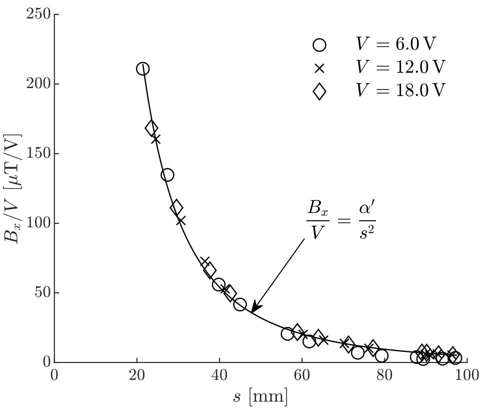

Figure 3.4: Determination of the dependency of the magnetic field generated by the EM with distance and applied voltage.

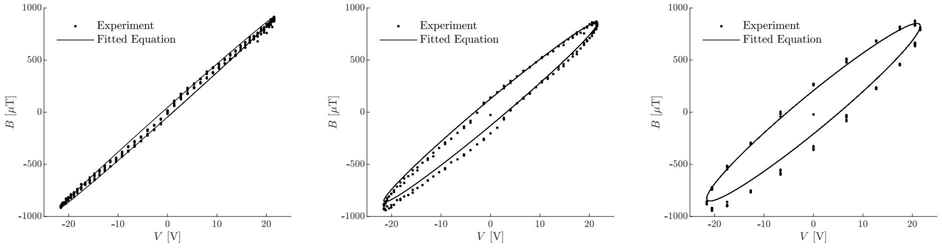

(a) 0.2 Hz

(b) 0.6 Hz

(c) 1.0 Hz

Figure 3.5: Determination of the time constant τ of the RL circuit.

where the derivative of the voltage output with respect to time is given by $\dot{J}$ and $\tau = L/R$. Since the numerical value for resistance R of the circuit can be condensed into the model coefficient for the magnetic field, the response of the circuit is fully determined by the time constant τ. The numerical value of the latter is easily extracted from measurement data, in which the magnetic field is determined for various harmonic voltage signals (Figure 3.5). By fitting the solution of the RL circuit model, it follows that $\tau = 0.040$ s.

Now the general equation for the magnetic interaction force is known, the coefficient α is to be determined. For this, the equilibrium position u_0 of the pendulum is measured for different constant values of the supply voltage. For static conditions, all time derivatives vanish from Equation (3.1) and the following relation applies:

$$\left(M + \frac{m}{2}\right)\frac{g}{\ell}x_0 = \frac{\alpha J}{\left(d - x_0\right)^3}, \tag{3.10}$$

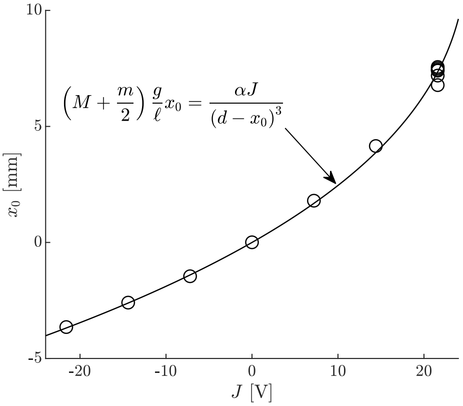

Figure 3.6: Measurements of the static equilibrium position of the pendulum with $d = 50$ mm for different supply voltages, and a fit to data to determine the magnetic interaction coefficient.

For an initial separation distance of $d = 50$ mm, Figure 3.6 presents the measured values for the equilibrium position. By fitting Equation (3.10) to this data, it is found that $\alpha = -2.5810 \times 10^{-7}$ Nm^3/V.

Note that the empirical formula Equation (3.8) differs slightly from the magnetic interaction force derived in Equation (2.16a). This discrepancy arises from the geometry of the external actuator. The electromagnet used in the experimental measurements generates magnetic field lines with a different arrangement and orientation compared to those of a single dipole, altering the nonlinear distance relationship.

3.3. Forced vibrations of a magnetically-excited planar pendulum

The predictive capabilities of the numerical simulation and the nonlinearity of the dynamical system can be further validated by studying the forced vibrations of the system. The motion of the pendulum with a fixed pivot point can be described by

$$\ddot{x}+\frac{K_t}{M_t}x=\frac{\mu}{M_t}\,\mathrm{sgn}\,(\dot{x})+\frac{\alpha}{M_t}\frac{J}{(d-x)^3}, \tag{3.11}$$

where $M_t = \left(M+\frac{m}{3}\right)$ is the effective inertia and $K_t = \left(M+\frac{m}{2}\right)\frac{g}{\ell}$ corresponds to the effective stiffness of the system. For simplicity, the self-inductance of the EM is neglected, resulting in $J \equiv V$. In order to modify the magnetic field exerted by the actuator, the voltage J serves as the forcing parameter.

The behaviour of the magnetic pendulum is now subjected to an alternating electromagnetic force. The voltage of the electromagnet is varied harmonically, taking the following form:

$$J = A\sin(\omega t), \tag{3.12}$$

in which A and ω represent the voltage amplitude and frequency, respectively. The initial separation distance between the two magnets is kept constant and equal to $d = 50\,\mathrm{mm}$. Additionally, a comparison between the experimental and simulation data is performed for various excitation cases to evaluate the accuracy of the numerical simulation of the system.

Figure 3.7 illustrates the dynamic response of the system when excited by an alternating electromagnetic force both in terms of amplitude and phase. More specifically, the root mean square (RMS) amplitude of the harmonic motion is extracted from the experimental data in order to construct the response spectrum of the pendulum in steady-state and is given by

$$x_{RMS} = \sqrt{2}\sqrt{\overline{(x-\overline{x})^2}}, \tag{3.13}$$

where x is the horizontal displacement and $\overline{x}$ the mean value of the displacement time series, which accounts for the equilibrium position of the oscillation. The overbar ($^{-}$) represents the mean value of the enclosed function and it is calculated by the following formula

$$\overline{f(t)} = \frac{1}{N}\sum_{n=1}^{N} f(t), \tag{3.14}$$

where N refers to the total number of data points and $f(t)$ to an arbitrary function.

To extract the phase of the simulated dynamic response signal φ, the Fast Fourier Transform (FFT) is employed. First, the signal is sampled at a consistent rate to obtain a discrete time series. This time-domain signal is then transformed into the frequency domain using the FFT algorithm, which decomposes it into its constituent sinusoidal components, each characterized by a specific frequency, amplitude, and phase. The output of the FFT algorithm consists of complex numbers, with the magnitude representing the amplitude of each frequency component and the argument (or angle) of the complex number corresponding to the phase.

In Figure 3.7, the markers refer to experimental data while the continuous lines pertain to the simulated response. The different shapes and line types indicate the amplitude of the excitation signal. The experimental and numerical data validate the presence of one natural frequency for the single degree of freedom of the system. The measurement points around resonance belong to cases, where the motion of the pendulum becomes unstable, causing the permanent magnet to stick to the core of the electromagnet. Therefore, these points represent a steady-state in which the separation distance between the two magnets is zero, namely the displacement is constant and equal to $x = d = 50\,\mathrm{mm}$, equal to the initial distance between the magnets. The phase angle of these points is omitted, as it cannot be computed and would not have significant physical meaning.

The comparison of the numerical and experimental data in Figure 3.7a shows that the best correspondence between the data occurs for the larger excitation amplitudes and excitation frequencies above the resonance frequency. For the small excitation amplitudes, the

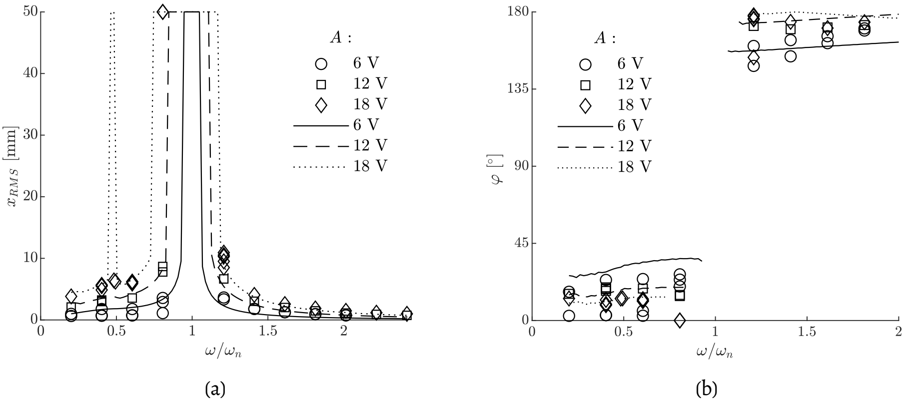

(a) (b)

Figure 3.7: Dynamic response of the experimental and numerically-simulated system: (a) Frequency response function: RMS amplitude of oscillations and (b) Phase of the response signal against frequency ratio ω/ω_n. The discrete markers represent the experimental data, while the continuous lines refer to the numerical simulations. The results are assigned different line types or marker shapes for each excitation amplitude.

prediction of the model is adequate but shows discrepancies between different measurements. These deviations can be attributed to the highly uncertain action of the friction force and the nonlinear damping it introduces. Besides these friction effects, the relatively weak magnetic field of the EM (when a small voltage is applied) may provide insufficient energy to overcome the magnetization of the EM's core, causing a delay in the alternation of the polarity of the magnetic field. As a result, the larger the amplitude of the applied voltage, the less significant the effect of these external nonlinear phenomena on the motion of the pendulum mass becomes.

In Figure 3.7b, the phase for the different excitation frequencies follows the anticipated shape of a damped response of a linear dynamical system. The distinct difference π is observed, with the system vibrating in anti-phase to the external excitation force for frequencies above its natural frequency ω_n.

Additionally, the modelled system appears to have a second resonance peak at half the natural frequency for the highest value of voltage amplitude as shown in Figure 3.7a. This behaviour is to be expected in the response of a nonlinear system [94]. However, this peak is not explicitly present in the respective experiments, where only a slight increase of the amplitude is observed. The reason is that the experimental set-up has a small degree of freedom for out-of-plane motion. Therefore, for the frequency $\omega_n/2$, the amplitude of the pendulum motion increases due to instability but starts to transfer energy to out-of-plane oscillations, converting the pendulum from simple to spherical. For the numerical model, however, the pendulum is restricted to oscillate as a SDOF system and thus allows the instability to grow in-plane. Moreover, the damping representation may also contribute to the secondary resonance, since it is less accurate for frequencies below ω_n. The time series of the displacement is presented in Figure 3.8a.

As established earlier, friction in the suspension is highly sensitive to factors such as lubrication, oscillation frequency, and amplitude. Therefore, some level of discrepancy is to be expected/anticipated between experimental measurements taken on different dates and lubrication stages as well as when the simulated response is compared to the real measurements. Further evidence of the friction-related discrepancies of the modelled response is presented in Figure 3.8b. The absence of freshly applied lubricant at the hinge pivot point of the pendulum introduces greater dissipative forces. Consequently, the system becomes unstable and sticks to the electromagnet after more cycles of oscillation (Experiment - L0).

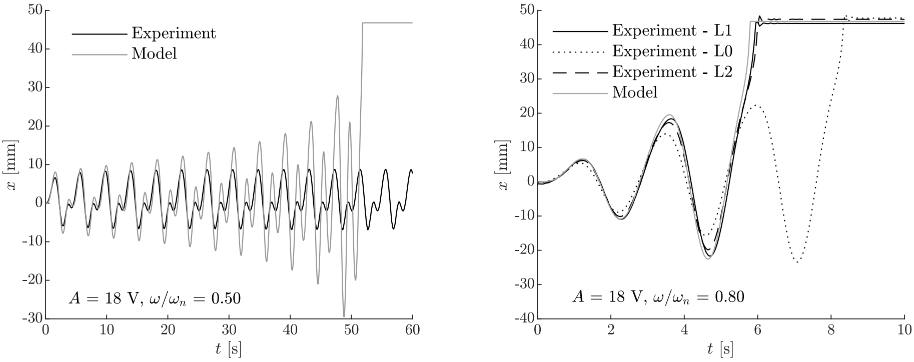

(a)

(b)

Figure 3.8: (a) Displacement time series for second resonance peak (ω/ω_n = 0.50 and A = 18 V), (b) Effect of the relative time of the experiment to the time of lubrication for a critical excitation case (ω/ω_n = 0.80 and A = 18 V) exhibiting instability. Experiment - L1 and Experiment - L2 represent two physical measurements taken under freshly lubricated conditions, whereas Experiment - L0 reflects the response of the system after a period of time has elapsed since Experiment - L1.

The excitation cases presented in Figure 3.8b and 3.9 involve three exemplary excitation frequencies, two below and one above resonance, with the forcing amplitude close to the saturation limits of the electromagnet, namely [−24 V, 24 V]. The experimental and simulated time series exhibit the same behaviour for the pendulation of the mass under electromagnetic interaction. Specifically, for the frequency ω/ω_n = 0.80, both the experimental and modelled data predict that the mass becomes unstable, causing the permanent magnet to be attracted to the core of the electromagnet almost instantly. In the case of ω/ω_n = 0.40, the model predictions correspond well with the respective measurement, including the prediction of the contribution of higher harmonic components to the response. For the frequency above resonance ($\omega > \omega_n$), the phenomenon of beating is observed, indicating the superposition of two harmonics of slightly different frequencies in the response: the excitation frequency (ω/ω_n = 1.20) and the natural frequency (ω/ω_n = 1) of the system.

Furthermore, the simulation results exhibit greater discrepancies in cases of lower forcing amplitude. Figure 3.10 presents two excitation frequencies, one above and one below ω_n, for amplitudes of A = 6 V and A = 12 V, respectively. The response of the system is

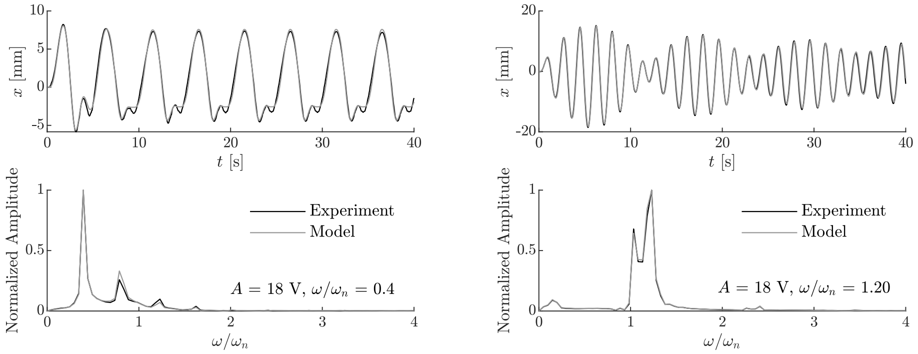

(a) (b)

Figure 3.9: Displacement time series for excitation cases of the same amplitude (A = 18 V) and different frequency ratios: (a) $\omega/\omega_n = 0.40$, (b) $\omega/\omega_n = 1.20$.

slightly underestimated in terms of amplitude for the lower frequencies and overestimated for higher frequencies. This behaviour can be attributed to nonlinearity introduced by the dissipation mechanism, leading to an underdamped response below resonance ($\omega/\omega_n < 1$) and an overdamped response above resonance ($\omega/\omega_n > 1$). Moreover, the displacement time series shown in Figure 3.10a is a superposition of multiple harmonic components, with the dominant frequency of the response equal to the excitation frequency and the rest being its multiples. The simulated response captures only the first two harmonic frequency components.

Figure 3.11 illustrates the response of the (numerically simulated) dynamical system across a range of excitation frequencies and amplitudes. The colour bar indicates the ratio of the maximum displacement of the mass, normalised by the initial distance between the magnets. For displacement ratios $x_{max}/d > 0.5$, the system exhibits unstable behaviour, with $x_{max}/d = 1$ corresponding to the yielding attraction of the magnets. It is evident that as the initial separation d decreases, the range of stable behaviour narrows both in terms of A and ω/ω_n. As anticipated, Figure 3.11a reflects the frequency response function obtained in Figure 3.7a for the three different values of A, highlighting the resonance frequencies. With decreasing distance, the nonlinear properties of the interaction become more pronounced, leading to the emergence of multiple resonant frequencies ω, which appear as harmonics of the natural frequency of the system ω_n.

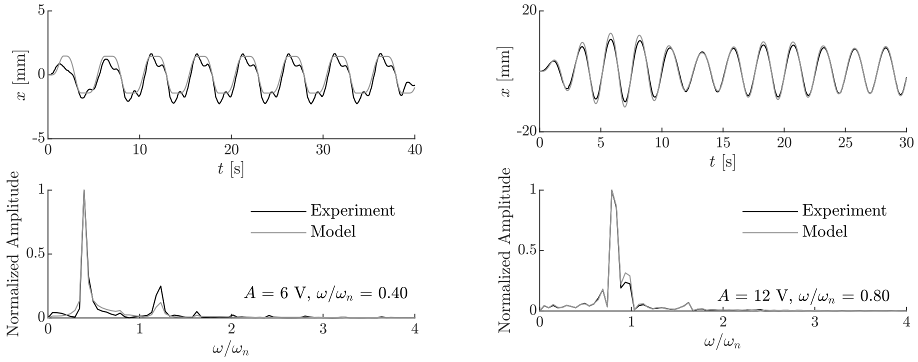

(a) $A = 6\,\mathrm{V}$ & $\omega/\omega_n = 0.40$

(b) $A = 12\,\mathrm{V}$ & $\omega/\omega_n = 0.80$

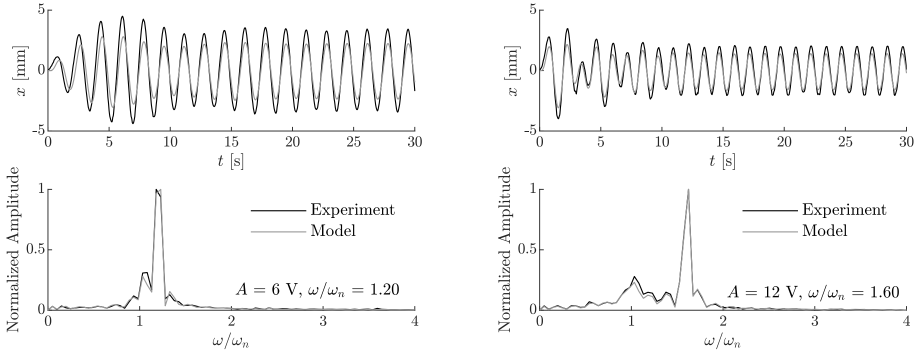

(c) $A = 6\,\mathrm{V}$ & $\omega/\omega_n = 1.20$

(d) $A = 12\,\mathrm{V}$ & $\omega/\omega_n = 1.60$

Figure 3.10: Comparison between numerical simulations and experimental measurements for exemplary excitation cases.

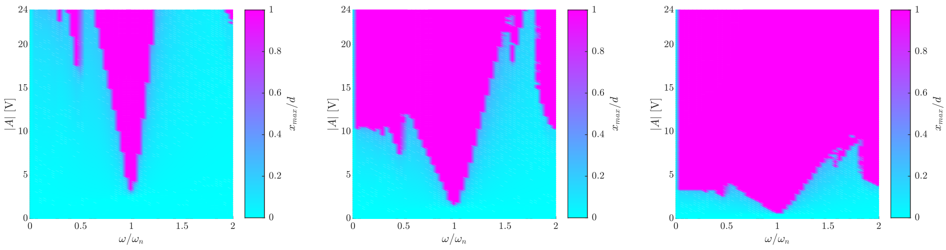

(a) $d = 50\,\mathrm{mm}$

(b) $d = 40\,\mathrm{mm}$

(c) $d = 30\,\mathrm{mm}$

Figure 3.11: Stability map of the dynamic system: Maximum displacement ratio x_{max}/d as a function of excitation amplitude A and frequency ω.

3.4. Conclusions

This chapter presented two models used to develop the proof-of-concept for the contactless technique. Specifically, an elaborate description of the experimental apparatus of a lab-scale magnetic pendulum with external actuation is provided. To create the numerical model counterpart, the external forces acting on the pendulum had to be identified. These forces include the dissipative torque at the pivot point and the electromagnetic interaction. A parametric calibration of the forces against experimental measurements was conducted, yielding a satisfactory representation of the damping force given by Coulomb's friction formula and the interaction between the two magnets as an empirical nonlinear function of the distance. The force of the electromagnetic interaction, though involving an electromagnet and a permanent magnet, exhibits a similar nonlinear relationship to the separation distance as derived from the simple dipole-to-dipole interaction model.

To further validate the prediction of the numerical model, forced vibrations of the dynamical system were studied. The electromagnetic actuator excited the system through an alternating harmonic signal, exploring different frequency and amplitude cases. Overall, the model successfully predicts the physical dynamic behaviour of the system, while the minor discrepancies observed can be attributed to the system's two main nonlinearities. The presence of friction, along with its memory and sensitivity to experimental conditions, can hinder the convergence of the two data sets. Additionally, the operational limits of the electromagnetic device, such as possible delays in alternating the polarity of the actuator due to core magnetization, can be significant at lower excitation amplitudes.

Given the successful calibration of the numerical model and the preliminary study of the electromagnetic interaction of two magnets, the controlled response of the system will be investigated in the following chapter, delving deeper into the limitations and parameters of influence of the control technique.

4

Contactless magnetic control of the translational vibrations of a magnetic pendulum

Following the validation of the numerical model through physical experiments, this chapter delves into the examination of the controlled vibrations of the planar magnetic pendulum. The control algorithm, as outlined in the theoretical foundation, is now integrated into the magneto-mechanical system, leading to the identification of crucial control parameters.

The primary focus of this chapter is the investigation of an efficient position control of the pendulum's motion. Position control is explored through three modes of excitation and control: two distinct modes and a combination thereof. In the first mode, a specific time-varying motion pattern is imposed on the hanging load with a stationary suspension. This motion pattern serves as the desired response of the dynamic system, simulating the relative motion of the target and the mass-crane-vessel system offshore. In the second control mode, the objective is to attenuate external disturbances to maintain a fixed desired position of the suspended mass. This mode explores the controllability range of the technique in the presence of external excitations (e.g., crane tip motions). The third mode introduces a combination of the two preceding control modes, adding complexity to the controlled vibrations that may arise in practical applications due to potential errors in the dynamic positioning (DP) system and the relative motion between the vessel and the fixed

---

Part of this chapter has been published in:
P. Atzampou, P. C. Meijers, A. Tsouvalas, and A. V. Metrikine, "Contactless control of suspended loads for offshore installations: Proof of concept using magnetic interaction," *Journal of Sound and Vibration*, vol. 575, p. 118 246, 2024

installation position. To validate and showcase the predictive capabilities of the numerical model, the results are compared to experimental data.

This chapter starts with the development of a modified PD control algorithm. The response of the controlled system is then analysed across the different control modes, and the controllability ranges of the designed controller are discussed. Finally, conclusions are drawn with respect to the efficiency of the introduced contactless technique.

4.1. Governing equations of a controlled planar magnetic pendulum

To control the translational motion of the magnetic pendulum, a conventional PID controller is employed. The control variable is the intensity of the electromagnetic interaction which is governed by the voltage (c) applied to the electromagnetic actuator. The controller output in the time domain, as derived in Chapter 2 (Equations (2.18) and (2.19)) reads:

$$c = K_p\, e + K_i \int e\, \mathrm{d}t + K_d\, \dot{e}, \text{ with } e = \xi - x_n = (\xi - h) - x. \tag{4.1}$$

K_p, K_i, and K_d represent the gains of the PID controller, while e denotes the error of the measured state $x_n = x + h$ with respect to the global axes. The pivot point is driven horizontally by h and the desired motion reference is given by ξ.

Given the application, the desired position can be a time-varying function, consisting of a summation of different harmonic signals. Thus, it is expected that the integral term of the PID control will not have a considerable influence on the output of the controller, as the overshoot produced by the K_i contribution will be followed by an undershoot, leading, on average, to a negligible shift. The same holds for the case of disturbance rejection at a fixed position (when this position refers to the equilibrium $\xi = 0$). In this control mode, the additional damping force provided by the derivative term of the controller is most decisive for a good control performance. As a result, only the proportional and derivative components of the control output are considered, essentially performing PD control.

According to the general control methodology elaborated upon in Section 2.4, the control output c is multiplied by a correction factor γ, creating a new control output c' given as

$$c' = K_p'(x_n)\, e + K_d'(x_n)\, \dot{e}, \tag{4.2}$$

in which $K_p'(x_n) = \gamma K_p$, and $K_d'(x_n) = \gamma K_d$, while $\gamma = s^3/\alpha$ with $s = d - x_n = (d - h) - x$. The modified PD controller now consists of state-dependent coefficients. Due to the physical limit of the actuator supply voltage, the new control output c' bears saturation limits,

$$\mathrm{sat}(c') = \begin{cases} -24\,\mathrm{V} & \text{if } c' < c'_{\mathrm{limit}^-} = -24\,\mathrm{V}, \\ +24\,\mathrm{V} & \text{if } c' > c'_{\mathrm{limit}^+} = +24\,\mathrm{V}. \end{cases} \tag{4.3}$$

A visual summary of the modified PD controller algorithm is presented in Figure 4.1 as a block diagram.

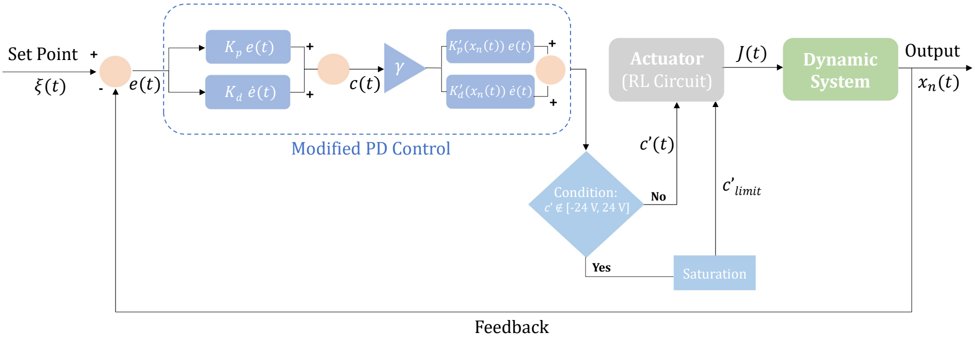

Figure 4.1: Block diagram for the modified PD control.

As established in the parametric calibration of the empirical interaction formula in Chapter 3, the applied voltage prescribed by the modified PD controller is not directly proportional to the current intensity in the electromagnet, but rather is given by Equation (3.9). Incorporating this relation, the controlled vibrations of the pendulum system are described by the following set of equations:

$$\left(M + \frac{m}{3}\right)\ddot{x} + \left(M + \frac{m}{2}\right)\frac{g}{\ell}x = -\left(M + \frac{m}{2}\right)\ddot{h} + \mu\,\mathrm{sgn}\,(\dot{x}) + \frac{\alpha J}{s^3}, \tag{4.4a}$$

$$\dot{J} = \frac{1}{\tau}(c' - J), \tag{4.4b}$$

$$c' = \Big[K_p'\,(\xi - h - x) + K_d'\,(\dot{\xi} - \dot{h} - \dot{x})\Big]_{c'_{\text{limit}^-}}^{c'_{\text{limit}^+}}, \tag{4.4c}$$

where x is the translation of the point mass, h the external excitation of the suspension and c' the control variable.

Due to the nonlinear nature of these equations, the system is analyzed in the time domain. The numerical integration is performed using MATLAB's function *ode45*; an explicit Runge-Kutta method with a variable step (Dormand-Prince method, [95]), which generates the time series of the system's unknown states. The simulations initiate from trivial initial conditions, namely $x = \dot{x} = 0$. To study the controlled vibrations of this system, two distinct modes are considered:

1. *Desired motion control*: Imposition of a desired motion pattern to the suspended mass M;
2. *Disturbance rejection*: Attenuation of the dynamic response of the pendulum mass M when subjected to an external excitation to maintain a desired fixed position.

Moreover, an additional scenario is studied with a more realistic multiple-harmonic suspension point excitation to demonstrate the efficiency of the magnetic manipulation of the nonlinear pendulum. Figure 4.2 illustrates the three variables of interest for the control; the tip motion h, the load displacement x_n, and the relative motion ξ of the crane-load-vessel system with respect to the fixed installation position (monopile head).

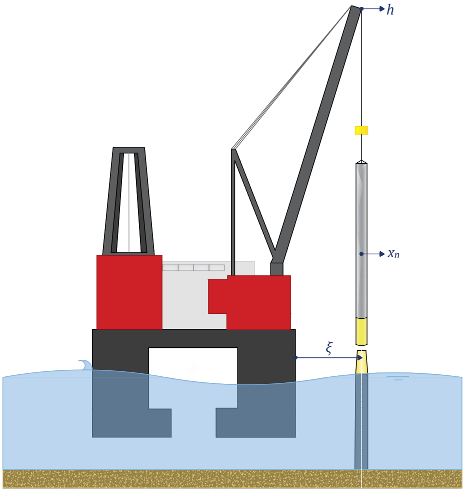

Figure 4.2: Schematic analogue of a tower installation depicting the respective degrees of freedom of the controlled magnetic pendulum analogue presented in Figure 3.1.

4.2. Desired motion control

Desired motion control is defined by imposing a prescribed motion $\xi \neq 0$ to the pendulum mass with a stationary pivot point $h = 0$ (Figure 4.2). This control mode is relevant for floating vessel OWT installations, where the target of the installation (e.g. a monopile) moves relative to the vessel-crane-load system. This motion results from dynamic disturbances (waves, wind, etc.) on the latter system. For this control mode, the desired motion pattern follows a single-harmonic motion: $\xi = A\sin(\omega t)$, where A represents the amplitude and ω is the frequency of the oscillation.

For the activation of the PD control, a set of constant values for the gains K_p and K_d are selected for the simulations. The values of the coefficients are chosen heuristically by means of trial and error, and the results reflect a sufficient level of motion control for the experimental tests. The chosen gains of the PD controller are equal to $K_p = 631$ N/m and $K_d = 100$ Ns/m, respectively. Note that the modified control approach, which employs state-dependent gains, exhibits reduced sensitivity to the gain amplitudes, suggesting a meticulous tuning is less critical [96].

Given the distance-dependent nature of the electromagnetic force, the most deciding variable in terms of control efficiency is the initial separation distance d. Therefore, in Figure 4.3, the displacement time series of the same desired motion pattern ($\omega/\omega_n = 0.6$ and $A = 5$ mm) is presented, but for decreasing initial distance. The numerical simulations are compared to experimental measurements. It is evident that the efficiency of the control (error from the desired reference) improves as d decreases, while the convergence of the experimental and modelled data is satisfactory with the discrepancies attributed to noise and disturbances associated with the physical experiment. Moreover, the optimal separation distance for the case presented is 40 mm, as for the smallest separation distance, the experimental curve appears less smooth (Figure 4.3c). This underscores the importance of accounting for the nonlinearity in the force and establishing an operational range to ensure effective interaction (upper distance limit) while mitigating unwanted unstable behaviour (lower distance limit).

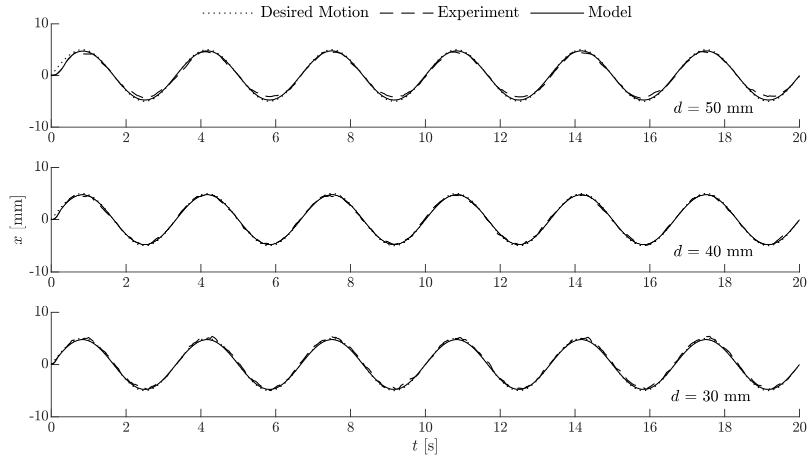

Figure 4.3: Displacement time series of controlled motion for desired harmonic motion pattern with different initial separation distances: (a) $d = 50$ mm, (b) $d = 40$ mm, and (c) $d = 30$ mm.

During the physical experiment, the internal control variables were not registered, and, as a result, it is not possible to directly assess the error, output and saturation level of the controller. Fortunately, the numerical model has proven to be satisfactory in predicting the corresponding physical behaviour. Hence, it is sufficient to draw conclusions on the performance of the controller by considering only the results of the numerical simulations.

An important parameter of the control efficiency is the deviation of the response from the desired motion, i.e. the dynamic position error. In order to achieve a better understanding of the correlation of the error with the modifiable variables of the control (in this case, the frequency of the desired oscillation), a representative value for the error observed in each excitation scenario is derived. This value is the RMS error (e_{RMS}) and is given by [97] as

$$e_{\mathrm{RMS}} = \sqrt{2}\sqrt{\overline{(e-\bar{e})^2}}, \tag{4.5}$$

where e is the steady-state error of the PD control and the overbar symbolises the mean value of the error over the entire time series.

In any case, the physical limits of the actuation system should not be omitted when the overall performance of the control is assessed. When the error becomes higher, the EM compensates by reaching the full capacity of the applied voltage and thus saturates. To quantify this saturation, a saturation level indicator ($\mathcal{S}$) is introduced, which is equal to the percentage of the total time in which the electromagnet functions at the maximum voltage. $\mathcal{S}$ is calculated as

$$\mathcal{S}(\%) = \frac{T_s}{T_{\mathrm{tot}}} \cdot 100\%, \tag{4.6}$$

where T_{tot} is the total duration of the simulation or experimental test, while T_s refers to the cumulative time for which the supply voltage of the EM is above 95% of the physical limit $\left(|c| > 0.95\, c'_{\mathrm{limit}^{\pm}}\right)$.

Figure 4.4a and Figure 4.4b illustrate the error value e_{RMS} and the total saturation τ with respect to the desired frequency of motion and for different initial separation distances. An instantaneous increase of the error is observed at certain frequencies and corresponds well to critical values of the frequency (ω_c) where the controller is abruptly fully saturated. This frequency value differs in the cases studied; the closer the two magnets are located initially, the higher this critical frequency becomes. The critical frequency signifies the cut-off point for an efficient control with the chosen control parameters. In Figure 4.4a, the case of $d = 30$ mm demonstrates a broader frequency range of motion control and a smoother transition from low to higher error values (around $\omega/\omega_n = 2$). Moreover, in terms of saturation (Figure 4.4b), the frequency point of the abrupt change coincides better with the error jump when the separation distance is larger. Hence, moving the actuator closer to the mass M increases the frequency range in which the control operates at full capacity, i.e. maintaining a low deviation from the desired motion pattern. For low frequencies ($f < 0.3$ Hz or $\omega/\omega_n < 0.5$) and for the case of $d = 50$ mm, the controller is saturated for a short time span in the simulation while maintaining a low overall error. This effect is eliminated when the distance between the two magnets is reduced. In short, the control is effective: 1) for $d = 50$ mm, when $0 \leq \omega/\omega_n \leq 1.30$, 2) for $d = 40$ mm, when $0 \leq \omega/\omega_n \leq 1.60$ and 3) for $d = 30$ mm, when $0 \leq \omega/\omega_n \leq 2.05$. The non-proportional relation of the distance and the critical frequency results from the nonlinear nature of the electromagnetic interaction.

In terms of the force exerted by the electromagnet, Figure 4.4c presents the amplitude range of the force solely for the controllable cases of prescribed excitation depending on the initial distance d. The attracting (maximum amplitude) and the repulsive (minimum amplitude) forces are almost symmetric with respect to the mean value of the force, which corresponded to 0 mN. As anticipated, the capacity of the electromagnet's force depends on

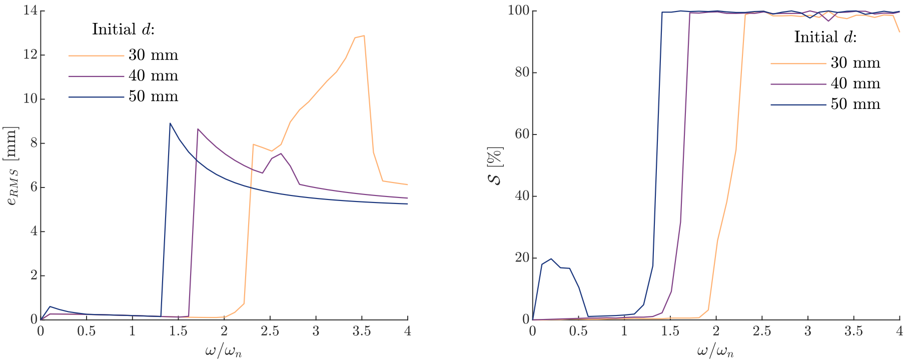

(a) Error e_{RMS} for $A = 5$ mm (b) Total saturation $\mathcal{S}(\%)$ for $A = 5$ mm

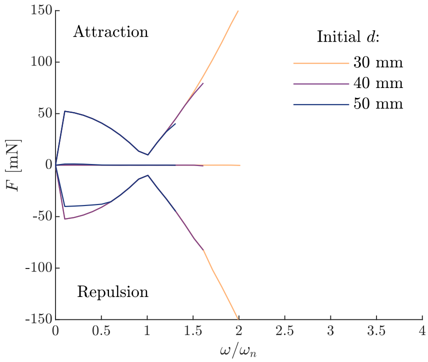

(c) Effective control actuation force F amplitude range for $A = 5$ mm

Figure 4.4: Control efficiency metrics for each frequency of the desired motion control mode.

the distance between the EM and the mass of the pendulum, while the forcing amplitudes are not proportional to the separation distance. Furthermore, for certain low or below resonance frequencies ($\omega/\omega_n \leq 1$) where the error is insignificant, the control can be executed satisfactorily regardless of the separation between the magnets. More specifically, a local minimum of the absolute electromagnetic force is observed at the natural frequency of the uncontrolled system for all different initial separation distances. This observation signifies that the controller is required to apply less force to accomplish the same amplitude of vibration, exploiting the system's resonance.

The highest absolute value of the interaction force is observed for the ratio $\omega/\omega_n = 1.90$ for $d = 30$ mm and is approximately equal to 137 mN. This value corresponds to the unsaturated (effective) control of a simple mass of approximately 1 kg or weight of 10 N. Assuming an equal unit of force per unit weight, the ratio of force per weight is 0.137 N/kg. A typical monopile in the offshore wind park *Prinses Amalia* (Netherlands) has a diameter of 4 m and a total mass of 320 t or weight of 3200 kN [98]. A crude estimation of the maximum forcing amplitude for control would be 0.137 N/kg · 320 × 10^3 kg = 44 kN. This value is comparable to (or even lower than) the force exerted by active tugger lines controlling the installation of OWT blades with a mass of approximately 18 t as derived in [45].

4.2.1. Controllability assessment

When a desired harmonic motion is prescribed to the controlled system, the controller reaches the limiting value for a certain combination of motion amplitude A, motion frequency ω and initial distance d. To derive an expression for the saturation values, the steady-state response of the system is analysed. Assuming the delay of the electromagnet and the nonlinear Coulomb damping are negligible in the steady-state regime, the set of equations of the system given by Equation (4.4) reduce to a single linear equation for the controlled motion, which can be rewritten more concisely as

$$M_t\,\ddot{x} + K_t\,x = K_p\,(\xi - x) + K_d\,(\dot{\xi} - \dot{x}), \tag{4.7}$$

where $M_t = \left(M + \frac{m}{3}\right)$ and $K_t = \left(M + \frac{m}{2}\right)\frac{g}{\ell}$. In this control scenario, the pivot point is considered fixed ($h = 0$) and its objective is to impose a desired motion on the mass, ξ. Evaluating Equation (4.4c) with Equation (4.7), the modified control output is given by

$$c' = \gamma\left(K_p(\xi - x) + K_d(\dot{\xi} - \dot{x})\right) = \gamma\,(M_t\,\ddot{x} + K_t\,x)\,, \tag{4.8}$$

with the parameter $\gamma = (d - x)^3/\alpha$.

The control is effective as long as it remains within the controller limits, i.e. it does not saturate. The first condition ensures that the motion is approximately equal to the desired motion, namely $x \approx \xi = A\sin(\omega t)$ where A is the amplitude and ω is the frequency of the desired response. Substituting this condition into Equation (4.8) yields

$$c' = \frac{Ad^3\left(K_t - \omega^2 M_t\right)}{\alpha}\left(1 - \kappa\sin(\omega t)\right)^3 \sin(\omega t), \tag{4.9}$$

in which $\kappa = A/d$. To check the frequency at which the controller is (partially) saturated, one must check when the amplitude of the control signal is above or below the limit. The second condition pertains to the limit case in which the control output is equal to the physical limit $c'_{\mathrm{limit}^{\pm}}$. Hence, the following expression holds at the critical frequency ω_c:

$$c'_{\mathrm{limit}^{\pm}} = \frac{Ad^3(K_t - \omega_c^2 M_t)Q}{\alpha} \tag{4.10}$$

with $Q = 1 - 3\kappa + 3\kappa^2 - \kappa^3$.

Solving for ω_c gives the following closed-form expression:

$$\frac{\omega_c}{\omega_n} = \sqrt{\frac{\alpha c'_{\text{limit}^{\pm}}}{A K_t d^3 Q} + 1}, \tag{4.11}$$

where only the real-valued solutions of this expression have physical significance. This expression yields the critical frequency by assuming the steady-state response of the undamped controlled system for the conditions of partial or full saturation.

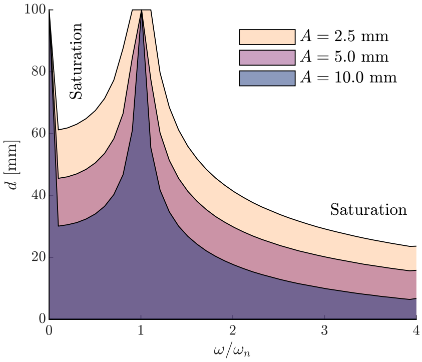

Figure 4.5: Frequency-controllability curves for the desired motion control.

In Figure 4.5, the effective initial distances are plotted against different desired frequencies of motion in order to highlight the area in the parameter space where the control is effective and the actuator is not saturated. It should be noted that, in this figure, the saturated area refers to full capacity regardless of the respective value $\mathcal{S}$ during the simulation. The aforementioned ranges of effective control as well as the non-proportionality with respect to the initial distance are validated. Moreover, for frequencies around ω_n, the control appears to be effective regardless of the choice of the initial distance of the magnets. This effectiveness is also evident in the actuation force shown in Figure 4.4c. Another interesting result is the prediction of partial saturation for $d = 50$ mm and frequency ratios ω/ω_n below 0.5, further linking the saturation with the steady state error e_{SS} (see Figure 4.4a, Figure 4.4b).

4.3. Disturbance rejection control

Disturbance rejection refers to motion compensation that aims to eliminate the suspended mass' response to external excitation of the system, thus keeping the mass M at a fixed position. This control problem is the inverse case of the motion control presented previously. In this section, the pivot point is excited by a prescribed harmonic motion, $h = A\sin(\omega t)$, while the desired position for the payload is constant and equal to $\xi = 0$. A set of constant coefficients for the gains K_p and K_d is selected heuristically by means of trial and error to demonstrate a satisfactory level of control. The gains of the PD controller are equal to $K_p = 5000$ N/m and $K_d = 3000$ Ns/m, respectively.

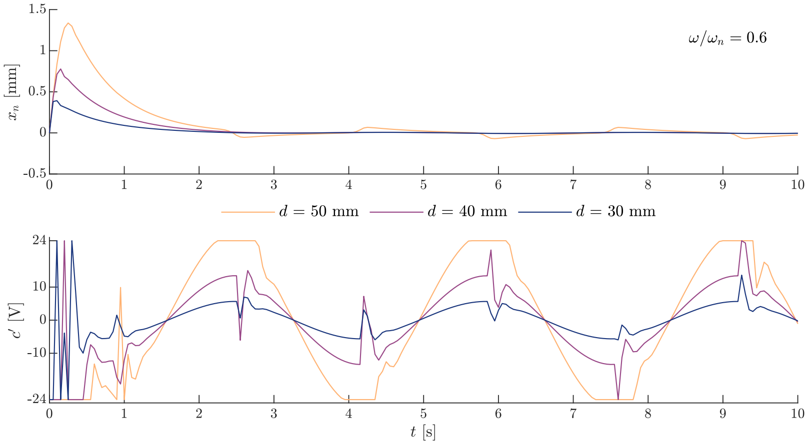

Figure 4.6: Displacement x_n (upper) and control output c' (lower) time series of the controlled motion for a harmonic excitation with $A = 5$ mm and desired position $\xi = 0$ for different initial separation distances d.

For a fixed desired position, $\xi = 0$, the time traces of the controlled motion as well as the respective control output are presented in Figure 4.6 for an exemplary case of excitation with amplitude $A = 5$ mm and an arbitrary frequency ratio $\omega/\omega_n = 0.6$ for three initial distances d. Overall, the controller succeeds in attenuating the externally imposed motion caused by the pivot point and maintain the desired position regardless of the separation distance. However, during the transient response, a large error is observed. As a result, the actuator operates at its limits in order to mitigate the motion. It is noted that the greater the initial distance, the longer the duration of, and the higher the initial, overshoot in the transient. Nevertheless, this part of the response is, from a broader perspective, short in duration (within the order of a few seconds). In the steady-state, a small fluctuation of the error is present, while the level of saturation depends on the initial distance.

Figure 4.7a illustrates the maximum error of the overshoot during the transient response (e_{trans}) and after the steady-state response is reached (e_{SS}) for various initial distances d. The value of e_{trans} is determined by extracting the maximum error within the first 5 s of the simulation. An almost linear relation is observed between the e_{trans} and the frequency ratio ω/ω_n, with a steeper slope as the distance of the two magnets increases. Since the most significant deviations occur during the transient vibrations, an upper limit of acceptable maximum e_{trans} should be set to serve as an additional efficiency condition next to the critical initial distance d_c. In contrast to the transient, the error during the steady-state response appears to be less significant with one order of magnitude difference between e_{SS} and e_{trans}.

The total saturation $\mathcal{S}$ against different pivot excitation frequencies is given by Figure 4.7b. As expected, separation distance d = 50 mm results in the greatest levels of saturation, while for the highest ω/ω_n ratios the controller saturated fully. Moreover, as presented also in the previous control case, the level of saturation of the controller strongly affects the error during the steady-state response. The greatest values of e_{SS} for d = 50 mm occur when the controller reaches its limits. An interesting point can be made for the performance of the controller for smaller d, where there is a constant low $\mathcal{S}$ percentage throughout the range of excitation frequencies. These low values of $\mathcal{S}$ correspond to the saturation present during the transient for the case of pivot excitation with amplitude A = 5 mm.

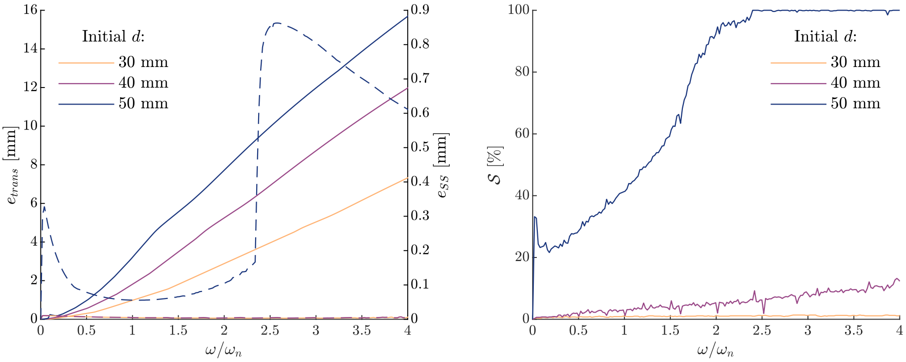

(a) e_{trans} (solid) and e_{SS} (dashed) for A = 5 mm (b) Total saturation $\mathcal{S}$(%) for A = 5 mm

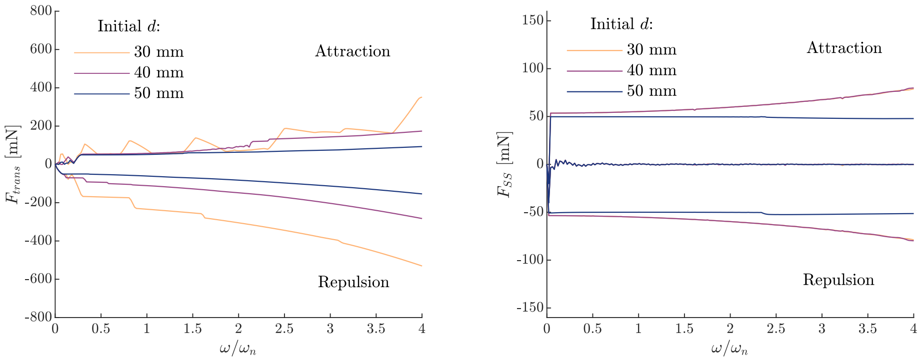

(c) Force range for the transient F_{trans} for A = 5 mm (d) Force range for the steady-state F_{SS} for A = 5 mm

Figure 4.7: Control efficiency metrics for each frequency of the disturbance rejection control mode.

The amplitude range of the force for the transient (F_{trans}) and the steady-state (F_{SS}) controlled response is demonstrated in Figure 4.7c and Figure 4.7d for the different initial distances d, respectively. F_{SS} exhibits the same profile for $d \leq 40$ mm as the control is efficient. For d = 50 mm, due to full saturation and low error, the controller reaches a certain constant value for all frequency ratios. Similar behaviour is observed for the force range

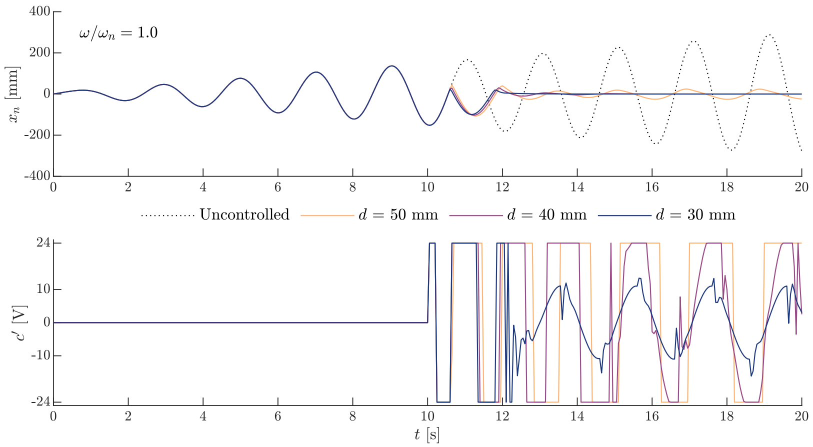

Figure 4.8: Comparison of the motion between the controlled and uncontrolled response for different initial distances d and a harmonic excitation amplitude $A = 10$ mm at resonance.

during the transient response for $d \geq 40$ mm. For $d = 30$ mm, the profile is less smooth and symmetric around the horizontal axis. It appears that the controller reaches higher force amplitudes in the repulsion regime, which can be explained by the coupling of high e_{trans} and small initial d that results in an even smaller separation $s = d - x_n$ between the two magnets, leading to instability.

The highest absolute value of the interaction force is obtained for the ratio $\omega/\omega_n = 4$ and is approximately equal to 530 mN and 80 mN for F_{trans} and F_{SS} respectively. This order of magnitude corresponds to the unsaturated disturbance control of a simple mass of approximately 1 kg or weight of 10 N. For a typical monopile of total mass of 320 t or weight of 3200 kN, the maximum forcing amplitude would amount to 170 kN during the transient and 26 kN for the steady-state response. This difference between the force magnitudes could be resolved by the introduction of additional damping to the system, with the aim of attenuating the transient response peak. In this control mode, the force exerted is higher than when a desired motion is imposed. However, the control is able to attenuate the external perturbation of a larger range of frequencies with success, offering greater controllability. Even for these high forcing amplitudes, the ratio of the control force over the weight of the object remains low, approximately 5%.

Figure 4.8 compares the controlled and uncontrolled response of the system at resonance in order to assess the overall efficiency of the motion compensation technique. The control is activated with a 10 s delay to underline the swift response of the controller. The uncontrolled response corresponds to the motion of the system due to the applied pivot point excitation in the absence of an electromagnet. Overall, significant motion mitigation is achieved even for this high value of excitation amplitude ($A = 10$ mm). Even though the system is excited with its natural frequency, the controller is able to prevent the system from exhibiting resonance.

4.3.1. Controllability assessment

Similarly to the derivation of the previous control mode, and assuming no damping or electromagnet self-impedance, the equation of motion for the controlled system (Equation (4.4)) is reformulated concisely as follows:

$$M_t\,\ddot{x} + K_t\,x = B\,\ddot{h} + K_p\,(\xi - x_n) + K_d\,(\dot{\xi} - \dot{x}_n), \tag{4.12}$$

where $x_n = x + h$ with the prescribed motion of the pivot point being equal to a harmonic sinusoidal motion of amplitude A and frequency ω, given by $h = A\sin(\omega t)$. The coefficient $B = -\left(M + \frac{m}{2}\right)$. Thus, the modified control output c' reads

$$c' = \gamma\left[K_p\,(\xi - h - x) + K_d\,(\dot{\xi} - \dot{h} - \dot{x})\right] = \gamma\,[M_t\,\ddot{x} + K_t\,x - B\,\ddot{h}], \tag{4.13}$$

in which $\gamma = (d - x - h)^3/\alpha$. In this control mode, the desired motion ξ is not a function of time but rather a constant desired position for the mass of the pendulum in the global reference frame. Hence, higher-order derivatives of the desired motion are zero. Moreover, in order to define a criterion for effective control, two conditions need to be met. First, for the error of the control, $e \approx 0$ should apply, and, consequently, the steady-state response of the pendulum can be approximated as $x \approx \xi - h$. After the substitution of the first condition to Equation (4.13) and further simplifications one obtains

$$c' = \gamma\,[M_t\omega^2 A - K_t A + B\omega^2 A]\sin(\omega t) + \gamma\,K_t\xi, \tag{4.14}$$

with $\gamma = (d - \xi)^3/\alpha$. Second, there is a condition for effective control that pertains to the saturation and the limits of the control signal. Saturation occurs when the amplitude of c' is equal to $c_{\text{limit}^\pm}$. As the amplitude of a pure sinusoidal signal is given by the factor in front of the sine function, this condition, if applied to Equation (4.14), yields

$$c_{\text{limit}^\pm} = \frac{(d - \xi)^3}{\alpha}\left[M_t\omega_c^2 A - K_t A + B\omega_c^2 A + K_t\xi\right], \tag{4.15}$$

where ω_c refers to the critical frequency above which the controller saturates partially or fully. Solving for the ratio of the critical frequency over the natural frequency of the system (ω_c/ω_n) gives the following closed-form expression:

$$\frac{\omega_c}{\omega_n} = \sqrt{\frac{\frac{c_{\text{limit}^\pm}}{\gamma A K_t} + 1 - \frac{\xi}{A}}{1 + \frac{B}{M_t}}}, \tag{4.16}$$

where $c_{\text{limit}^\pm}$ is the operational capacity of the electromagnet, A the amplitude of the desired motion, ξ the fixed desired position and d the initial distance.

The denominator of Equation (4.16), $1 + B/M_t$, is always negative because $B < -1$. Thus, a physically-admissible critical frequency ($\omega_c > 0$) can only exist when:

$$\frac{c_{\text{limit}^\pm}}{\gamma A K_t} + 1 - \frac{\xi}{A} < 0 \longrightarrow c_{\text{limit}^\pm} < \frac{(d-\xi)^3}{\alpha} K_t(\xi - A). \tag{4.17}$$

For the special case where the desired position is $\xi = 0$, a condition can be obtained for the critical initial distance d,

$$d < \sqrt[3]{\frac{\alpha \left\| c_{\text{limit}^\pm} \right\|}{K_t A}} = d_c, \tag{4.18}$$

where $\left\| c_{\text{limit}^\pm} \right\|$ signifies the absolute value of the physical limit of the electromagnet. Equation (4.18) is graphically presented in Figure 4.9 for different excitation amplitudes and frequencies.

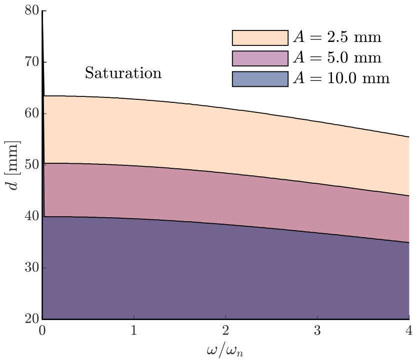

Figure 4.9: Frequency-controllability curves for the disturbance rejection control mode (steady-state response).

By calculating d_c, one obtains the optimum value for d for the static case of $\omega = 0$ rad/s and the maximum initial distance between the magnets without saturation. This critical distance could serve as a conservative criterion for high controllability (low error in the steady-state response and no saturation). Any initial distance value larger than d_c would result in a degree of saturation for the controller, thus reducing the controller's ability to maintain the desired position. Figure 4.9 shows that the control is effective for an extensive range of excitation frequencies, in which the determining parameter is the initial distance. More specifically, at lower frequencies, this critical distance is almost constant or exhibits a small reduction of the order of approximately 5 mm compared to the "static" case ($\omega/\omega_n = 0$). This figure can serve as an indicator for a proper choice of d for successful control depending on the amplitude of the pivot motion. For instance, for the case of $A = 5$ mm and $\omega/\omega_n = 0.6$ presented in Figure 4.6, the control is successful (without saturation and no significant error) for $d < 50$ mm during the steady-state, confirming the validity of the respective controllability curve in Figure 4.9. In Figure 4.8, the controller suppresses instability for $d < 40$ mm as predicted by Figure 4.9, while the disturbance rejection remains effective even at $d = 40$ mm despite the saturation. Thus, there is a small tolerance around the critical value, where the controller can still be efficient (low error) despite being fully saturated. This conservative prediction of d_c aligns with the assumptions made, such as the absence of damping and the actuator's self-inductance.

4.4. Disturbance rejection for a multiple-frequency pivot excitation

Now, a more realistic signal is prescribed as external excitation for the pivot point h of the pendulum. This signal was obtained from a simulation of a full-scale installation of an OWT tower operated by a semi-submersible vessel (*Prometheus*, [44]) with an input sea state generated by a JONSWAP spectrum with significant wave height $H_s = 3$ m and a peak period $T_p = 8$ s. More specifically, the full-scale time response displacement signal h_f of a floating vessel offshore crane tip was scaled in terms of amplitude and time in accordance with the geometry of the experimental set-up by means of Froude scaling [99]. The time series and frequency content of the signals are shown in Figure 4.10, whereas the characteristics of the two systems (full-scale and lab-scale) are presented in Table 4.1. For the full-scale set-up, the dimensions of a typical offshore crane are used.

Table 4.1: Dimension comparison between the experimental and full-scale set-up.

Parameters	Full-scale	Lab-scale	Ratio
Crane length [m]	$L_{c,f} = 140$	$L_{c,s} = 1.22$	$\lambda_c = 8.7 \times 10^{-3}$
Pendulum arm [m]	$L_{p,f} = 80$	$L_{p,s} = 1.04$	–
Natural frequency [Hz]	$f_{n,f} = 0.056$	$f_{n,s} = 0.489$	–

The scaling factor λ_c is defined as the ratio between a typical length in the full-scale and the experimental set-up. Here, this length is the distance between the deck and the sheave on the top of the crane. Then, the motion h_f and the time t_f of the full-scale data are scaled as

$$h_s = \lambda_c \cdot h_f \text{ and } t = \sqrt{\lambda_c} \cdot t_f, \tag{4.19}$$

ensuring that the imposed signal in the simulations has the same frequency content relative to the natural frequency as the full-scale signal. In order to demonstrate the control through simulations, a one-minute fragment of the scaled displacement time series is deduced and is shown as h in Figure 4.10a. Figure 4.10b present the frequency content of the three signals, namely the full-scale crane-tip h_f, the scaled counterpart h_s, and the final crane-tip displacement h imported as excitation to the model. The frequency scale is normalized with the natural frequency of the two (lab-scaled and full-scale) systems respectively. Small discrepancies are observed when comparing the full-scale and scaled signals due to the simplifying assumptions made in calculating the natural frequency of the full-scale dynamical system $f_{n,f}$. The offshore crane-payload system is assumed to be equivalent to a simple point mass pendulum with a massless inflexible arm. In all spectra, multiple frequency components are present and the overall energy corresponds to ratios $\omega/\omega_n > 1$.

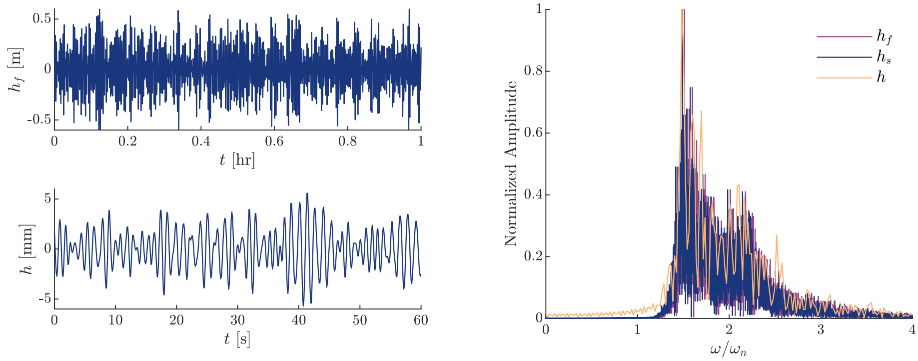

(a) Time series of the crane tip displacement for the full-scale (h_f) and scaled signal (h)

(b) Frequency response of the full-scale (h_f) and scaled signals (h_s & h)

Figure 4.10: Amplitude time series and frequency content of the pivot point excitation signal input.

Figure 4.11 presents the relevant time traces of the controlled motion for different separation distances. For the displacement x_n, an excellent level of attenuation of motion is achieved for all d. The main differences pertain to the transient part of the response, namely the amplitude of the error and the duration of the transient. Reducing the distance, results in a lower error and a shorter transient response, which is in line with the previous results. Moreover, the total level of saturation of the control output c' decreases for $d < 50$ mm.

To assess the total efficiency of the control and to connect it to real-life operations and technical capacities, the consumed power needs to be examined. There are two main power components to be considered:

1. the power required to control the payload which is associated with the work done by the actuation force (P_F) and
2. the electrical power consumed to enable the control actuation (P_I).

The actuation power is defined as

$$P_F = F\dot{x}_n, \tag{4.20}$$

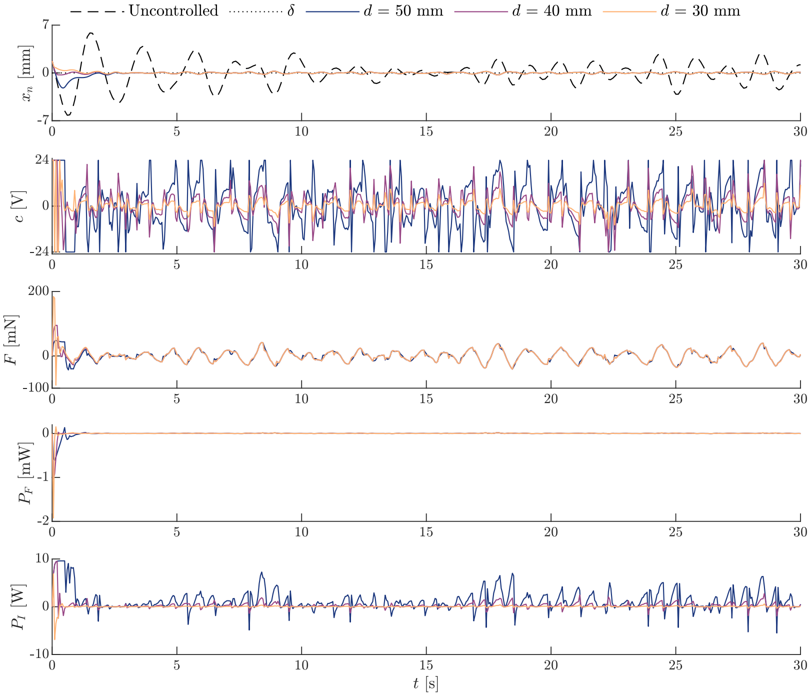

Figure 4.11: Controlled response for the disturbance rejection of a multiple frequency excitation: Times series of the displacement x_n, control output c', control actuation power P_F and electrical power consumed by the actuation P_I.

in which F represents the force of the electromagnetic interaction (Figure 4.11), and $\dot{x}_n$ is the velocity of the mass with respect to the global reference system ($\dot{x}_n = \dot{x}+\dot{h}$). To determine the electrical power input, the resistance R of the feeding electrical circuit is needed, measured at $R = 60$× for the experimental setup. The electrical power is then calculated as

$$P_I = c' \cdot \frac{J}{R}, \tag{4.21}$$

where c' and J are the voltage input and output of the actuator, respectively. P_I is presented in Figure 4.11. As intuitively expected, the electrical power consumed by the controller becomes greater with the initial distance. Integrating the power consumption during the entire simulation yields the cumulative electrical energy $E_{I,\text{tot}}$, which amounts approximately to $E_{I,\text{tot}} \approx [1.30, 8.50, 33.5]$ J for $d = [30, 40, 50]$ mm, respectively. When the control is efficient, during steady-state, the effort of the actuation (P_F) is the same regardless of the separation. Differences are highlighted during the transient, where the response for $d = 30$ mm exhibits the highest work required to achieve low error.

By comparing all the time series reported in Figure 4.11, the most effective control case for this multiple frequency signal is the distance $d = 40$ mm in terms of the error and actuation power and the distance $d = 30$ mm in terms of saturation and electrical power. This discrepancy underlines the importance of consciously selecting the distance not only aiming at less energy consumption but also ensuring the stability and safety of the operation, as the nature of the interaction becomes highly nonlinear with decreasing distance.

4.5. Conclusions

In this chapter, the controlled vibrations of a contactless control technique for the translational motions of a magnetic pendulum subjected to electromagnetic forcing and pivot point excitation are studied. Numerical simulations are validated and calibrated against experiments on a lab scale, as elaborated in Chapter 3. A modified PD controller is employed to enforce a desired motion to the suspended mass by regulating the intensity and polarity of an electromagnet. The key advantage of this modification is that the use of state-dependent gains reduces the need for meticulous tuning.

The technique is successful for two different control modes: the desired motion of the mass with a fixed pivot and the fixed global position with a moving pivot point. Two important control parameters are identified: the saturation of the controller and the separation distance of the two magnets. It is noted that the swifter the transitions between the two polarities during the control, the longer the time where the electromagnet operates at its full capacity, leading to an inferior response. The relative distance between the magnets plays an equally crucial role. When the magnets operate in closer proximity, the performance of the control is significantly improved (lower error and less saturation). Controllability curves are derived analytically to indicate areas of efficient control. These curves serve as nomographs through which the optimum distance between the magnets can be deduced for different combinations of excitation (external excitation or desired motion). Resonance is exploited by the controller when a desired harmonic motion is imposed, while this behaviour is successfully subdued when the controller aims at a fixed position. For the latter control mode, transient response is of great importance for the overall efficiency of the control of the system as it leads to large errors and high saturation levels, which attenuate when steady-state is reached. It is important, therefore, to set an additional criterion for the maximum acceptable error during the transient.

The power required can be also indicative of the optimum choice of initial separation distance for the magnets: with the power of the actuation force being in favour of an intermediate distance, while the electrical power suggests smaller distances as the least energy-demanding. In terms of force amplitude exerted by the actuator, the estimated order of magnitude is comparable to an active tugger line control system, but with a crucial difference: both repulsive and attracting forces are possible, thus allowing for more control authority.

In short, the contactless control technique successfully exploits magnetic interaction to impose a desired motion pattern to a suspended mass. The findings of this chapter focus on the most —intuitively —important degree of freedom of the floating crane-payload dynamical system: the translational vibration of a load in the plane parallel to the seawater level, highlighting the controller's potential. To further develop the technique, particularly for the intended application in OWT installations, it is necessary to address the controllability and control design of additional vibrational modes. This topic is explored in the following chapters.

5

Contactless magnetic control of the torsional vibrations of a hanging monopile

During the installation stage of OWT components, another significant vibration mode arises in the form of rotation around the shaft (vertical axis) of the component. This rotation poses challenges in aligning the pieces accurately, thereby prolonging the overall time needed for component assembly. To investigate a non-contact method to attenuate this vibration, a novel control algorithm strategy is developed. The dynamical system under consideration involves a hanging cylinder rotating around its longitudinal axis.

Critical to the successful deployment of offshore turbines is the installation process and, more specifically, the temporary suspension of the components before their connection to the already installed structure; such as the connection of an OWT tower to the transition piece (TP) of a monopile foundation [101]. Throughout this stage, external environmental excitation or asymmetries in control actuation forces, e.g. active tugger line systems, can induce undesirable vibrations of the suspended component. In conjunction with the translational vibration control of a suspended load introduced in Chapter 4, the vibrations around the longitudinal axis become noteworthy, influencing the overall effectiveness and duration of the installation process. The precise control of this mode is pivotal, especially for connections that necessitate high precision, such as the widely used bolted flange joints. Controlling this vibration of the tower during installation can ensure the accurate align-

---

Part of this chapter has been published in:
P. Atzampou, P. C. Meijers, A. Tsouvalas, and A. V. Metrikine, “Non-contact electromagnetic control of torsional vibrations of a rigid cylinder,” *Nonlinear Dynamics*, vol. 113, no. 3, pp. 2001–2016, 2025

ment required for a safe and effective assembly of OWT components. In this chapter, a contactless rotational control technique is developed, utilising electromagnetic interaction between two magnets, incorporating magnetically-induced damping and motion manipulation principles.

This chapter commences with an overview of the state of the art in rotational control, encompassing technological advancements reported across various engineering fields and scales. Then, the dynamical system is introduced, emphasizing the nonlinear properties of magnet-to-magnet interaction that form the foundation for the proposed control algorithm. A detailed control design is presented and implemented in various control modes, demonstrating the effectiveness of the technique in energy dissipation and the precise control of the cylinder's rotation.

5.1. State of the art in magnetic rotational control

Magnetically induced dissipation finds application across diverse industries in the form of magnetic braking, demonstrating its efficacy in controlling the motion of rotating systems. This method encompasses two techniques: electromagnetic induction-based and magnetic attraction-based braking. Electromagnetic actuators are employed in active magnetic bearings for controlling the rotation of ferromagnetic objects in rotating machinery [102–106]. In the automobile sector, Puttewar et al. [107] elucidated electromagnetic brakes that utilize attractive forces to pull the armature, effectively arresting the rotatory motion of the system. Ou et al. [108] introduced a novel design of eddy current magnetic brakes, driven by Faraday's law of induction and the Lorentz force formula for descent devices using arrays of permanent magnets. This technique is extended to upright magnetic braking for building elevators [109], railway vehicles [110] and seismic vibration control of civil engineering structures [111, 112]. However, in applications such as the installation of OWT, where the components requiring control are made of ferromagnetic materials (e.g. steel), eddy currents are not a viable alternative for efficient rotation braking, as their effectiveness depends heavily on the electrical conductivity properties of the material. Moreover, the use of electromagnetic actuators capable of changing the magnetic field's direction and extracting energy through interaction with a magnetic object has not been thoroughly investigated yet for motion attenuation purposes.

Rotational control has major advancements through the use of magnetic interactions. In biomedical applications, studies have been conducted on the precise control of the motion (translation and rotation) of micro-magnets in arbitrary 3D paths using a group of permanent magnets that could rotate with the help of motors modifying the magnetic field [113–115]. Mahoney & Abbott [116] explored the 5-degree-of-freedom manipulation (motion and orientation control) of a magnetic device using a single rotating permanent magnet attached to a robotic arm actuator. The aerospace industry has also leveraged rotational magnetic control for satellites, namely for attitude control and stabilization. In this setting, the control is based on the interaction of three orthogonal current-driven magnetic coils with the Earth's magnetic field [117, 118]. Despite the multiple degrees of freedom and the high level of controllability exhibited, these applications pertain to systems of smaller scales, ranging from micro [119] to nano-scale [120].

The present chapter introduces and investigates the efficient contactless rotational control of a cylinder around its shaft (longitudinal axis). The control relies on the interaction between a permanent magnet attached to the cylinder and an electromagnetic actuator positioned at a fixed distance from the cylinder's surface, similar to the translational control. Through manipulation of the orientation of the magnetic field of the actuator, fundamental characteristics of the system can be altered, including its natural frequency (through magnetically-imposed stiffness [121, 122]) and the equilibrium position. Three distinct control modes are addressed herein:

1. *Damping control*: Motion attenuation of a rotating cross-section of a cylinder through magnetic interaction, introducing a nonlinear dissipative force to the dynamical system;
2. *Active rotation control*: Active rotational control and the imposition of a desired angle for the cross-section of the cylinder;
3. *Active torsional vibrations control*: Imposition of a time-varying desired rotation.

5.2. Dynamical system & Governing equations

A sketch of a floating offshore OWT installation operation is presented in Figure 5.1a. Here, the degree of freedom that the controller will address is the rotation around the longitudinal axis of the tower (ϕ). In order to create the base case for the proof of concept of the control technique, the aforementioned system is transformed into a simplified, yet equivalent, scaled-down system, which is presented in Figure 5.1b. The equivalent dynamical system is comprised of a ring of total mass m, wall thickness τ_r, and outer radius R that is free to rotate around its origin. The studied configuration resembles a cross-section of the suspended tower (as observed from above), while the rotational spring element with stiffness k_s represents the stiffness of the attached cables of the crane. The set-up pertains to a single degree of freedom system with two unknown states, namely the angle of rotation ϕ and the angular velocity $\dot{\phi}$. A permanent magnet (PM) is attached to the circumference of the ring at $\phi = 0^\circ$ (static equilibrium, referring to the system's resting position in the absence of any magnetic forcing), coinciding with the equilibrium of the uncontrolled system. The dipole moment $\vec{m}_c$ describes the orientation and the strength of the PM. While the strength of the dipole moment of the PM (M_c) is constant, the orientation is forced to follow the rotation of the ring ϕ (Figure 5.1b). An electromagnetic actuator (EM) is placed on the global x-axis at a given distance d from the PM. The dipole moment of the EM is given as $\vec{m}_f$ and its polarity as M_f. The orientation of the magnetic dipole of the electromagnetic actuator is represented by the angle θ as shown in Figure 5.1b. The parameters of the set-up are quantitatively presented in Table 5.1. The selected values correspond to a full-scale offshore crane-tower system, scaled down to 1/100 to facilitate the laboratory experiments [123].

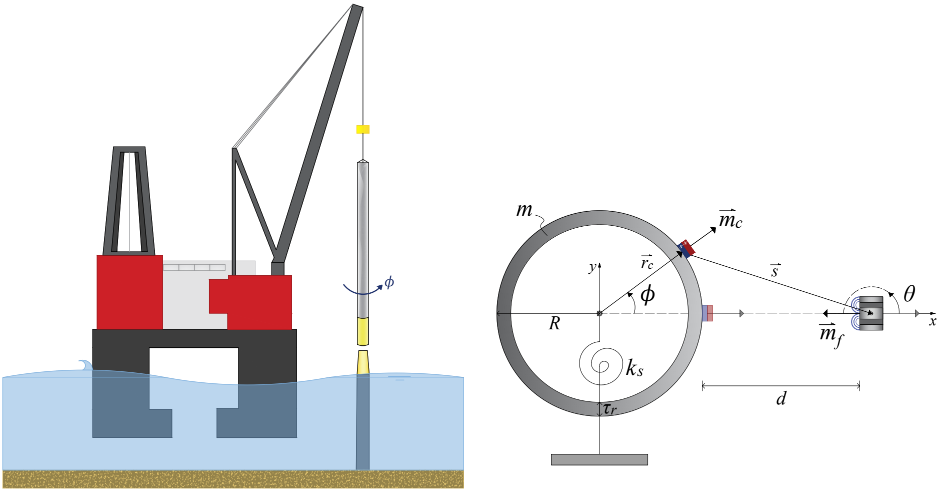

(a)

(b)

Figure 5.1: (a) Full-scale dynamical system of a tower installation with the torsional degree of freedom notated, (b) Schematic diagram of the lab-scale analogue dynamical system. The ring resembles a cross-section of the tower, while the rotational spring represents the stiffness of the crane cable suspension.

Table 5.1: Set-up parameters of the SDOF system.

m [kg]	R [mm]	τ_r [mm]	k_s [N mm/°]	I_z [kg mm^2]	ω_n [rad/s]	f_n [Hz]
0.2	20.0	2.0	50	36.2	37.2	5.9

The equation of motion (EOM) that governs the angular position of the rotating ring derived by means of the Euler-Lagrange method (Chapter 2, Equation (2.5)) reads:

$$I_z\ddot{\phi} + k_s\phi = T, \tag{5.1}$$

where I_z is the mass moment of inertia of the ring around its centre, and T is the total external torque acting on the system. The undamped natural frequency (f_n) of the dynamical system is equal to

$$f_n = \frac{\omega_n}{2\pi} = \frac{1}{2\pi}\sqrt{\frac{k_s}{I_z}}, \tag{5.2}$$

while the chosen numerical values are given in Table 5.1.

In the absence of an additional damping mechanism, the external torque T is equal to the torque induced by the magnetic interaction, which is calculated as follows:

$$T = -\frac{\partial W_m}{\partial \phi}, \tag{5.3}$$

where W_m is the contribution of the two interacting magnetic dipoles to the potential energy. W_m is equal to

$$W_m = -\vec{m}_c \cdot \vec{B}_{fc}, \tag{5.4}$$

in which $\vec{B}_{fc}$ is the magnetic field generated by the EM at the location of the PM on the ring. The external torque can be expressed as

$$T = \hat{k} \cdot \left(\vec{T}_m + \left(\vec{r}_c \times \vec{F}_m\right)\right), \tag{5.5}$$

where $\hat{k}$ represents the unit vector of the z-axis (perpendicular to the xy-plane), $\vec{r}_c$ denotes the vector from the centre of the cylinder to the location of the EM. The expressions for the force $\vec{F}_m$ (exerted by one dipole on another, [124]) and the torque $\vec{T}_m$ (acting around the centre of the dipole generated to align it to the field lines, [125]) are given by

$$\vec{T}_m = \vec{m}_c \times \vec{B}_{fc}, \tag{5.6a}$$

$$\vec{F}_m = \vec{\nabla}\left(\vec{m}_c \cdot \vec{B}_{fc}\right), \tag{5.6b}$$

with $\vec{B}_{fc}$ being equal to

$$\vec{B}_{fc} = -\frac{\mu_0}{4\pi}\vec{\nabla}\frac{\vec{m}_f \cdot \vec{s}}{s^3}. \tag{5.7}$$

The vector representing the separation distance between the two dipoles is denoted as $\vec{s}$ (Figure 5.1b). It is noted that the circumflex ˆ indicates a unit vector, and a plain character indicates the magnitude of a vector (e.g. $\vec{s} = s\,\hat{s}$).

Figure 5.2 illustrates the magnetic field $\vec{B}_{fc}$ generated by the EM, represented by arrows depicting the field lines and their respective directions. These arrows correspond to normalized values of $\vec{B}_{fc}$ in space, appearing uniform in size. The contour background of the figure indicates the areas of higher magnetic field strength, with its peak centred at the EM's position. Additionally, white concentric circles and white (round-tip) arrows represent the ring and the orientation of the magnetic dipoles of both the EM and PM respectively. Figure 5.2a demonstrates the magnetic field generated when the two dipoles are aligned with positive polarities, i.e. the magnets attract each other. An interesting property of the system is observed when the field of the EM is subjected to rotation by a positive (counter-clockwise) angle. In the absence of the linear spring ($k_s = 0$) and in the presence of linear damping ($T_d = -c_d\dot{\phi}$ with $c_d > 0$), the system rotates and eventually comes to rest at a new static equilibrium position, in this case corresponding to a negative angle (and vice-versa for a negative rotation of the EM dipole), as depicted in Figure 5.2b. The PM dipole adjusts its orientation to align with the external magnetic field lines.

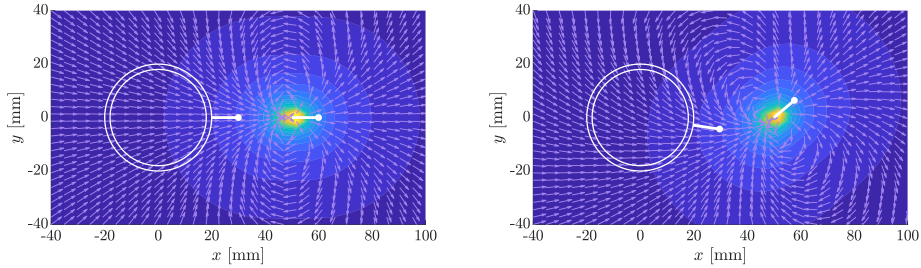

(a) $\theta = 0^\circ$ (b) $\theta = 40^\circ$

Figure 5.2: Spatial distribution of the magnetic field generated by the electromagnetic actuator for different orientations of its field θ.

5.3. Potential energy & Equilibrium position

To further investigate this property, analysis of the potential energy of the dynamical system is essential. The total potential energy of the system is a summation of the potential energy of the spring (W_s) and the magnetic interaction (W_m), and reads

$$\mathcal{U} = W_s + W_m, \tag{5.8}$$

with:

$$W_s = \frac{1}{2} k_s \phi^2. \tag{5.9}$$

The dynamical system without an external magnet has a static equilibrium dictated solely by the spring element, namely at $\phi = 0^\circ$. Due to the interaction of the two magnets, there is an additional contribution on the potential energy W_m (substituting Equation (5.7) to Equation (5.4)), which reads

$$W_m = -\vec{m}_c \cdot \vec{B}_{fc} \tag{5.10a}$$

$$= \frac{\mu_0 M_c M_f}{4\pi s^3} \left(\cos(\theta - \phi) + \frac{\Big(3R\cos(\theta-\phi) - 3\cos(\theta)(R+d)\Big)\Big(\cos(\phi)(R+d) - R\Big)}{s^2} \right), \tag{5.10b}$$

where s is calculated by

$$s = \sqrt{(R\sin(\phi))^2 + (R + d - R\cos(\phi))^2}, \tag{5.11}$$

and the magnetic dipoles are given by

$$\vec{m}_f = M_f \begin{bmatrix} \cos(\theta) \\ \sin(\theta) \end{bmatrix} \text{ and } \vec{m}_c = M_c \begin{bmatrix} \cos(\phi) \\ \sin(\phi) \end{bmatrix}. \tag{5.12}$$

Evaluating Equation (5.10a) using the Taylor series expansions of the trigonometric terms of ϕ up to the second order around $\phi = 0°$ yields

$$W_m = K_{m_1}\phi^2 + K_{m_2}\phi + C, \tag{5.13}$$

with:

$$K_{m_1} = \frac{\mu_0 M_c M_f}{4\pi d^5}(6R^2 + 6Rd + d^2)\cos(\theta), \tag{5.14a}$$

$$K_{m_2} = \frac{\mu_0 M_c M_f}{4\pi d^5}(3Rd + d^2)\sin(\theta), \tag{5.14b}$$

$$C = -\frac{\mu_0 M_c M_f}{2\pi d^5}d^2\cos(\theta). \tag{5.14c}$$

The truncated series representation of the potential energy W_m (Equations (5.13) and (5.14)) illustrates the presence of coupled nonlinear contributions of the rotations of the two dipoles to the potential energy of the system. The magnitude of the magnetically induced potential energy is proportional to the product of the dipole strengths ($M_f M_c$) and decays as the distance between the two magnets (d) increases.

The equilibrium position of the rotating dynamical system (ϕ_e) is determined by

$$\left.\frac{\partial \mathcal{U}}{\partial \phi}\right|_{\phi=\phi_e} = 0 \rightarrow 2K_{m_1}\phi_e + K_{m_2} + k_s\phi_e = 0. \tag{5.15}$$

Solving for ϕ_e yields

$$\phi_e = -\frac{K_{m_2}}{(2K_{m_1} + k_s)}. \tag{5.16}$$

It is noted that the equilibrium position is governed by the magnetic interaction when the following condition holds:

$$k_s/K_{m_1} \ll 2. \tag{5.17}$$

In this case, k_s can be dropped from Equation (5.16) and the closed-form prediction formula for ϕ_e becomes

$$\phi_e = -\frac{1}{2}\left(\frac{3Rd + d^2}{6R^2 + 6Rd + d^2}\right)\tan(\theta_e), \tag{5.18}$$

where θ_e represents the respective external magnetic field orientation angle to impose the new equilibrium.

Figure 5.3a shows the nonlinear magnetic potential energy given by Equation (5.10a) for different ranges of the angles θ and ϕ, illustrating the potential wells for different angles of rotation of the EM. The equilibrium positions are determined by the local minima of the potential energy. The area with the lowest potential energy (stable equilibrium positions) is located in the centre of the plot, confirming that the deepest potential well (and thus most stable equilibrium position) is in fact $\phi_e = 0^\circ$. This equilibrium corresponds to an EM dipole orientation angle $\theta_e = 0^\circ$. This scenario corresponds to the perfect alignment of the field lines in attraction. However, when the EM dipole is rotated ($\theta \neq 0^\circ$), the position of the stable equilibrium shifts, validating the observation made in Figure 5.2. The observed rule is that a positive rotation of θ_e results in a negative (but not linearly proportional to θ_e) angle ϕ_e as equilibrium position for the system, and vice-versa.

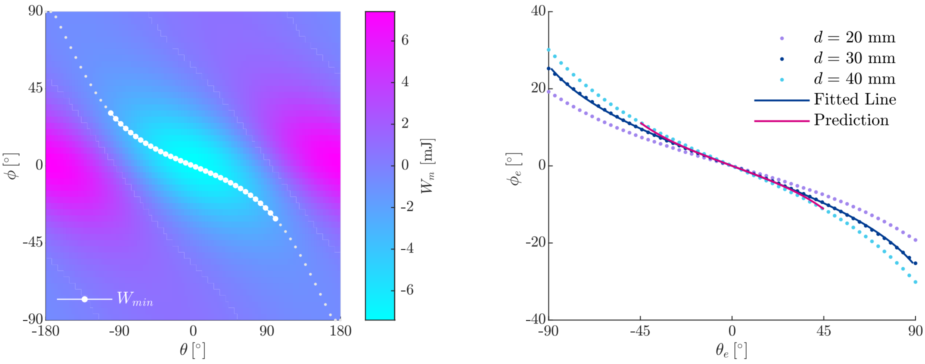

(a) (b)

Figure 5.3: (a) Potential energy of the dipole W_m for different angles θ and ϕ for $d = 30$ mm, (b) Fitting functions for the prediction of the new equilibrium point ϕ_e and corresponding external magnetic field orientation θ_e for different d.

In Figure 5.3a, the white dotted line connects the lowest points of the potential wells. All these points correspond to the modified equilibrium position ϕ_e for each respective θ_e. Figure 5.3b displays these lines for different distances d, alongside the formula predicting the equilibrium positions as given by Equation (5.18). The latter approximation, as expected, provides a good prediction of the equilibrium positions around $\phi = 0^\circ$, namely for $-6^\circ < \phi_e < 6^\circ$. Therefore, a function that provides a better fit to the data reads

$$\phi_e = A(d)\,\operatorname{arctanh}\left(B(d)\,\theta_e\right), \tag{5.19}$$

where for $d = 30$ mm, the coefficients of the function are equal to $A = 22.22^\circ$ and $B = -0.0092\,/^\circ$. It is noted that the range of the desired fixed angles in Figure 5.3b is $-40^\circ < \phi_e < 40^\circ$. This interval corresponds to the range of stable equilibrium angles ϕ_e, namely the adequately deep local minima of the potential (Figure 5.3a). Thus, Equation (5.19) is chosen to describe the relation between the equilibria and the orientation of the external field in the numerical simulations.

5.4. Damping control of rotational vibrations

Damping control involves attenuating the vibrations of the system (resulting from non-trivial initial conditions) to reach the static (intrinsic) equilibrium. The control is based on the introduction of an energy dissipation mechanism into the system using contactless means, namely the magnetic interaction of the PM on the ring and the EM. This control mode is important to initiate the development of the rotation control algorithm envisioned in offshore wind installations. The full-scale counterpart of this mode is the attenuation of the torsional vibrations of a cross-section of a suspended cylindrical structure (resembling an OWT monopile or tower).

5.4.1. Analysis of the linearized EOM around the intrinsic static equilibrium

To devise a control algorithm for the case where the equilibrium of the system aligns with the desired resting position (control set-point), namely when $\phi_e = 0^\circ$ and $\theta_e = 0^\circ$, it is essential to examine the linearized EOM (valid for small angles ϕ) as given by Equation (5.1), Equation (5.3) and Equation (5.13),

$$I_z\ddot{\phi} + (2K_{m_1} + k_s)\phi + K_{m_2} = 0, \tag{5.20}$$

with K_{m_1} and K_{m_2} given by Equation (5.14a) and Equation (5.14b), respectively.

The magnetic interaction between the two dipoles contributes to the stiffness of the system through an additional term K_{m_1}. The coefficient K_{m_1} (for $|\theta| < 90^\circ$) is positive when the product of dipole strengths $M_c M_f$ is positive. Additionally, K_{m_2} is a term independent of ϕ, and its sign is determined by either the orientation θ or the polarity M_f of the electromagnetic dipole when $M_c > 0$.

5.4.2. Control strategy

Motion attenuation within the system can be achieved through a damping mechanism. Coulomb friction is a non-linear dissipative force characterized by the following form [126]:

$$D = \mu_s \,\mathrm{sgn}\,(v), \tag{5.21}$$

where μ_s represents the kinetic friction coefficient and v denotes the velocity. This force acts as a constant force with a sign opposing the velocity of the system. By examining Equation (5.14b), a force resembling Coulomb friction can be introduced into the system (through K_{m_2}) either by alternating the polarity M_f or by modifying the orientation of the external field θ.

Considering the polarity of the actuator as the control variable of the system leads to the adoption of the following expression: $M_f = M_{f_0}\,\mathrm{sgn}(\dot{\phi})$, where M_{f_0} corresponds to the initial absolute value of the strength of the EM. Additionally, the orientation angle θ is chosen to be equal to $\theta = \theta_0$, where θ_0 can be any arbitrary, but small, non-zero angle. While this orientation ensures that the damping term K_{m_2} is not eliminated (see Equation (5.14b)), it conflicts with the optimal orientation for the intrinsic equilibrium, according to which the two dipoles are aligned to impose $\phi_e = 0^\circ$. It is noted that M_f also dictates the sign of the additional magnetically-induced stiffness K_{m_1}. To avoid the occurrence of negative stiffness, which could lead to instability, the stiffness coefficients must satisfy the following condition:

$$\max(|K_{m_1}|) < \frac{k_s}{2} \rightarrow M_{f_0} M_c < \frac{2\pi d^5 k_s}{\mu_0(6R^2 + 6Rd + d^2)}, \tag{5.22}$$

in which, for the given system parameters, $M_{f_0} M_c < 0.88$ is required. Selecting any electromagnetic strength within this specified range results in a stiffness ratio of $k_s/K_{m_1} > 2$, opposing the condition in Equation (5.17) for a magnetically-governed response, leading to an overall impractical control solution.

Thus, in order to avoid instability and ensure practical controllability, the control variable is chosen to be the orientation of the field generated by the EM, which is allowed to fluctuate around $\theta_e = 0^\circ$ with a certain predefined small step $\pm\Delta\theta$. The sign of $\Delta\theta$ is determined by the direction of the angular velocity $\dot{\phi}$, resulting in θ following the rule

$$\theta = \Delta\theta\ \mathrm{sgn}\,(\dot{\phi}). \tag{5.23}$$

For each time step, the controller selects from a number of predefined cases depending on the error from the desired angular position ($e = \phi_e - \phi$). The control cases are:

- Case 0: No action taken ($M_f, \theta = 0^\circ$), when the damping control is successful and the attenuated response is within negligible amplitude bounds ($e < 0.5^\circ$ and $\dot{e} < 50^\circ/s$), and
- Case 1: Positive EM rotation ($M_f, \theta = +\Delta\theta$), or
- Case 2: Negative EM rotation ($M_f, \theta = -\Delta\theta$).

Figure 5.4 illustrates the damping control strategy scheme adopted based on the aforementioned cases and the phase-space quadrants, ensuring motion attenuation. The small fluctuation of the EM dipole orientation aims to generate a torque that opposes the motion of the system, by introducing a force resembling Coulomb friction.

In the examined control scenario, the system initiates from non-trivial initial conditions ($\phi_0, \dot{\phi}_0$). The desired equilibrium position ϕ_e is set to zero. Euler Forward numerical integration is used to solve the full nonlinear equations of the system, with a time step equal to $\Delta t = 2 \times 10^{-5}$ s, which corresponds to a control frequency $f_s = 50$ kHz. The dynamical system's parameters for the damping control mode are given in Table 5.2.

Table 5.2: System parameters for the damping control mode.

$M_f M_c$ [$\mathrm{A^2m^4}$]	d [mm]	ϕ_e [°]	θ_e [°]	ϕ_0 [°]	$\dot{\phi}_0$ [°/s]	$\Delta\theta$ [°]
5	30	0	0	-10	-100	5

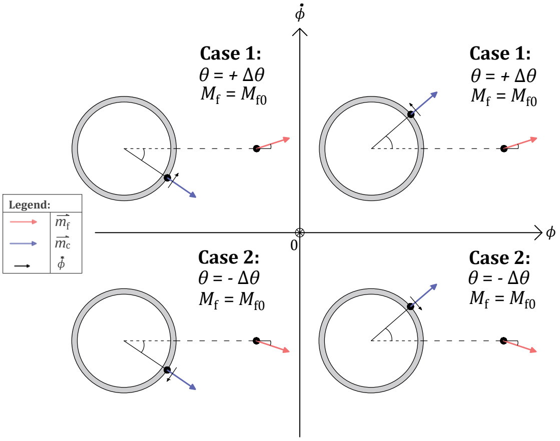

Figure 5.4: Phase portrait of the damping control scheme detailing the control cases per quadrant.

5.4.3. Damping control results

Figure 5.5a presents the relevant time traces of the controlled motion juxtaposed with the uncontrolled ($\Delta\theta = K_{m_2} = 0$) and linearly damped ($\Delta\theta = 0°$ and $K_{m_2} = c_d\dot{\phi}$ with $c_d = 0.4$ N mm s/°) responses. The controller shows a high level of performance with respect to the attenuation of the rotation angle ϕ and the angular velocity $\dot{\phi}$. The presence of nonlinear damping in the controlled response of the system is apparent from the linear decay of oscillations compared to the exponential decay of the linearly damped response. The linear envelope confirms the presence of Coulomb friction in the system [90].

In the time series of the power ($P = T\dot{\phi}$) shown in Figure 5.5a, kinetic energy is both extracted and added to the system, which is attributed to the spring-like force introduced to the system by the additional stiffness terms. It is noted that the extraction of energy solely arises from fluctuations in the sign of $\Delta\theta$, which manifest as small-amplitude discontinuities present in the peaks of the torque T. Furthermore, the contribution of magnetic interaction to the stiffness is evident in the change of the natural frequency of the system when comparing the uncontrolled and controlled response. Finally, the magnetic torque required for control is of low amplitude and, as expected, opposes rotation.

The dissipation of motion is explicitly depicted in Figure 5.5b, where the phase portrait of the controlled response and the different control cases are illustrated as an inward-spiralling path, contrasting the circular trajectory of the equivalent uncontrolled free vibration. This spiral pattern signifies the presence of damping in the system. Notably, the system states effectively converge to the equilibrium position, $\phi = 0^\circ$ with a small steady-state error of $e \approx 0.4^\circ$. For reference, a linearly damped response with a similar decay rate further illustrates the nonlinear nature of the magnetically induced damping.

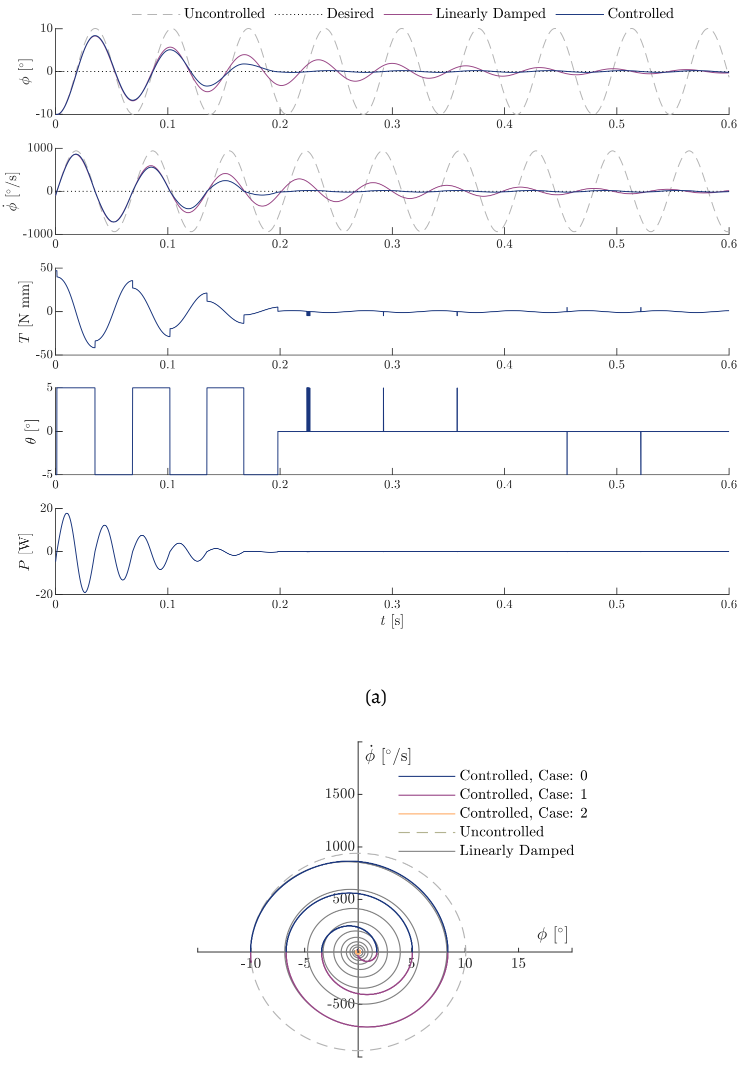

(a)

(b)

Figure 5.5: Damping control system's response: (a) Times series of the rotation ϕ and the angular velocity $\dot{\phi}$ of the ring, the actuation torque T, the orientation θ, and the power of the magnetic interaction P, (b) Phase portrait of the system's response in the damping control mode.

5.5. Active rotation control

Active rotation control is defined as the imposition of a desired constant angle ϕ_e of the ring while attenuating the transient response of the system to a set of initial conditions. The desired constant angular position does not coincide with the system's static equilibrium. This mode combines the damping control with active equilibrium manipulation. In real installations, such a controller would be advantageous for component connections that require high precision, such as the bolted flanged connections between the tower and the monopile of an offshore wind power generator.

5.5.1. Analysis of the linearized EOM around the desired equilibrium

A similar control strategy to the damping control can be applied to this control mode, provided that the following transformation is applied:

$$\phi = \bar{\phi} + \phi_e, \tag{5.24}$$

where $\bar{\phi}$ represents the angular position of the PM relative to the desired equilibrium frame of reference, as depicted in Figure 5.6.

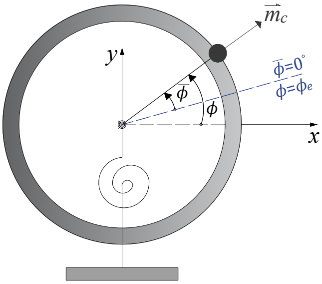

Figure 5.6: Definition of the global ϕ and relative $\bar{\phi}$ angle of rotation.

Substituting Equation (5.24) into the magnetic potential energy W_m Equation (5.10a) and expanding the subsequent trigonometric terms of ϕ up to the second order around the relative equilibrium $\bar{\phi} = 0^\circ$, under the assumptions that ϕ_e is small, yields

$$I_z\ddot{\bar{\phi}} + (2K_{m_1} + \Delta K_{m_1} + k_s)\bar{\phi} + (K_{m_2} + \Delta K_{m_2}) = 0, \tag{5.25}$$

where K_{m_1} and K_{m_2} are given by Equations (5.14a) and (5.14b) respectively, while

$$\Delta K_{m_1} = -\frac{\mu_0 M_c M_f}{4\pi d^6}\,\phi_e\,(45R^3 + 63R^2 d + 21Rd^2 + d^3)\,\sin(\theta), \tag{5.26a}$$

$$\Delta K_{m_2} = +\frac{\mu_0 M_c M_f}{4\pi d^5}\,\phi_e\,(12R^2 + 12Rd + 2d^2)\,\cos(\theta) = 2K_{m_1}\phi_e. \tag{5.26b}$$

To impose a new equilibrium that differs from the inherent equilibrium of the system without the magnetic interaction, an additional contribution to the magnetic and spring stiffness is introduced denoted as ΔK_{m_1}. According to Equation (5.26a), ΔK_{m_1} acts as a positive contribution to the stiffness, as ϕ_e and the respective θ_e of rotation of the field of the electromagnet have opposite directions. This overall positive additional stiffness prevents the introduction of instability to the dynamical system. Similar to the damping control presented in Section 5.4.2, a dissipative force is introduced to the system through the state-dependent term $K_{m_2} + \Delta K_{m_2}$. Note that both additional terms introduced are explicitly dependent on ϕ_e (Equation (5.26)).

Substituting the equilibrium position ϕ_e (Equation (5.16)) as derived by the linearized EOM into Equation (5.26b) yields

$$\Delta K_{m_2} = -\frac{2K_{m_1}K_{m_2}}{2K_{m_1} + k_s}. \tag{5.27}$$

Thus, according to the analysis of the linearised EOM and potential, the state-independent term ΔK_{m_2} is present only when $k_s > 0$.

5.5.2. Control strategy

Similar to the damping control, the angle of rotation of the electromagnetic field θ serves as the control variable and it follows the rule:

$$\theta = \theta_e + \Delta\theta \ \mathrm{sgn}\,(\dot{\phi}), \tag{5.28}$$

where θ_e corresponds to the orientation angle required to impose the new desired equilibrium. This value is determined by solving Equation (5.19) for the desired ϕ_e and the parameters of the system.

Provided that the desired angle of rotation of the ring does not coincide with the static equilibrium of the system, the methodology outlined in Section 5.3 becomes instrumental. Here, for the initial angle of the EM holds: $\theta = \theta_e \neq 0°$. The specific value of θ_e is determined by evaluating Equation (5.19) with the prescribed distance d and desired new equilibrium angle ϕ_e. The dynamical system's parameters for the active control mode are given in Table 5.3.

This control mode consists of two separate actions: the imposition of the new desired equilibrium position and the attenuation of the system's response to the initial conditions. The torque generated by the rotating magnetic field of the actuator consists of a static component due to the constant desired angle θ_e and the additional contribution arising from the modification of this angle $\Delta\theta$. The controller is required to extract ($P < 0$) or add ($P > 0$) energy as necessary to stabilize the system at the chosen new equilibrium position. Therefore, the controller can choose to act according to predefined cases for each time step depending on the error from the desired angular position ($e = \phi_e - \phi = -\bar{\phi}$). include:

- Case 0: No action taken ($M_f, \theta = \theta_e$), when the control was successful and the attenuated response is within certain acceptable amplitude bounds ($e < 1.5°$ and $\dot{e} < 150°/s$), and
- Case 1: Positive EM rotation $\Delta\theta$ ($M_f, \theta_e + \Delta\theta$), or
- Case 2: Negative EM rotation $\Delta\theta$ ($M_f, \theta_e - \Delta\theta$).

Figure 5.7 illustrates the active control strategy scheme adopted based on the aforementioned cases and the phase-space quadrants, ensuring the condition: $\phi \approx \phi_e$. The controller generates a torque opposite to the system's rotation when the PM deviates from the desired reference angle, with the intention of restoring it to the new equilibrium. The nonlinear EOM is solved through the Euler forward numerical integration with a time step equal to $\Delta t = 2 \times 10^{-5}$ s which corresponds to a control frequency $f_s = 50$ kHz.

Table 5.3: System parameters for active control mode.

$M_f M_c$ [A^{2}m^4]	d [mm]	ϕ_e [°]	θ_e [°]	ϕ_0 [°]	$\dot{\phi}_0$ [°/s]	$\Delta\theta$ [°]
50	30	20	-78.3	-10	-100	5

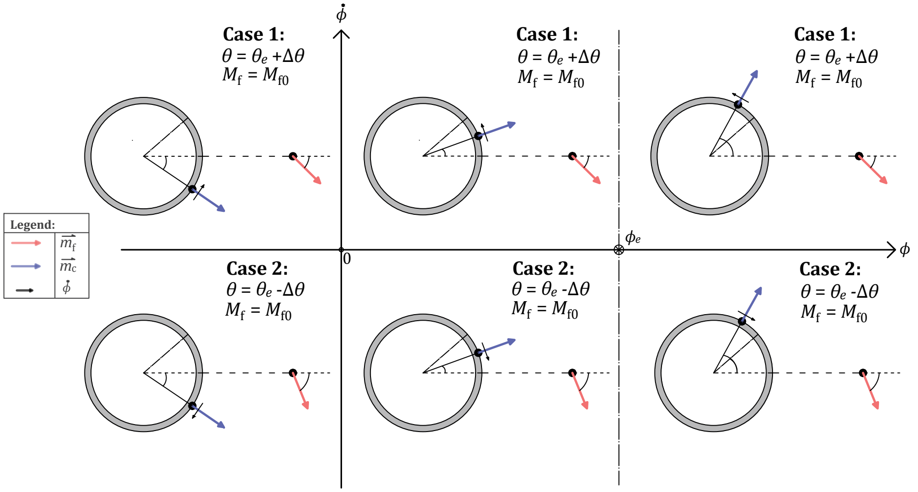

Figure 5.7: Phase portrait of the active control scheme detailing the control cases per quadrant.

5.5.3. Active rotational control results

The time traces of the controlled motion are presented in Figure 5.8a. The controller successfully imposes the new equilibrium with minimal residual error from the desired reference. Moreover, a satisfactory level of motion attenuation is achieved, as evidenced by the rotation angle ϕ and angular velocity $\dot{\phi}$ time series, exhibiting the characteristic linear decay indicative of a Coulomb friction dissipative force being present. The efficiency of the nonlinear magnetically-imposed damping becomes evident when compared with the linearly damped response of similar decay rate ($\theta = \theta_e$ and $K_{m_2} = c_d\dot{\phi}$ with $c_d = 0.4$ N mm s/°).

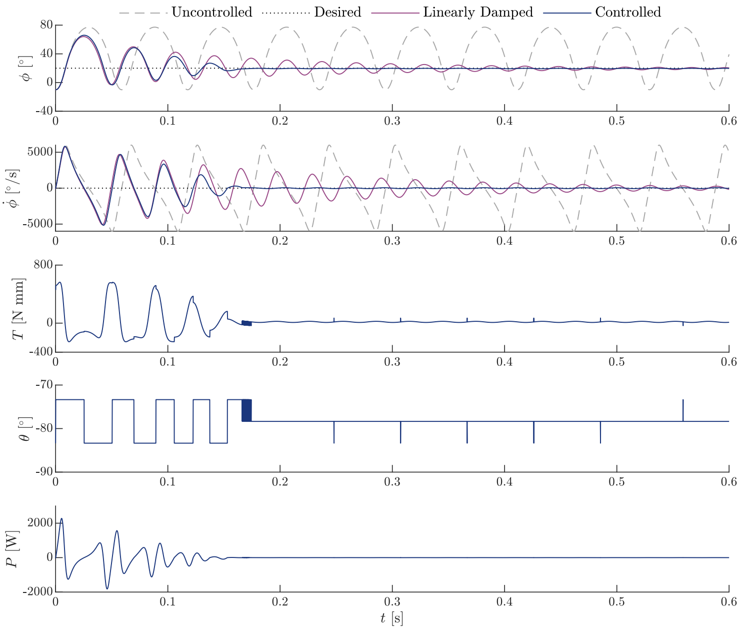

(a)

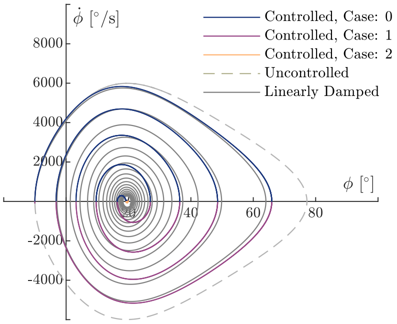

(b)

Figure 5.8: Active control system's response: (a) Times series of the rotation ϕ and the angular velocity $\dot{\phi}$ of the ring, the actuation torque T, the rotation θ, and the power of the magnetic interaction P, (b) Phase portrait of the system's response in the active control mode.

The power P plot in Figure 5.8a shows that energy is added and subtracted throughout the simulation, with the slight dominance of negative cycles within the power time signature validating the additional dissipation needed to eliminate the influence of the initial conditions. The nonlinear response of the SDOF system is also observed in the uncontrolled case, particularly in terms of the angular position ϕ, attributed to the interaction of the system with the static component of the EM field. When the electromagnet is activated in static mode (namely in the uncontrolled case: $M_f = M_{f_0}$, $K_{m_2} = 0$, and $\theta = \theta_e$), it establishes the new equilibrium of the system through a nonlinear adjustment of stiffness, leading to oscillations around ϕ_e.

The phase portrait of the actively controlled response of the system is presented in Figure 5.8b. The shape of trajectories is indicative of a dissipative system. It is evident that the damped oscillations of the system converge to the new stable equilibrium with the small error of $e \approx 0.8^\circ$. The nonlinear nature of the static field constantly exerted by the actuator is responsible for the distorted shape of the uncontrolled phase portrait closed loop, which would be circular in the absence of this magnetic interaction.

As anticipated, the control's performance depends highly on the properties of the two magnets and their separation distance. Therefore, an informed choice of $M_f M_c$ and d can improve the controlled response of the system. In Figure 5.9a, different magnet strengths M_f (or equivalently different ratios k_s/K_{m_1}) are demonstrated for the same distance, desired reference and initial conditions. Increasing the strength of the electromagnet reduces the duration of the transient response (the time interval between the initiation of the simulation and the convergence to the desired angle). Moreover, the steady-state error e from the desired angle of rotation ϕ_e is reduced by increasing M_f. It is noted that for $k_s/K_{m_1} > 2$ (Equation (5.17)), the response is primarily governed by the linear spring, with only a minor shift in the frequency and equilibrium position compared to the uncontrolled response, where only the linear spring is active.

Similar conclusions can be drawn when varying the separation distance d, while the strength and initial conditions are kept constant (Figure 5.9b). Decreasing the separation distance d results in a response with a steeper decay rate. However, due to the non proportional relation of the distance to the ratio k_s/K_{m_1}, it is imperative to consider upper and lower bounds for the separation distance according to transient behaviour and safety specifications. For instance, a separation distance $d = 20$ mm despite exhibiting the lowest steady-state error from the desired resting position, the response is dominated by the strong magnetic forces, resulting in large rotational angles during the transient response before the system eventually yields to the dissipative forces.

Equally important for the control efficiency is the size of the fluctuation step $\Delta\theta$ of the control variable θ. Figure 5.9c illustrates the controlled responses of the system for various adjustments of the external magnetic field orientation angle while maintaining the same dipole-to-dipole interaction strength. The effectiveness of the control (demonstrated by a good level of motion attenuation with a short transient) is directly proportional to $\Delta\theta$.

In Figure 5.9d, the controlled response of the system is depicted for both the presence ($k_s \neq 0$) and absence ($k_s = 0$) of the spring. Despite the restriction that arises from the analysis of the linearized equations (Equation (5.27)), the control algorithm effectively imposes the new desired equilibrium. It is important to note that although the control strategy is deduced and designed through the analysis of the linearized analytical equations, the numerical simulations consider the full nonlinear system. The nonlinearity of the system is crucial for the efficiency of the control, allowing it to be effective for higher ϕ_e and independent of the spring when the magnetic interaction is strong enough to impose the new equilibrium.

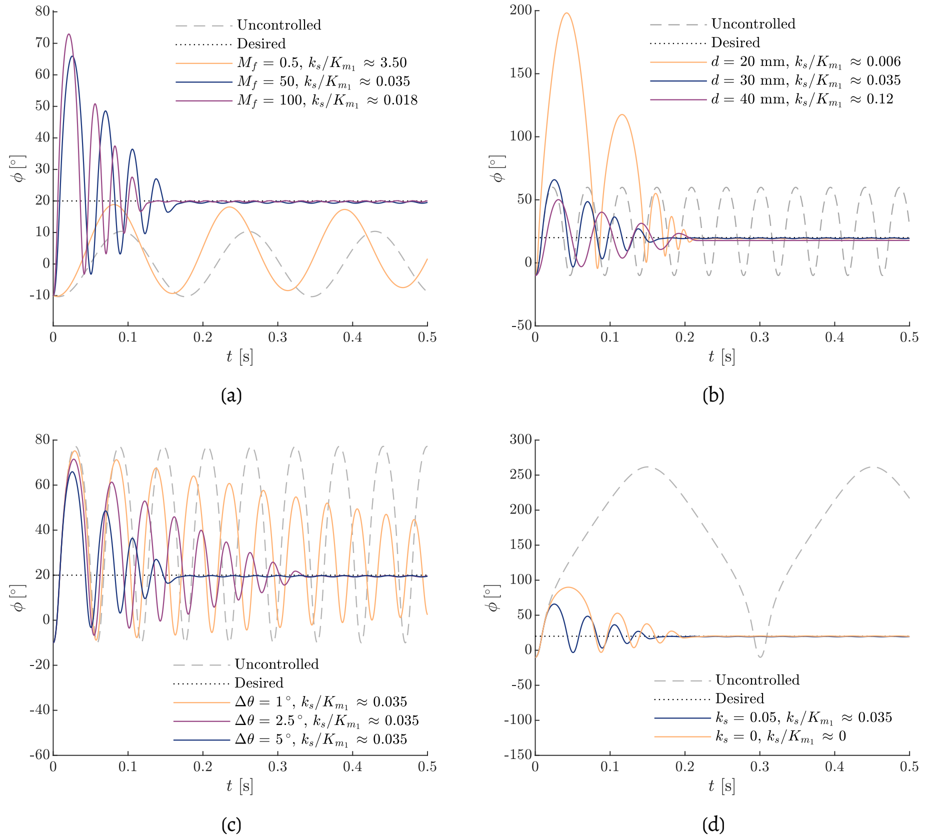

(a)

(b)

(c)

(d)

Figure 5.9: Comparison of the controlled response of the system for the same initial conditions and varied: (a) magnetic strength M_f with a constant $d = 30$ mm, (b) separation distances d with a constant $M_f = 50\,\mathrm{Am}^2$, (c) d with a constant $M_f = 50\,\mathrm{Am}^2$, and (d) spring stiffness k_s with a constant $M_f = 50\,\mathrm{Am}^2$.

5.6. Active torsional vibration control

Provided the successful imposition of a different equilibrium point than the intrinsic, an additional control mode can be explored to fully exploit the relationship between the external field orientation and stable equilibrium ϕ_e. This mode involves controlling rotation by selecting a desired trajectory for the cylinder's angular position ϕ. Such time-varied motion has practical applications in another critical stage of turbine installation: monopile installation.

Recently, an innovative vibratory installation technique for tubular piles is introduced, Gentle Driving of Piles (GDP). It is characterized by the simultaneous application of low-frequency axial vibrations and high-frequency torsional vibrations, designed to improve the installation efficiency while reducing underwater noise emissions [127]. In this method, axial pile penetration is achieved through vibrations applied at the pile head, utilising a novel pile-driving apparatus.

5.6.1. Analysis of the linearized EOM for a desired motion pattern

In this section, the ability of the controller to magnetically induce high-frequency torsional motion is examined. The desired motion is described by a harmonic oscillatory signal, which reads

$$\phi_e = A\sin(\omega t), \tag{5.29}$$

where A and ω represent the amplitude and frequency of the desired torsional vibration, respectively. The motion of the controlled system is given by Equation (5.20), as previously derived.

In order to achieve effective control, the response of the system during steady-state should be approximately equal to the desired trajectory, namely $\phi \approx \phi_e = A\sin(\omega t)$. Substituting this condition into the equation of motion yields

$$I_z\ddot{\phi}_e + (2K_{m_1} + k_s)\phi_e + K_{m_2} = 0, \tag{5.30}$$

with the coefficients K_{m_1} and K_{m_2} defined by Equations (5.14a) and (5.14b).

Similarly to the active rotation control scheme, the control rule for the orientation of the external magnetic field θ is formulated as

$$\theta = \theta_e + \Delta\theta\,\mathrm{sgn}(\dot{\phi}_e), \tag{5.31}$$

where θ_e is predicted by Equation (5.19) for the desired equilibrium angle ϕ_e and is given by

$$\theta_e = \frac{1}{B}\tanh\left(\frac{\phi_e}{A}\right). \tag{5.32}$$

Substituting Equation (5.32) and the coefficients K_{m_1} and K_{m_2} into the equation of motion (Equation (5.30)), an expression for the dipole strength product $M_f M_c$ is obtained:

$$M_f M_c = \frac{4\pi d^5}{\mu_0} \frac{A\sin(\omega t)\left(I_z\omega^2 - k_s\right)}{2R_1 A\sin(\omega t)\cos\left(-\frac{2AR_1}{R_2}\right) + R_2\sin\left(-\frac{2AR_1}{R_2}\right)}, \tag{5.33}$$

with $R_1 = 6R^2 + 6Rd + d^2$ and $R_2 = 3Rd + d^2$.

Assuming time moments $t = nT/2 = n\pi/\omega$ with $n \in \mathcal{Z}$, the maximum combined strength required to achieve the desired torsional vibration is obtained. Figure 5.10a plots $M_f M_c$ over a wide range of excitation frequencies and varying separation distances between the interacting magnets. The magnetic strength depends nonlinearly on d and f (where $f = \omega/2\pi$), with higher frequencies and larger distances requiring stronger magnetic fields to maintain effective control in the steady-state regime. Different conclusions arise when comparing the strength product $M_f M_c$ across frequencies for varying amplitudes of the desired torsional motion; higher amplitudes (A) require stronger dipole strengths for effective control. It should be noted that for the local minima observed, the desired vibration frequency f coincides with the natural frequency of the free and uncontrolled system f_n (Table 5.1).

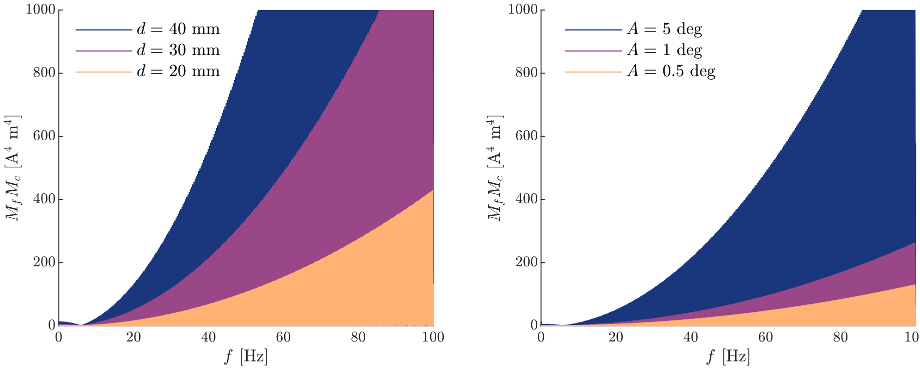

(a) (b)

Figure 5.10: Magnetic dipole strength for efficient torsional vibrations control for a range of excitation frequencies f with: (a) different distance between the magnets d and $A = 5°$, (b) different amplitudes of desired rotation A and $d = 30$ mm.

5.6.2. Active torsional vibration control results

The parameters of the controlled system studied in this section are listed in Table 5.4. The strength of the two interacting magnetic dipoles is deduced from Figure 5.10. The time series of the angular displacement of the rotating ring ϕ for different separation distances is shown in Figure 5.11a. The controller successfully imposes harmonic motion in terms of amplitude, phase, and frequency, compared to the system's free response. As expected, the controlled response consists of a brief transient followed by a steady-state component. The error and the duration of the transient depend on the distance d, with smaller distances yielding shorter transients and lower errors. Although the control is efficient for $d < 40\,\text{mm}$, optimizing the distance between the magnets can minimize power consumption P, as shorter distances generate higher interaction torques and power during the transient response. Similar insights are drawn from the analysis of translational control in the previous chapter.

Table 5.4: System parameters for the controlled vibrations mode.

$M_f M_c$ [A^{2}m^4]	d [mm]	A [°]	f [Hz]	ϕ_0 [°]	$\dot{\phi}_0$ [°/s]	$\Delta\theta$ [°]
500	[20, 30, 40]	5	50	-10	-100	5

The control performance is further demonstrated by the divergence of the controlled response ellipses from the desired motion pattern (dotted line) in the phase portrait in Figure 5.11b. The uncontrolled response of the system, in the absence of the magnetic interaction, is illustrated by the dashed line, whereas the controlled response is presented by the continuous lines. The best fit to the desired motion occurs at the shortest separation distance d. Furthermore, the performance of the controller for the different distances d confirms the prediction of Figure 5.10a for the selected magnetic dipole strength $M_f M_c = 500\,\text{A}^2\text{m}^4$.

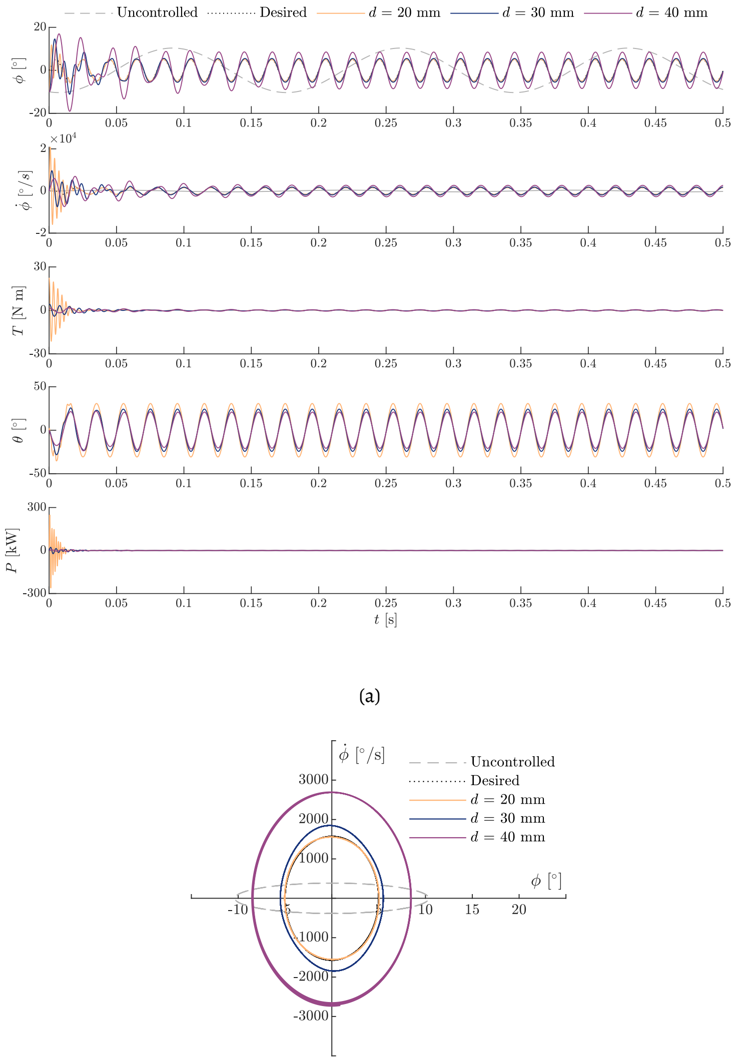

(a)

(b)

Figure 5.11: Torsional controlled vibrations system's response: (a) Times series of the rotation ϕ and the angular velocity $\dot{\phi}$ of the ring, the actuation torque T, the orientation θ, and the power of the magnetic interaction P, (b) Phase portrait of the system's response in the torsional vibration control mode.

5.7. Conclusions

This chapter has treated the development of a proof-of-concept contactless rotation control technique for cylindrical structures rotating around their longitudinal axis, with a specific focus on a potential application in offshore wind turbine installations.

The proposed controller exploits magnetic interaction between two magnets: one permanent magnet mounted on the structure and an electromagnetic actuator, with the control variable being the orientation of the magnetic dipole of the latter. By manipulating the magnetic field in this way, fundamental characteristics of the system, including the natural frequency and the stable equilibrium position, can be modified. Even though the control strategy is designed by analysing the linearized controlled system, it demonstrates efficiency in controlling the full nonlinear system solved using a numerical simulation method.

High controllability is exhibited in the control modes studied. The first control mode attenuates the rotational motion of the system by fluctuating the orientation of the external magnetic field, effectively generating a dissipative torque to the system. This energy dissipation is introduced through a magnetically-imposed term resembling Coulomb friction. The second control mode imposes a new stable equilibrium position to the system, combining attenuation with active control of the rotation. The third control mode expands on the active control imposing a time-variant desired torsional vibration to the cylinder. A small residual error from the reference and a swift transient response is reported in the active control results. The control performance depends on an informed selection of the separation distance, the fluctuation step of the dipole orientation and the ratio between the stiffness of the magnetic interaction and the linear spring.

Following the successful control of two critical vibrational modes, each addressed individually in the previous two chapters, it is now imperative to investigate their combined control design. This involves analysing the complexities and implications arising from the coupling of these two degrees of freedom within the dynamics of a suspended cylinder by a floating crane. This will be a matter of discussion in the upcoming chapter.

6

Magnetic control of coupled translational & torsional motions of suspended loads

Following the independent validation of the two most critical vibrational modes of a suspended load, the dynamics of simultaneous control are examined. These vibrational modes, translational and torsional, dominate the dynamical response of the payload during the floating offshore turbine deployment and significantly impact the assembly accuracy.

To investigate this, the lab-scale pendulum analogue (discussed in Chapter 4) is augmented with a cylindrical mass that is free to rotate around its shaft (longitudinal axis), in a similar manner as the system studied in the previous chapter. The new configuration is analysed through numerical simulations, exploring the controllability of a two-degree-of-freedom dynamical system. The design approach for controlling translational and torsional motion adheres to the methodologies detailed in previous chapters.

This chapter first introduces the dynamical system, emphasizing the magnetic coupling, then presents the control design with a focus on stability requirements. Finally, the controlled response of the system is demonstrated for selected initial conditions and external disturbances. Special attention is given to the efficiency of the combined control and its impact on the system's dynamical behaviour, including the nonlinear coupling effects from magnetic interactions.

Part of this chapter has been published in:
P. Atzampou, P. C. Meijers, A. Tsouvalas, and A. V. Metrikine, "Motion control of suspended loads via magnetic interaction," in *Nonlinear Systems - Practical Applications and Contemporary Challenges*, (soon to be published), IntechOpen, 2025

6.1. Governing equations of a controlled planar torsional magnetic pendulum

The fundamentals of the concurrent control are studied using an elementary coupled model, as illustrated in Figure 6.1. The dimensions and properties of the system are given by Table 5.1 (Chapter 5), for a pendulum arm of $\ell = 1\,\mathrm{m}$. In principal, the set-up integrates the two SDOF systems reported in previous chapters. The control design requires the action of two separate electromagnetic actuators: one controlling the rotation of the mass in *xz*-plane (translation) and the other in *xy*-plane (torsional rotation). In the real practical application, the suspended mass is an elongated cylindrical structure (e.g., an OWT monopile foundation). Such geometry allows for an advantageous placement of contactless control points on different heights along its length on one side of the load, ideally on the floating vessel's deck. For simplicity, in this preliminary study of the combined control, two permanent magnets are attached to opposite sides of the cylindrical mass, represented by magnetic dipoles.

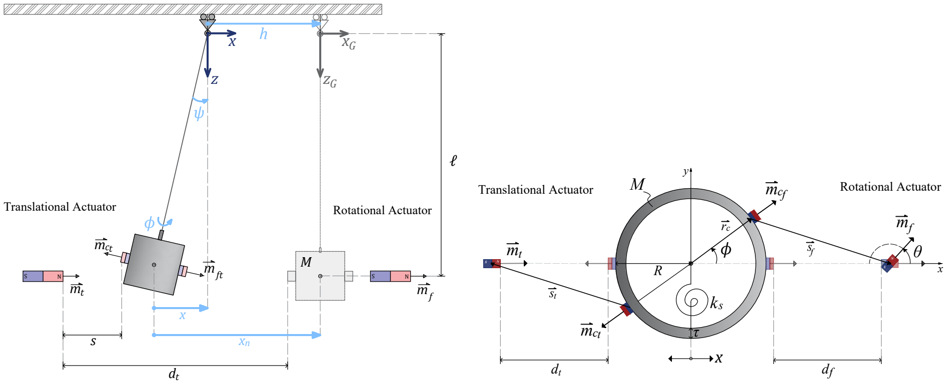

(a) *xz*-plane (b) *xy*-plane

Figure 6.1: Schematic of the pendulum set-up for the combined control of its translational and torsional degree of freedom.

The placement of the dipoles, depicted in Figure 6.1, may be favourable for the visual representation of the point mass problem. However, this arrangement infers potential interactions between the magnetic fields of the mounted dipoles or direct interference from one actuator affecting the field of the other as experienced by the targeted fixed magnet. Nevertheless, these effects are neglected in the current analysis, as such interactions would not occur in practical applications, due to adequate separation distance between the control points and respective actuators (along the structure's *z*-axis).

The first step in deriving the equations of motion for the dynamical system involves analytically expressing the position of the suspended mass concerning the three spatial coordinates. The position vector of the mass ($\vec{P}_G$) with respect to the global reference system is given by

$$\vec{P}_G = \vec{P} + \vec{h} = \begin{bmatrix} \ell \sin(\psi) \\ 0 \\ \ell \cos(\psi) \end{bmatrix} + \begin{bmatrix} h \\ 0 \\ 0 \end{bmatrix}, \tag{6.1}$$

where $\vec{P}$ represents the coordinates of the centre of gravity (COG) of the cylindrical load in the local reference system xyz. Note that the suspended load is adequately small to be considered a point mass in the derivations. The motion of the pivot is described by $h = A_h \sin(\Omega t)$.

The coordinates of the magnets mounted on the mass are denoted as $\vec{P}_{ct}$ and $\vec{P}_{cf}$ for the translational and the torsional control, respectively, and are expressed as

$$\vec{P}_{ct} = \vec{P}_G - \begin{bmatrix} R\cos(\phi) \\ R\sin(\phi) \\ 0 \end{bmatrix} \text{ and } \vec{P}_{cf} = \vec{P}_G + \begin{bmatrix} R\cos(\phi) \\ R\sin(\phi) \\ 0 \end{bmatrix}. \tag{6.2}$$

Two electromagnetic actuators are placed at a fixed distance on either side of the load, d_t for the translational and d_f for the torsional controller. The position vectors of the actuators $\vec{P}_t$ and $\vec{P}_f$ are

$$\vec{P}_t = \begin{bmatrix} -R - d_t \\ 0 \\ \ell \end{bmatrix} \text{ and } \vec{P}_f = \begin{bmatrix} R + d_f \\ 0 \\ \ell \end{bmatrix}, \tag{6.3}$$

while they describe the coordinates of the translational and torsional actuators, respectively.

The kinetic ($\mathcal{K}$) and potential ($\mathcal{U}$) energy of the dynamical system are given by

$$\mathcal{K} = \frac{1}{2} M ||\vec{P}_G||^2 + \frac{1}{2} I_z \dot{\phi}^2, \tag{6.4a}$$

$$\mathcal{U} = W_m + Mg\left(\ell - \vec{k} \cdot \vec{P}_G\right) + \frac{1}{2} k_s \phi^2, \tag{6.4b}$$

with the $\vec{k}$ representing the unit vector in the vertical direction (z-axis), I_z the moment of inertia of the mass around the z-axis, and k_s being analogous to the stiffness provided by the suspension cable and experienced by the mass rotating in this direction.

In Equation (6.4b), W_m is the contribution of the pairs of interacting magnetic dipoles to the potential energy of the system $\mathcal{U}$ and is equal to

$$W_m = -\sum \vec{m}_{cn} \cdot \vec{B}_n, \tag{6.5}$$

in which $\vec{B}_n$ is the magnetic field exerted by the EM ($\vec{m}_n$) to the location of the respective PM on the cylindrical point mass ($\vec{m}_{cn}$), where the general subscript notation n is either t

for the translational or f for the torsional control. The magnetic field vector $\vec{B}_n$ reads

$$\vec{B}_n = -\frac{\mu_0}{4\pi}\vec{\nabla}\frac{\vec{m}_n \cdot \vec{s}_n}{s_n^3}. \tag{6.6}$$

The vector representing the separation distance between the two dipoles is denoted as $\vec{s}_n$ (Figure 6.1b). The magnitude of s_n is calculated by the following norm:

$$s_n = \|\vec{P}_n - \vec{P}_{cn}\|. \tag{6.7}$$

Referring to Figure 6.1b, the vectors representing the four magnetic dipole moments are given by

$$\vec{m}_t = M_t \begin{bmatrix} 1 \\ 0 \\ 0 \end{bmatrix} \text{ and } \vec{m}_{ct} = -M_{ct} \begin{bmatrix} \cos(\phi) \\ \sin(\phi) \\ 0 \end{bmatrix} \text{ for the translational control, and} \tag{6.8}$$

$$\vec{m}_f = M_f \begin{bmatrix} \cos(\theta) \\ \sin(\theta) \\ 0 \end{bmatrix} \text{ and } \vec{m}_{cf} = M_{cf} \begin{bmatrix} \cos(\phi) \\ \sin(\phi) \\ 0 \end{bmatrix} \text{ for the torsional control,} \tag{6.9}$$

where θ is the orientation angle of the torsional actuator's magnetic field.

Similarly to Equation (5.10a), the magnetic potential energy W_m, once evaluated, results in a nonlinear trigonometric expression. In order to analyse the dynamics of the coupling, the trigonometric terms of ϕ and ψ are replaced by their corresponding Taylor series expansions up to the second order around the equilibrium points $\phi = \psi = 0°$. The contribution from the magnetic interaction can then be concisely rewritten as:

$$W_m = -K_{m_1}\psi + K_{m_2}\phi + K_{m_3}\psi^2 + K_{m_4}\phi^2 + K_{m_5}\psi\phi + C, \tag{6.10}$$

with the coefficients:

$$K_{m_1} = 3\ell\left(\frac{M_{ct}M_t\mu_0}{2\pi(d_t+h)^4} + \frac{M_{cf}M_f\mu_0}{2\pi(d_f-h)^4}\cos(\theta)\right) \tag{6.11a}$$

$$K_{m_2} = \frac{M_{cf}M_f\mu_0}{4\pi(d_f-h)^4}(3R+d_f-h)\sin(\theta) \tag{6.11b}$$

$$K_{m_3} = 3\ell^2\left(\frac{M_{ct}M_t\mu_0}{\pi(d_t+h)^5} - \frac{M_{cf}M_f\mu_0}{\pi(d_f-h)^5}\cos(\theta)\right) \tag{6.11c}$$

$$K_{m_4} = \frac{M_{cf}M_f\mu_0}{4\pi(d_f-h)^5}\left((d_f-h)^2 + 6R^2 + 6Rd_f - 6Rh\right)\cos(\theta) - \frac{M_{ct}M_t\mu_0}{4\pi(d_t+h)^4}(3R+d_t+h) \tag{6.11d}$$

$$K_{m_5} = 3\ell\left(\frac{M_{cf}M_f\mu_0}{4\pi(d_f-h)^5}(4R+d_f-h)\sin(\theta)\right) \tag{6.11e}$$

$$C = -\frac{M_{cf} M_f \mu_0}{2\pi(d_f - h)^3}\cos(\theta) + \frac{M_{ct} M_t \mu_0}{2\pi(d_t + h)^3}. \tag{6.11f}$$

The Lagrangian ($\mathcal{L}$) of the system is formulated as

$$\frac{\mathrm{d}}{\mathrm{d}t}\left(\frac{\partial \mathcal{L}}{\partial \dot{\vec{q}}}\right) - \frac{\partial \mathcal{L}}{\partial \vec{q}} = 0 \text{ with } \mathcal{L} = \mathcal{K} - \mathcal{U} \text{ and } \vec{q} = \left[\psi, \phi\right]^{\mathrm{T}}, \tag{6.12}$$

in which $\vec{q}$ describes the vector of the two unknown states of the system. Evaluating Equation (6.12) using the expression from Equation (6.10), yields the following equations of motion:

$$M\ell^2\ddot{\psi} + Mg\ell\psi = -M\ddot{h}\ell + T_t \tag{6.13a}$$

$$I_z\ddot{\phi} + k_s\phi = T_f, \tag{6.13b}$$

where the external magnetic torques are equal to

$$T_t = -\frac{\partial W_m}{\partial \psi} = +K_{m_1} - 2K_{m_3}\psi - K_{m_5}\phi \tag{6.14a}$$

$$T_f = -\frac{\partial W_m}{\partial \phi} = -K_{m_2} - 2K_{m_4}\phi - K_{m_5}\psi. \tag{6.14b}$$

The magnetic interaction couples the two degrees of freedom ψ and ϕ, through the coupling term K_{m_5} in the magnetic potential energy contribution (Equation (6.10)). Specifically, the external torques introduce magnetically induced stiffness-like terms, which interconnect the equations of motion through the stiffness matrix. Consequently, Equation (6.13) can be reformulated into matrix form to emphasize the contributions induced by the magnetic interaction as follows:

$$\mathbf{M}\ddot{\vec{q}} + \mathbf{K}\vec{q} = \vec{T}, \tag{6.15a}$$

$$\begin{bmatrix} M\ell^2 & 0 \\ 0 & I_z \end{bmatrix}\begin{bmatrix} \ddot{\psi} \\ \ddot{\phi} \end{bmatrix} + \begin{bmatrix} Mg\ell + 2K_{m_3} & K_{m_5} \\ K_{m_5} & k_s + 2K_{m_4} \end{bmatrix}\begin{bmatrix} \psi \\ \phi \end{bmatrix} = -\begin{bmatrix} M\ell\ddot{h} - K_{m_1} \\ K_{m_2} \end{bmatrix}, \tag{6.15b}$$

in which the bold characters **M** and **K** denote the mass and stiffness matrices, respectively. The coupling present in the off-diagonal elements of the stiffness matrix is attributed exclusively to torsion, as K_{m_5} contains important parameters of the torsional control.

6.2. Control strategy

Following the control schemes introduced in Chapter 4 and Chapter 5 which addressed the two DOFs individually, translational vibrations are controlled by adjusting the strength and polarity of the dipole M_t, while the orientation of the magnetic field of M_f is employed to control the torsional rotation of the point-mass cylinder. In Equation (6.15b), the terms

K_{m_1} and K_{m_2} serve as the controlled external forces acting on the system. The magnetic strength of the translational controller is governed by a PD control equation, expressed as

$$M_t = K_p\, e + K_d\, \dot{e}, \text{ with } e = \xi - \ell\psi - h, \tag{6.16}$$

where the PD gains are constant values with $K_p, K_d > 0$ and ξ represents the desired translational motion. The control rule for the torsional mode is defined by

$$\theta = \theta_e + \Delta\theta \tanh\left(\beta\dot{\phi}\right), \text{ with } \Delta\theta = \text{const.}, \tag{6.17}$$

where θ_e is the orientation angle that corresponds to the desired new equilibrium ϕ_e, and $\Delta\theta$ is the chosen fluctuation step for the total orientation θ. Moreover, the parameter β controls the steepness of the transition between the values around zero. As β approaches infinity, the control function converges to the standard sgn(..) function, while still providing a smooth and differentiable approximation.

6.3. Stability requirements

While the signs of the dipoles of the torsional control and the mounted dipole M_{ct} are known and taken into account in the derivations, M_t is subject to an alternating polarity dictated by the error (e) and the error's rate of change ($\dot{e}$). Moreover, the strength is a controlled variable and, as numerically described in Equation (6.16), introduces additional stiffness (through the $K_p\psi$) and damping ($K_d\dot{\psi}$) terms to the system. Therefore, it is difficult to deduce one concise rule for the stability of the system in terms of stiffness due to the presence of time-varying functions in the stiffness coefficient in Equation (6.15b).

To ensure a stable response, a condition concerning the magnetic strength of the translational actuator must be satisfied. This condition directly affects the stability of the controlled dynamical system. Instability is undesirable as it results in an increasing amplitude of the response, which, within the proposed control scheme, can reduce the separation distance between the magnets. Such a reduction could potentially lead to the "failure" of the control, as one of the pairs of magnetic dipoles may yield to the attracting forces and stick to each other.

To assess the stability of the system, the natural frequencies ω_n need to be calculated. These frequencies are determined by solving the eigenvalue problem [129]. The characteristic equation is given as

$$\det\left(\mathbf{K} - \omega_n^2\mathbf{M}\right) = 0, \tag{6.18}$$

in which **K** and **M** are the stiffness and mass matrices as defined in Equation (6.15b). Non-trivial, real, and positive roots of ω_n^2 correspond to the squared natural frequencies of a stable system. However, if at least one ω_n has a positive imaginary part, or equivalently if $\omega_n^2 < 0$, the system falls within the unstable regime. For reference, the natural frequencies of the uncontrolled system, derived from the modal analysis, are equal to: $\omega_n = [3.13,\ 26.38]$ rad/s, which correspond approximately to $f_n \approx [0.50,\ 4.20]$ Hz.

For equal separation distances $d_t = d_f$, a desired stable equilibrium $\phi_e = 0^\circ$, and equal magnetic dipole strengths $M_f = M_{cf} = M_{ct}$, the natural frequencies ω_n^2 are plotted against different magnetic strength ratios M_t/M_f in Figure 6.2. Since the desired equilibrium position for the rotation around the z-axis aligns with the intrinsic equilibrium of the system, the corresponding orientation becomes $\theta_e = 0^\circ$. Furthermore, the fluctuation angle $\Delta\theta$ is an *a priori* selected small angle (as per the control rule presented in Equation (6.17)). Thus, it is reasonable to assume $\cos(\theta) \approx 1$ and $\sin(\theta) \approx \theta$. Now, the only time-varying variable of the system is the pivot point motion. Therefore, it is important to examine the changes in the natural frequencies derived for three distinct values of h. For $h = 0$, the system remains stable for $M_t/M_f \leq -1$ (Figure 6.2a). However, the stability range broadens when the pivot moves away from the torsional actuator (Figure 6.2c). Conversely, when the distance between the two translational dipoles increases ($h > 0$, Figure 6.2b), the range shifts toward lower ratios. In order to compensate for the attractive forces of the torsional dipoles and the additional leverage of a smaller d_f, the translational actuator must increase its (absolute) strength by over threefold to maintain a stable response.

The common denominator in the Figure 6.2 is the fact the ratio remains negative across all three amplitudes of suspension motion h. This is a logical condition for the stability of the system, since when M_t is positive, the dipoles have opposite polarities, resulting in repulsion. This configuration represents a potentially unstable state for the pendulum, creating an unstable equilibrium for $\phi = 0^\circ$ as shown in Figure 6.3a. In contrast, when the controller's dipole strength is negative, the dipoles align to produce attractive forces on both sides. This configuration creates a stable state, characterized by a single global potential well (Figure 6.3b).

Inspecting K_{m_1} as given by Equation (6.11a), two distinct torque actions are observed: one direct, exerted by the translational controller, and another indirect, generated by the horizontal components of the attractive force between the magnetic dipoles of the torsional controller. For an effective controlled response, the translational controller should counteract the additional torque (around the pivot point) induced by the torsional control. It is important to note that the translational control torque does not directly influence the motion in the xy-plane, except for the excitation amplitude at the pivot, as outlined in Equation (6.11b).

Therefore, it is suspected that the time trace of M_t will have a non-zero average value, let it be M_{t_0}, around which the translational control variable will fluctuate with respect to the error and suspension motion. The amplitude of M_{t_0} arises from the main prerequisite for the stability of the system, neutralising the torque generated by M_f in Equation (6.11a) , which yields

$$K_{m_1} = 0 \rightarrow \frac{M_{t_0}}{M_f} = -\cos(\theta)\frac{(d_t + h)^4}{(d_f - h)^4}. \tag{6.19}$$

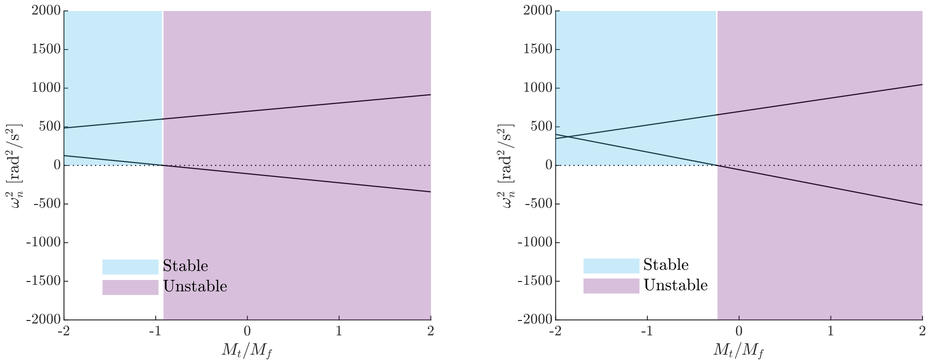

(a) For $h = 0$

(b) For $h < 0$

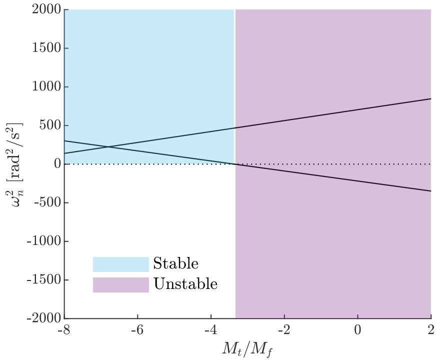

(c) For $h > 0$

Figure 6.2: Equilibrium stability indicators for various relative strength ratios M_t/M_f and different pivot point motion amplitudes h.

6.4. Controllability range

To ensure the efficiency of the torsional control and update the prediction formula for the torsional control scheme, the equilibrium position ϕ_e is derived with relation to the external dipole orientation θ and reads

$$\frac{\partial W_m}{\partial \phi} = 0 \rightarrow \phi_e = -\frac{K_{m_5}\psi_d + K_{m_2}}{k_s + 2K_{m_4}}. \tag{6.20}$$

The equilibrium position of the rotating mass is now a function of various time-varying parameters of the system, namely $\phi_e \rightarrow f(\psi_d, h, \theta_e)$, where ψ_d is the desired angular displacement of the suspended mass. Thus, deriving a closed-form equation to *a priori* predict the suitable external orientation of the field of the torsional controller is no longer possible. This calculation is incorporated into the numerical solver, resulting in a time-varying $\theta_e(t)$.

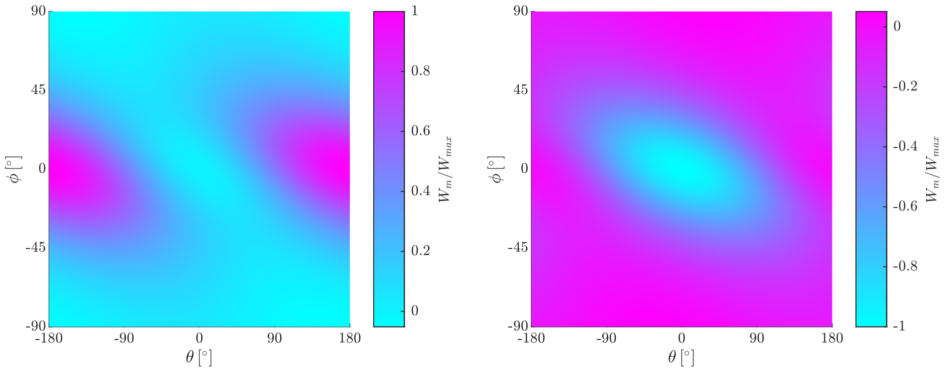

(a) Repulsion: $M_t M_{ct} < 0$

(b) Attraction: $M_t M_{ct} > 0$

Figure 6.3: Normalized magnetic potential over its maximum value W_m/W_{max} against ϕ for various angles θ and $\psi = h = 0$. The magnetic dipoles are equal to $M_f = -M_{ct} = M_{cf} > 0$, with initial separation distances set as $d_t = d_f$.

However, the relation of the desired equilibrium position ϕ_e to the external field orientation θ_e defines the controllability range of the torsional rotational control. In order to estimate the expected range, certain assumptions can be set. First, the translational controller is successful in attenuating the motion of the pivot point, maintaining the position of the suspended mass at $\psi = \psi_d = 0\,^\circ$ in xz-plane with regard to the global reference system. Second, the strength of the translational actuator, even though a function of time, is chosen to have a fixed value, namely to equate to $M_t = M_{t_0}$ as derived in Equation (6.19). The equilibrium position is governed by the magnetic interaction when:

$$k_s/K_{m_4} \ll 2. \tag{6.21}$$

Figure 6.4a maps the potential energy wells $W_m(\phi)$ for various orientations of the external torsional actuator's static magnetic field θ, calculated by numerically solving the fully nonlinear expression for W_m. The deepest points of these wells are marked by the white dotted line, indicating that the relation between the desired new equilibrium ϕ_e and the angle θ_e is formed. This line corresponds to the case where the pivot point excitation h is set to zero.

The function given by Equation (5.19) can be fitted to these equilibrium points as plotted in Figure 6.4b, defining a controllability range of $-20^\circ < \phi_e < 20^\circ$. However, when the pivot point excitation varies over time, such as with a harmonic motion $h = A_h \sin(\Omega t)$, the prediction curve shifts as the amplitude A_h changes. Figure 6.4b displays the two extreme values of the pivot point motion. When the suspension point moves closer to the torsional actuator, controllability increases slightly. Conversely, when the pivot moves further away, controllability decreases. Notably, the inclination of the curve for these boundary cases does not change proportionally, reflecting the nonlinear nature of magnetic interactions with distance.

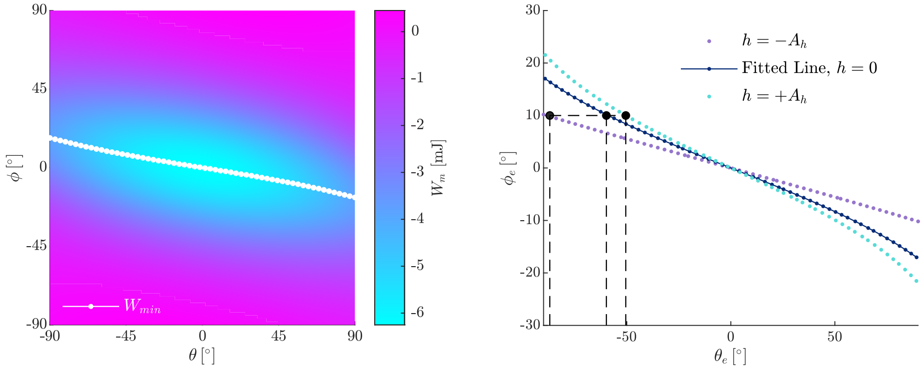

(a) (b)

Figure 6.4: Estimation of the equilibrium ϕ_e in presence of a static magnetic field for different orientations θ. The magnetic dipoles are equal to $M_f = -M_{ct} = M_{cf} > 0$, assuming $M_t = -M_f$, with initial separation distances set as $d_t = d_f$.

Another condition that might interfere with both stability and controllability pertains to saturation limits of the actuators, which were of importance in translational control presented in Chapter 4, but have not been considered in this chapter for simplicity.

6.5. Controlled response of a magnetic pendulum to translational and torsional vibrations

This section examines two distinct cases of controlled vibrations:

1. *Disturbance rejection*: Attenuation of the dynamic response of the pendulum translational and torsional motions while subjected to an external excitation of its pivot and non-trivial initial conditions;
2. *Desired translational motion & torsional motion attenuation*: Imposition of a desired motion pattern to the suspended mass M in xz-plane and attenuation of torsional vibrations in xy-plane.

6.5.1. Disturbance rejection of translational & torsional vibrations

The first control mode to be studied pertains to the motion attenuation of the translational and torsional vibrations. The desired position of the suspended load is chosen to be $\psi = \phi = 0°$. The parameters of the controlled system are presented in Table 6.1.

An adaptive, variable-order solver for ordinary differential equations (ODEs), MATLAB's built-in solver *ode113* is employed to handle the given coupled system. Unlike solvers

Table 6.1: System parameters for the combined controlled vibrations.

$M_f M_{c_f}$ [A^{2}m^4]	M_{c_t} [Am^2]	d_f [mm]	d_t [mm]	A_h [mm]	f_h [Hz]	ϕ_0 [°]	$\dot{\phi}_0$ [°/s]
5	-1	40	40	5	0.6	20	0

specifically designed for stiff equations, this solver relies on a combination of Adams-Bashforth-Moulton and variable-order methods, allowing it to efficiently manage both non-stiff and mildly stiff dynamics by adjusting step size and order automatically [130]. Due to the complex coupling in the system and varying time scales across the degrees of freedom, *ode113* provides a balance of stability and accuracy without requiring a fully stiff solver.

For the translational control, the PD controller gains are determined heuristically to minimize error and enhance the response of the controller. Thus, in this exemplary case, the proportional gain is set as $K_p = 3 \times 10^4$ A m and the derivative gain as $K_d = 30$ A m s. Note that the gain values differ from those used in Chapter 4, as the standard PD control is employed here, with the control input being the dipole strength rather than the electromagnet voltage. While the modified PD controller could also be applied, its effect can be equivalently achieved by using higher gain values to enhance the controller's sensitivity to deviations from the desired set-point [96].

Provided that the desired equilibrium of the torsional motion coincides with the intrinsic equilibrium of the system, the control rule given in Equation (6.17) becomes

$$\theta = \Delta\theta \tanh(\beta\dot{\phi}), \tag{6.22}$$

with the steepness coefficient $\beta = 1$ and the orientation alteration step $\Delta\theta = 5^\circ$. Both controllers are activated at $t_s = 2$ s from the start of the simulation. This delay may lead to a more intricate transient response, aligning with the real application where vibrations would be present before the controllers are activated.

Figure 6.5 displays the controlled (solid line), desired (dotted line) and uncontrolled response of the system (dashed line). More specifically, Figure 6.5a demonstrates the effectiveness of the PD translational controller, achieving minimal steady-state error and a quick, smooth transient response, as indicated by the displacement and velocity time series. To minimize the residual steady-state error, the integral gain of the PID controller can be introduced, effectively addressing the accumulated discrepancy from the desired position. Notably, the control variable M_t, upon a successful translational control settles at $M_t = -M_{t_0} = -M_f$, as predicted by Equation (6.19).

The controlled response of the torsional degree of freedom is depicted in Figure 6.5b. In this case, the attenuation of motion is more gradual than in the translational response, displaying a damping mechanism similar to Coulomb friction, which is evident by the linear decay of the oscillations. To reduce the duration of the decay, a stronger electromagnet

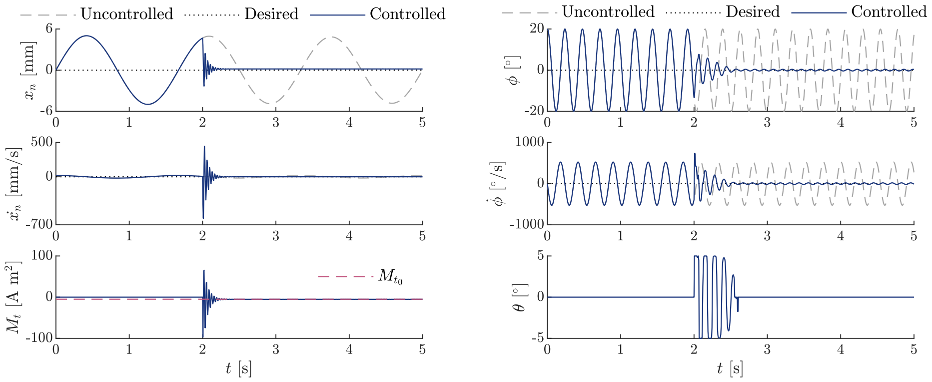

(a) Controlled response for translational vibrations

(b) Controlled response for torsional vibrations

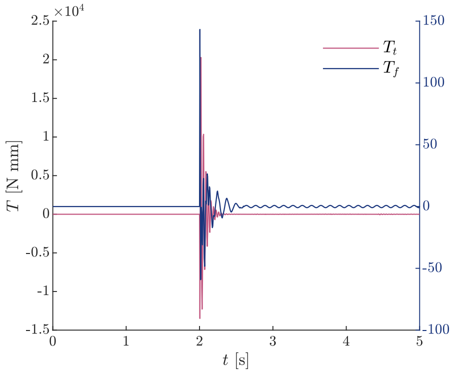

(c) Effective actuation torque T for torsional and translational control

Figure 6.5: Combined control efficiency metrics for motion attenuation.

M_f should be used. Alternatively, the closer proximity of the two interacting dipoles could yield similar favourable results as explored in Figure 5.8.

On a general note, the different frequencies of the oscillation observed in the steady-state responses of the two degrees of freedom reflect the natural frequencies of the free, uncontrolled system.

In Figure 6.5c, the two control torques exerted on the load are presented. The torque time series resembles the shape of the translational displacement and torsional angle time series. The highest amplitudes are observed for the translational torque T_t, which exhibits higher variation in the steady-state. Interestingly, the range of the translational torque is two orders of magnitude greater than that of the torsional torque, highlighting the differing control demands across the two degrees of freedom.

6.5.2. Desired motion for the translational & motion attenuation for the torsional vibrations

In this control mode, the system properties, initial conditions, and external excitation parameters remain consistent with those outlined in Table 6.1. The distinction lies in the translational vibration's control set point, now defined as a harmonic oscillation: $\xi = A \sin(\omega t)$, where the amplitude $A = 5$ mm and the frequency $f = 0.3$ Hz $< f_n$. This low-frequency oscillation aligns with the anticipated vessel movement induced by wave action relative to the fixed installation position of the offshore wind turbine.

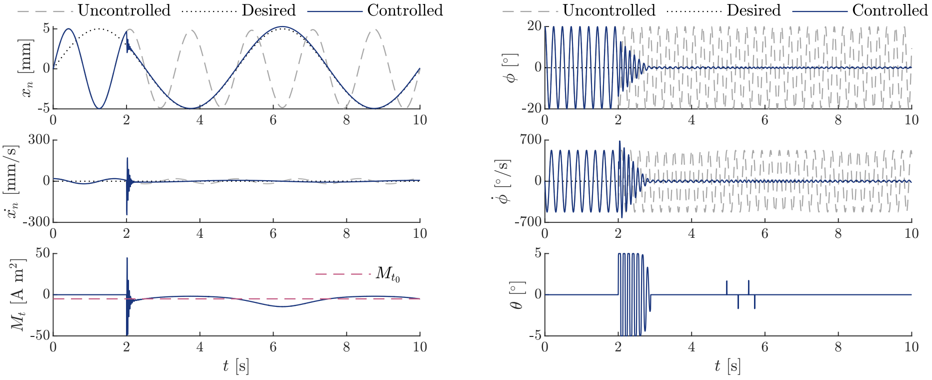

(a) Control response for translational vibrations

(b) Control response for torsional vibrations

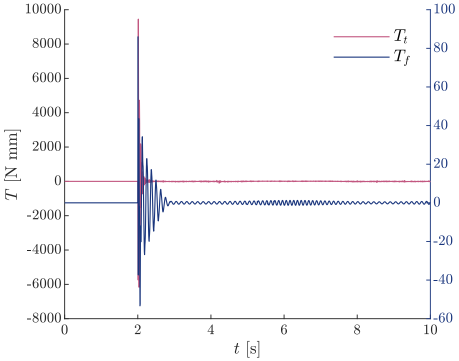

(c) Effective actuation torque T for torsional and translational control.

Figure 6.6: Combined control efficiency metrics for torsional damping and desired translational motion.

Figure 6.6 stimulate similar observations with the disturbance rejection combined control result of the previous section. Here, however, the translational controller succeeds in imposing a time-varying function to the displacement of the suspended load, as shown in Figure 6.6a. Furthermore, a distinct, sharp peak in T_t is observed in the effective actuation torque time series, representing an instantaneous adjustment in phase and frequency due to the controller's activation. The control objective of the translational actuator is to sustain a specific oscillatory motion, requiring a consistent torque amplitude throughout the simulation to achieve the desired displacement profile.

The performance of the torsional actuator is not negatively affected by the imposed oscillations of the load in *xz*-plane. On the contrary, the dissipation of the rotation is nearly twice as effective compared to the disturbance rejection mode. This observation suggests that as long as the translational control effectively manages the load position—and consequently the separation distance of the two torsional dipoles—the torsional control maintains its efficiency. This coupling ensures that both controllers contribute positively to the system's controllability.

6.6. Conclusions

In the present chapter, the combined control of two key degrees of freedom—translation and torsion—is analysed, building on the separate control strategies detailed in previous sections. The coupling presented due to the simultaneous action of the two actuators is reflected in the additional non-diagonal terms in the stiffness matrix of the system. The equilibrium position depends not only on the magnetic interaction but also on the excitation and the angular position of the pendulum in *xz*-plane. Moreover, the mean amplitude of the translational control is dictated by the chosen amplitude of the torsional actuator dipole, necessary to counteract the attraction forces exerted by the torsional dipole arrangement on the suspended load.

Using the previously established control schemes, the controllability and efficiency of the combined control approach are evaluated under two modes: disturbance rejection for both translational and torsional motions, and desired motion for translational control coupled with damping control for torsional motion. In both scenarios, the controllers perform effectively, significantly reducing vibrations, with the translational response showing a rapid transition to the target steady state. The success of the combined control lies primarily in the precise motion control applied by the translational actuator, which determines the separation distance of the torsional dipoles—a critical factor in achieving efficient torsional control.

The controllability range of the torsional vibrations in the combined control is both time-dependent and narrower compared to the case where the torsional actuator operates independently. Aligning the torsional actuator with the system's natural rotational equilibrium simplifies the control, making the optimal static orientation of the controller's magnetic field zero, regardless of external excitation or the other degree of freedom. The performance of the torsional controller can be further optimised by modifying the separation distance, magnetic strength, and orientation step of the external magnetic dipole.

Furthermore, the stability of the system under combined control relies on maintaining the separation distances between the mounted magnets and their respective controllers within a safe and allowable range to prevent the magnets from clashing. Additionally, the operational limits of the actuators, which have not been addressed in this chapter, may also impact both stability and controllability.

The subsequent chapter is devoted to presenting the planar oscillations of the combined control of a hanging distributed mass on full-scale, utilising the insights and mechanisms explored thus far.

7

Contactless magnetic control of a suspended monopile during installation

Subsequent to the successful implementation of position and rotation control of a point-mass pendulum, the dynamical system under consideration in this chapter reflects a more realistic installation configuration. This upgraded set-up features a suspended distributed cylindrical mass, providing a more accurate representation of the hanging OWT component, and introducing additional vibration modes.

A control strategy is devised for the full-scale setup, incorporating the methodologies established in previous chapters. The design incorporates an exemplary actuator arrangement tailored to meet the controllability requirements and achieve efficient control during the free suspension phase of the installation process. The scenario studied here serves as a practical exploration of the design while allowing for a direct comparison of the overall efficiency with traditional tugger line position control systems. Additionally, a detailed evaluation of the forces and strengths required by the individual magnet pairs is conducted, offering valuable insights into the feasibility and effectiveness of the contactless installation in operational conditions.

This chapter begins by presenting the full-scale data gathered during an offshore campaign, aiming at identifying the dominant environmental loads and the order of magnitude of the suspended tower's motion during installation. A full-scale simulated dynamic system of the tower installation is presented, accompanied by modal analysis results detailing mode shapes and natural frequencies. To ensure the controllability of the system, an exemplary efficient actuator arrangement is selected. Various control modes are evaluated to examine the performance of contactless control amidst the increased complexity arising from additional degrees of freedom. The advancements achieved through the contactless control design are emphasized, demonstrating its potential to enhance the efficiency and effectiveness of complex offshore installation processes.

7.1. Floating OWT installations

Floating installations of offshore wind turbines are particularly susceptible to environmental loads from wind and waves, which can significantly affect operations. Notably, wave loads induce pronounced motion at the crane tip during installation activities [131], with dynamic positioning systems only mitigating horizontal vessel movements, leaving roll motion largely unaddressed [29, 132]. These motions can introduce challenges to installation precision and efficiency.

The vessel's rigid-body dynamics primarily dictate the crane tip motion on floating vessels, whereas elastic deformation of the crane plays a relatively minor role compared to jack-up vessels, as concluded by de Kruif and Rossin (2021). The influence of the crane on the vessel's motion is minimal; however, as payload weights increase substantially, the interaction between crane-load and vessel dynamics transitions to a two-way relationship, potentially requiring additional stability checks during control system design [133].

One effective approach to mitigate undesired payload oscillations is to employ weather orientation for floating vessels, which improves feasibility and reduces operational costs [29]. Nonetheless, persistent vessel-induced disturbances pose further challenges for crane operations. These disturbances, acting on the crane-payload subsystem—a classic underactuated system with insufficient independent controls for its degrees of freedom—can exacerbate payload pendulation, increasing the risk of collisions and operational failures [134].

Critical phases during OWT installations are the lifting, lowering and mating of components, where the geometry and undesired pendulation of the suspended load play a significant role [135]. Tugger lines are often used to control these oscillations, enabling operations in broader weather conditions. Active and damping tugger lines ([30, 136], respectively) apply precise tensile forces directly to the load in an attempt to reduce its motion. Limiting the actuator usage is possible when it is combined with the vessel's dynamic positioning system [133]. However, beyond the control design itself, the effectiveness of the tugger line also depends on factors such as winch capacities and human intervention, which are challenging to integrate into numerical models [137]. This limitation highlights opportunities for further exploration of other motion compensation control techniques, such as the one proposed here.

Figure 7.1: Semi-submersible crane vessel (HMC-*Sleipnir*) during the offshore campaign for the project DOT6000-FOX in the *Princes Amaliawindpark* [43].

7.2. DOT6000-FOX offshore campaign

The project "Floating Installation Offshore XXL Wind Turbines" (DOT6000-FOX), funded by the Netherlands Enterprise Agency (RVO), aimed to assess the cost-effectiveness of heavy-lift vessels for offshore wind turbine installation compared to conventional methods, broadening the industry's installation capabilities. As part of this initiative, the first-ever floating installation of a full OWT was successfully carried out in October 2021 at the *Princess Amalia Wind Farm* in the Netherlands. The bottom-founded turbine had a capacity of 2.75 MW. Furthermore, a novel connection method for OWT components, the slip-joint, was tested on full-scale during the campaign. This boltless yet secure connection reduces the installation time and adheres to strict regulations regarding precision and oscillation control during a successful mating process [138].

The project consortium included Delft Offshore Turbine B.V. (DOT), responsible for the OWT; Heerema Marine Contractors Nederland SE (HMC), using Sleipnir, the largest semi-submersible HLV to date; and Delft University of Technology (TU Delft), which developed custom sensors to monitor the motion of turbine components during the offshore campaign (Figure 7.1).

The sensor units were designed and developed in partnership with the Técnico Solar Boat (TSB) team from the Instituto Superior Técnico in Portugal and provided a significant advantage by allowing synchronization with onboard measurement systems. Wind, wave, and tugger line loads as well as hoisting cable length data were measured during the campaign by an array of radars and sensors, which were strategically located on the vessel as shown in Figure 7.2a. These included anemometers for wind and wave radars for sea state measurements. The motion measurements were performed using the custom motion tracking modules placed at different key locations of the crane-payload system.

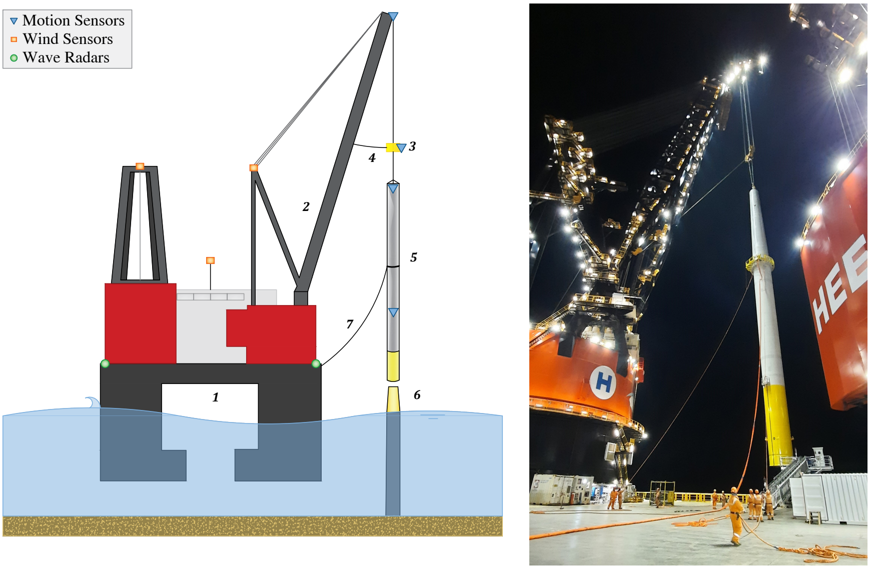

(a) (b)

Figure 7.2: (a) Schematic diagram of the tower installation: 1. Floating vessel, 2. Heavy lift crane, 3. Lifting block/hook, 4. Active (damping) tugger line, 5. Wind turbine tower, 6. Monopile head and 7. Passive (manual) tugger line. Symbols indicate motion sensors, wind sensors, and wave radars. (b) Tugger lines attached to the OWT tower during installation: The active tugger line is attached to the hook block and the passive manual tugger line is attached to the lower part of the tower.

This offshore campaign provided valuable insights into the installation of an OWT, addressing the limited availability of full-scale application data in the public domain. Scaling challenges inherent to physical testing arise due to the differing scaling laws for wind and wave loads, leading to inconsistencies referred to as the "Dilemma in Model Testing" [139]. By analysing the collected measurements, this study overcomes these challenges, offering a detailed examination of the full-scale dynamics of an OWT tower installation using a floating vessel [140].

The stage of the OWT installation that is reported here pertains to the set-down phase, during which the tower is suspended by the crane and gradually lowered towards the foundation (monopile). A schematic illustration of this operation is presented in Figure 7.2a. Fundamentally, the system comprises the floating crane vessel and the suspended load subsystem that resembles a triple pendulum. The constituent elements of this triple pendulum are the crane cable and the block hook, as well as the sling linking the hook to the attachment point of the suspended load. This load corresponds to a hollow cylindrical structure representing the OWT tower. The numerical values for the parameters defining this system are listed in Table 7.1.

To mitigate external disturbances caused by wind and waves, two tugger line systems were deployed during the installation operation (Figure 7.2b). An active tugger line was attached to the hook block to dampen the block's motion, thereby reducing the vibrations of the suspended tower. In addition, a set of passive tugger lines was connected directly to the tower above its centre of gravity. These passive tugger lines were secured to a cleat and manually operated by the crew to further stabilize the tower during installation.

Table 7.1: Overview of the system parameters.

Parameter	Notation	Value	Unit
Crane Tip Height	H_k	180	m
Tower Height	L	74	m
Average Tower Diameter	D_{T}	3.6	m
Average Tower Thickness *	τ_{T}	30	mm
Tower Mass	M	226	ton
Block Mass	m	45	ton
Sling Length	ℓ_s	10.6	m
Passive Tugger Length	L_{PT}	20	m
Passive Tugger Diameter	d_{PT}	64	mm
Passive Tugger Young's Modulus	E_{PT}	113	GPa

7.2.1. Analysis of the tower motions during installation

In the following, the dataset from one of the two separate lifts is presented to examine the impact of varying external environmental excitations and lowering speeds on the response of the overall dynamical system. During the lowering process, the crane's orientation and boom angle were held constant, with the hoisting length being the only parameter that varied as the tower was lowered towards the monopile. The time series of the cable length is presented in Figure 7.3a.

For the in-plane motion of the two components of the tower-block system, the power density spectra are analysed to identify the frequency range that contributes most significantly to the tower's motions. Figure 7.3b illustrates the power density spectra derived from sensor measurements to identify the excitations that contribute to the observed amplitudes. The acceleration spectra at three critical locations of the crane-payload system (s_α) are presented, alongside the wave (s_w) and active tugger line (s_F) spectra. The analysis identifies the primary contributors to the motions of the crane-payload system, linking them to the excitation of its various natural frequencies. The wave action on the vessel emerges as the dominant source of motion, a conclusion further validated by Figure 7.3c, which presents the resulting positional cumulative standard deviation (σ_p), determined from the measured data for the motion of the hook block and upper tower.

Although the direct action of the wind excites the second mode of the system through vortex-induced vibrations, its contribution to the overall motion is relatively small. These

---

* Educated approximation with reference to a turbine of similar geometry as detailed in [141].

findings are corroborated by the frequency-domain analyses conducted by Domingos et al. [142], which highlight that wave loads predominantly constrain the installation workability. Workability is defined as the percentage of time during which operational limits are not exceeded. Notably, tower motion tends to decrease with increasing tower size, and sling length has a minimal effect on the overall dynamics [142].

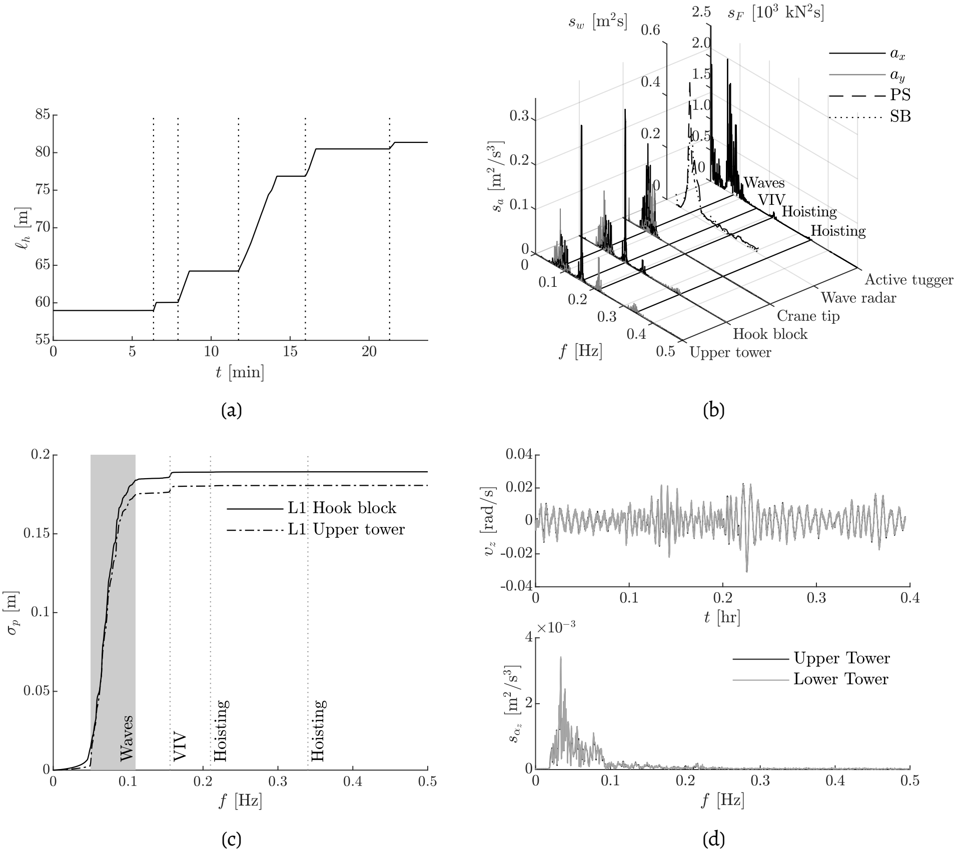

(a) (b)

(c) (d)

Figure 7.3: (a) Payout length as a function of time during the tower installation, (b) Power density spectra for the in-plane accelerations, the wave radar, and the active tugger line force as measured during Lift 1. The translational accelerations in the xy plane are denoted as a_x and a_y for the x- and y-axis, respectively. The abbreviations PS and SB denote the port side and starboard side of the vessel, respectively. (c) Cumulative standard deviation spectrum of the hook-block and upper tower during Lift 1. (d) Time series of the gyroscope measurement for the rotation around z-axis of the tower, and the corresponding power density spectrum for the upper and lower tower sensor data.

To quantify the rotational vibration of the tower during installation, Figure 7.3d presents the time series of the gyroscope measurements around the z-axis of the tower, along with the corresponding power density spectrum for the upper and lower tower sensor data. The rotation around the longitudinal axis of the tower is uniform, as expected for a rigid body when measured at two different heights. The oscillations are primarily present at the frequency of the wave action.

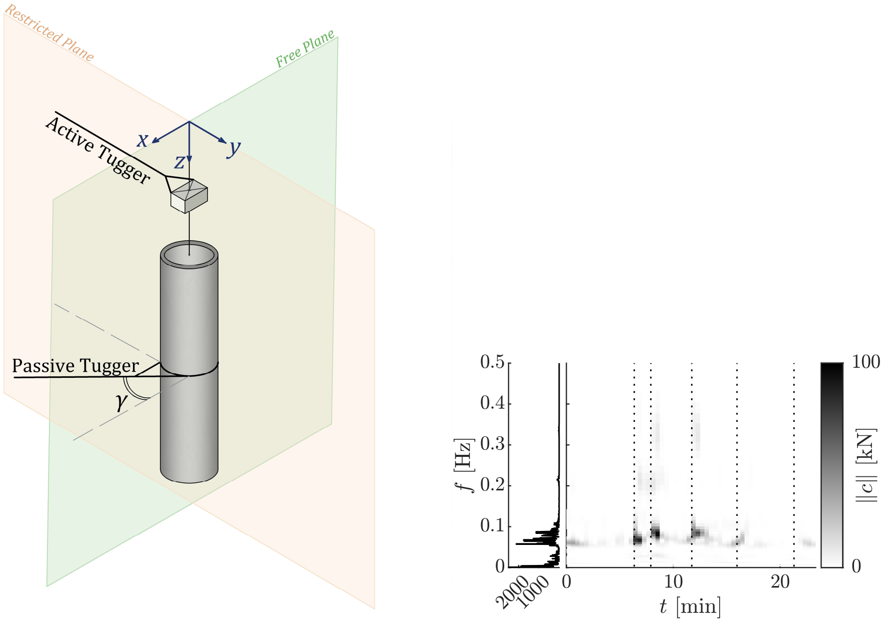

(a)

(b)

Figure 7.4: (a) Active and passive tugger line orientation, (b) Time-frequency plot of the active tugger tension during Lift 1. The dashed vertical lines denote the moments when the tower was lowered. For each component, the corresponding power density spectrum is presented on the left-hand side.

The motion of the system is restricted by the use of tugger lines. In Figure 7.4, the spatial tugger line placement is presented alongside the orientation of the axes selected as the frame of reference. The measured active tugger tension ranges from 0 kN to 100 kN and is excited at the wave frequency.

The presented full-scale measurements reveal the vibrational modes that are most prevalent during floating installations, emphasizing the degrees of freedom (DOFs) that experience the highest amplitudes and therefore require direct control. These DOFs are the rotations of the payload around its three local axes and the associated displacements resulting from these motions (6 DOFs of a rigid body). This observation aligns with numerically simulated results of the dynamic response of an OWT suspended by a floating crane, as reported by [37]. In that work, the estimated maximum amplitudes for the surge, sway, heave, roll, pitch, and yaw motions of the OWT (rigid body DOFs) were 0.59 m, 1.99 m, 0.31 m, 2.18°, 0.94°, and 8.42°, respectively.

7.3. Numerical simulation of an OWT tower installation

In this section, a numerical simulation is presented to model the installation of the full-scale OWT tower, with a focus on the component's response during the lifting and suspension phases. This simulation builds upon the findings reported during the DOT6000-FOX offshore campaign. The objective is to develop a control scheme aimed at mitigating undesired vibrations of the component, employing the magnet-to-magnet contactless techniques extensively explored throughout this thesis.

7.3.1. Equations of motion of a suspended OWT

The triple pendulum depicted in Figure 7.5 consists of an inextensible cable of length ℓ_h supporting a mass m representing the hook block, a (sling) rope of length ℓ_s connecting the block to the suspension point of a thin-walled cylinder with total mass M, which is evenly distributed along its length L. This configuration features seven degrees of freedom in 3D, corresponding to the rotational angles of the pendulum components in the three planes: xz-, yz-, and xy-plane. The equations of motion governing the 3D system are presented in Appendix A, derived based on the methodology applied to a similar crane-payload system as described in [47].

Assuming that the rotation angles remain small, the motions in the xz- and yz-planes decouple. As a result, the three-dimensional motion can be approximated as the superposition of the motions of two planar triple pendula. With this simplification, the analysis focuses on developing a control strategy for a single planar model, with the understanding that a similar methodology can be applied to the other plane.

For the planar dynamical system, the degrees of freedom include the pendulum angle of the point mass, η, the sling angle, ζ, and the rotational angle of the cylindrical payload around its top suspension point, ψ. Additionally, the cylinder's rotation about its longitudinal z-axis, ϕ, representing torsional motion in rigid body dynamics, constitutes the remaining unknown state of the system. The configuration is illustrated in Figure 7.5.

For simplicity, the tower is modelled as a cylindrical rigid body with a uniform diameter of $2R$. This assumption facilitates the derivation of the equations of motion and the system's analysis by reducing the complexity associated with the varying geometry of an offshore wind turbine tower (tapered cylinder), while still capturing the essential dynamics of the structure.

The vessel, despite utilising dynamic positioning, is influenced by wave and current forces, which translate into crane tip motion, $\vec{h}$. In this planar representation, the motion $\vec{h}$ comprises two components, h_x & h_z. This study focuses solely on the horizontal component ($h_x = h$), under the assumption that the crane's heave compensation mechanism effectively attenuates a significant portion of the undesired heave motion of the payload. To simplify the simulation of the system, the following assumption has been applied: The cable of the hook and sling are modelled as rigid, massless elements during the derivation of the EOMs.

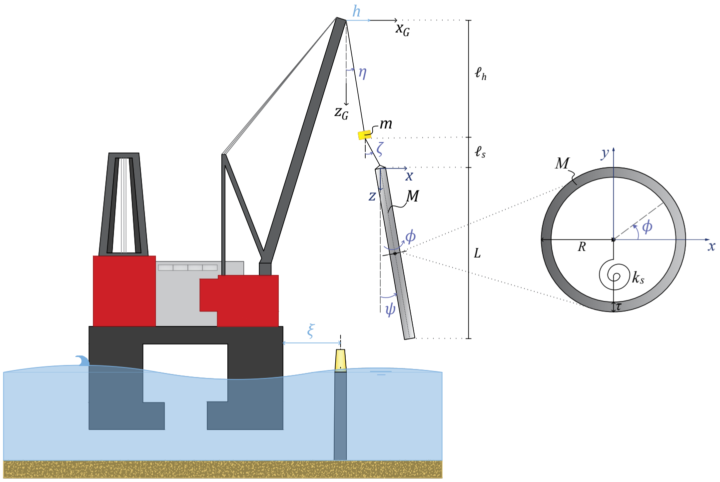

Figure 7.5: Schematic of the numerical model set-up: (a) Crane-payload configuration in $x_G z_G$-plane, (b) Cylindrical mass rotation in xy-plane.

To characterize the motion of the system, the positional vectors of its components are expressed in the global frame of reference ($x_G y_G z_G$) as follows:

$$\vec{P}_{h_G} = \vec{P}_h + \vec{h} = \begin{bmatrix} \ell_h \sin(\eta) \\ 0 \\ \ell_h \cos(\eta) \end{bmatrix} + \begin{bmatrix} h \\ 0 \\ 0 \end{bmatrix}, \tag{7.1a}$$

$$\vec{P}_{s_G} = \vec{P}_{h_G} + \vec{P}_s = \vec{P}_{h_G} + \begin{bmatrix} \ell_s \sin(\zeta) \\ 0 \\ \ell_s \cos(\zeta) \end{bmatrix}, \tag{7.1b}$$

$$\vec{P}_{c_G} = \vec{P}_{s_G} + \vec{P}_c = \begin{bmatrix} nL \sin(\psi) \\ 0 \\ nL \cos(\psi) \end{bmatrix}, \tag{7.1c}$$

where $\vec{P}_c$, $\vec{P}_s$, and $\vec{P}_h$ denote the position vectors of the cylinder's point of interest, the sling rope endpoint, and the hook mass, respectively, relative to the local frame of reference (xyz). The parameter n indicates the fraction of the cylinder's length at the point of interest, measured from its suspension point. For example, at the cylinder's centre of gravity (COG), $n = 0.5$.

The kinetic $\mathcal{K}$ and potential $\mathcal{U}$ energy of the dynamical system are given by

$$\mathcal{K} = \frac{1}{2} M \left\| \vec{P}_{c_G} \right\|^2 + \frac{1}{2} m \left\| \vec{P}_{h_G} \right\|^2 + \frac{1}{2} I_y (\dot{\psi})^2 + \frac{1}{2} I_z (\dot{\phi})^2, \tag{7.2a}$$

$$\mathcal{U} = Mg\left(\ell_h + \ell_s + L - \hat{k}\vec{P}_{c_G}\right) + mg\left(\ell_h - \hat{k}\vec{P}_{h_G}\right) + \frac{1}{2}k_s(\phi)^2, \tag{7.2b}$$

where $\hat{k}$ represents the unit vector of the vertical z-axis, I_y and I_z are the moments of inertia for the rotation of the cylinder around the respective axes. $\vec{P}_{c_G}$ correspond to the position vector of the COG of the cylinder.

The Lagrangian ($\mathcal{L} = \mathcal{K} - \mathcal{U}$) of the system is formulated as

$$\frac{\mathrm{d}}{\mathrm{d}t}\left(\frac{\partial \mathcal{L}}{\partial \dot{\vec{q}}}\right) - \frac{\partial \mathcal{L}}{\partial \vec{q}} = 0 \text{ with } \mathcal{L} = \mathcal{K} - \mathcal{U} \text{ and } \vec{q} = \left[\psi, \eta, \zeta, \phi\right]^{\mathrm{T}}, \tag{7.3}$$

in which $\vec{q}$ describes the vector of the four unknown states of the system. Evaluating Equation (7.3) using the expressions from Equation (7.2), yields the following nonlinear equations of motion:

$$\left(\frac{ML^2}{4} + I_y\right)\ddot{\psi} + \frac{MgL}{2}\sin(\psi) + \frac{ML\ell_h}{2}\cos(\eta - \psi)\ddot{\eta} + \frac{ML\ell_s}{2}\cos(\zeta - \psi)\ddot{\zeta} \tag{7.4a}$$

$$= +\frac{ML\ell_h}{2}\sin(\eta - \psi)\dot{\eta}^2 + \frac{ML\ell_s}{2}\sin(\zeta - \psi)\dot{\zeta}^2 - \frac{ML}{2}\cos(\psi)\ddot{h}$$

$$(M + m)\,\ell_h^2\ddot{\eta} + (M + m)g\ell_h\sin(\eta) + \frac{ML\ell_h}{2}\cos(\eta - \psi)\ddot{\psi} + M\ell_h\ell_s\cos(\eta - \zeta)\ddot{\zeta} \tag{7.4b}$$

$$= -\frac{ML\ell_h}{2}\sin(\eta - \psi)\dot{\psi}^2 + M\ell_h\ell_s\sin(\eta - \zeta)\dot{\zeta}^2 - (M + m)\ell_h\cos(\eta)\ddot{h}$$

$$M\ell_s^2\ddot{\zeta} + Mg\ell_s\sin(\zeta) + \frac{ML\ell_s}{2}\cos(\zeta - \psi)\ddot{\psi} + M\ell_h\ell_s\cos(\eta - \zeta)\ddot{\eta} \tag{7.4c}$$

$$= -\frac{ML\ell_s}{2}\sin(\zeta - \psi)\dot{\psi}^2 + M\ell_h\ell_s\sin(\eta - \zeta)\dot{\eta}^2 - M\ell_s\cos(\zeta)\ddot{h}$$

$$I_z\ddot{\phi} + k_s\phi = 0 \tag{7.4d}$$

7.3.2. Modal analysis

The modal analysis can only be performed on a linear system. Therefore, the displacements of the hanging components are assumed to be small relative to the pendulum lengths, enabling the use of the small angle approximation ($\sin(q) \approx q$ and $\cos(q) \approx 1$). Under this assumption, the linearised versions of the nonlinear equations of motion in Equation (7.4) are reformulated into a matrix representation as follows:

$$\mathbf{M}\ddot{\vec{q}} + \mathbf{K}\vec{q} = \vec{T}, \tag{7.5a}$$

$$\begin{bmatrix} \frac{ML^2}{4} + I_y & \frac{ML\ell_h}{2} & \frac{ML\ell_s}{2} & 0 \\ \frac{ML\ell_h}{2} & (M+m)\,\ell_h^2 & M\ell_h\ell_s & 0 \\ \frac{ML\ell_s}{2} & M\ell_h\ell_s & M\ell_s^2 & 0 \\ 0 & 0 & 0 & I_z \end{bmatrix}\begin{bmatrix}\ddot{\psi} \\ \ddot{\eta} \\ \ddot{\zeta} \\ \ddot{\phi}\end{bmatrix} + \begin{bmatrix} \frac{MgL}{2} & 0 & 0 & 0 \\ 0 & (M+m)g\ell_h & 0 & 0 \\ 0 & 0 & Mg\ell_s & 0 \\ 0 & 0 & 0 & k_s \end{bmatrix}\begin{bmatrix}\psi \\ \eta \\ \zeta \\ \phi\end{bmatrix} \tag{7.5b}$$

$$= -\begin{bmatrix} \frac{ML}{2} \\ (M+m)\ell_h \\ M\ell_s \\ 0 \end{bmatrix} \ddot{h},$$

where **M** and **K** are the mass and stiffness matrices, respectively.

The natural frequencies of the system can, now, be determined by solving the eigenvalue problem [129]:

$$\det\left(\mathbf{K} - \omega_n^2 \mathbf{M}\right) = 0, \tag{7.6}$$

with the non-trivial, real, and positive solutions ω_n yielding the natural frequencies. To obtain the magnitude of the natural frequencies in Hz, the following well-known identity is used: $f_n = \omega_n / 2\pi$. Four modes of motion are identified, corresponding to the degrees of freedom of the dynamical system: three pendulum modes and one torsional vibrational mode, illustrated alongside their respective natural frequencies in Figure 7.6.

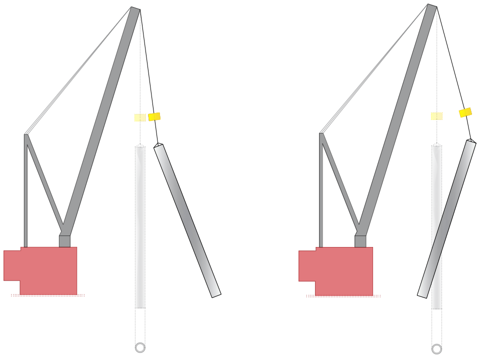

(a) Mode 1, $f_1 = 0.043$ Hz (b) Mode 2, $f_2 = 0.088$ Hz

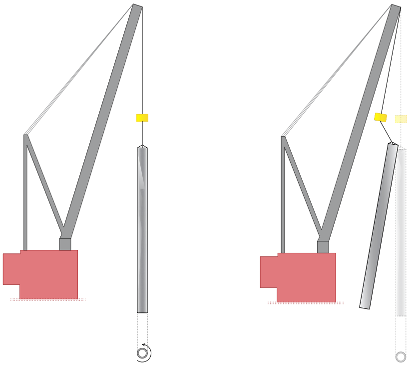

(c) Mode 3, $f_3 = 0.091$ Hz (d) Mode 4, $f_4 = 0.420$ Hz

Figure 7.6: Modal shapes of the suspended cylinder triple pendulum.

7.4. Control design

7.4.1. Arrangement of the actuators

As the torsional degree of freedom (ϕ) is decoupled from other degrees of freedom with respect to both inertia and stiffness, it requires a dedicated independent control torque (T_f, Figure 7.7). To control the rotational degree of freedom (ψ) in the $x_G z_G$-plane, a proposed strategy involves generating torque around the cylinder's centre of gravity by applying two forces at different heights on the suspended load (F_{t1} & F_{t2}, Figure 7.7). Note that the rotation angle ψ results in the translation of the suspended load in the plane, and therefore the two actuators are referred to as translational controllers.

The forcing configuration, depicted in Figure 7.7, is designed to ensure full controllability of the system's vibrations. The proposed configuration (blue arrows) is adopted due to its added advantage of directly influencing the motion of the suspended payload. This arrangement effectively facilitates the control of various potential modes of motion, such as the even-number vibrational modes (Figure 7.6). It should be noted that the conventional approach to motion compensation during the offshore campaign involves an active tugger line directly attached to the hook block and a passive tugger to control the motions of the hanging tower (Figure 7.4a). This conventional approach may only indirectly control the torsional vibrations around the longitudinal axis of the cylinder.

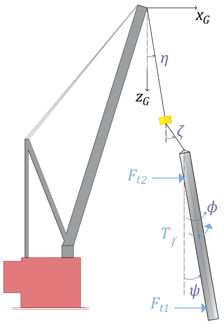

Figure 7.7: Proposed control configuration for full system controllability. The configuration of the control forces is represented by the blue arrows.

As established in the introduction, the heave motion of the suspended component is not explicitly controlled in this study, as it is assumed to be sufficiently compensated by the crane's active heave compensation system. The present study focuses on a representative snapshot of the installation process—specifically, the lifting phase in which the component remains freely suspended. During this phase, the magnetic actuators are assumed to be fixed at predetermined locations along the length of the payload. In a more realistic scenario involving the lowering of the component, the spatial control of the vertical position of the external magnetic actuators, as well as the distribution of the mounted recipient

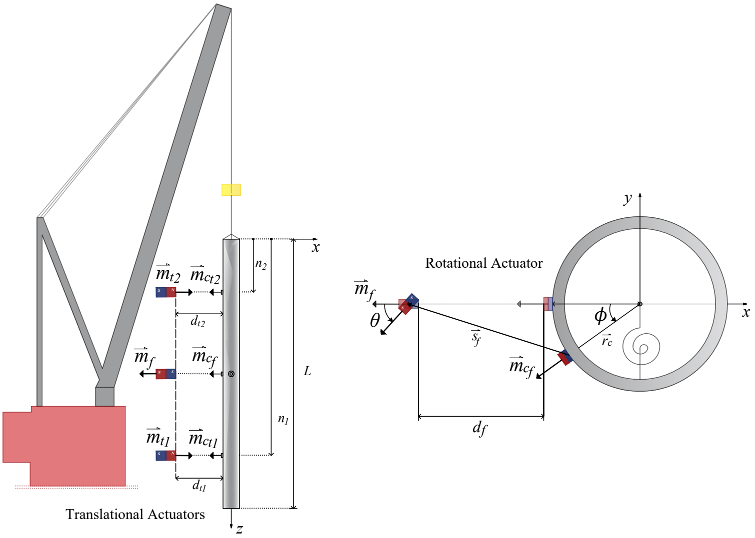

Figure 7.8: Actuator arrangement for torsional and translational control.

magnets at varying heights, would require careful consideration to ensure continuous and effective control.

7.4.2. Control strategy

The control setup adheres to the scheme introduced in the combined control approach (Chapter 6) and the selected control arrangement. This arrangement includes two actuators for translational control (in-plane rotation) and one actuator for torsional vibration control, and it is detailed in Figure 7.8. The translational controllers regulate the strength and polarity of two magnetic dipole moments, M_{t_1} & M_{t_2}, while the orientation of the magnetic field of a third dipole moment, M_f, is employed to manipulate the torsional rotation of the suspended cylinder.

The vectors representing the four translational magnetic dipole moments are given by

$$\vec{m}_{t_\kappa} = M_{t_\kappa} \begin{bmatrix} 1 \\ 0 \\ 0 \end{bmatrix} \text{ and } \vec{m}_{ct_\kappa} = -M_{ct_\kappa} \begin{bmatrix} \cos(\phi) \\ \sin(\phi) \\ 0 \end{bmatrix}, \tag{7.7}$$

where the subscript $\kappa = 1$ or 2 indicates the locations of the two magnetic forces applied on the cylinder. The magnetic strength of each translational controller is governed by a PID control equation, expressed as:

$$M_{t_\kappa} = K_{p_\kappa} e + K_{i_\kappa} \int e \, \mathrm{d}t + K_{d_\kappa} \dot{e}, \text{ with } e = \xi - n_\kappa L \psi - h, \tag{7.8}$$

where the PID gains are constant values with $K_p, K_i, K_d > 0$, and ξ represents the desired translational motion (relative motion of the vessel with respect to a stationary point, e.g. a monopile support structure). The general subscript notation κ is either 1 for the lower tower or 2 for the upper tower translational controller. Since the desired motion pertains to a desired stationary target position, $\xi = 0\,\mathrm{m}$, the integral gain of the controller plays a critical role in eliminating any potential offset error in the system's steady-state response.

The concurrent action of the two PID-driven forces aims to generate a torque around the centre of gravity of the suspended structure, ensuring that the cylinder remains as vertical as possible with minimal error. The arm of each individual torque is denoted as n_1 for the force applied on the lower tower and n_2 for the force on the upper tower, representing the two distinct magnetic dipole pairs.

The magnetic dipole moments of the torsional control pair are expressed as

$$\vec{m}_f = -M_f \begin{bmatrix} \cos(\theta) \\ \sin(\theta) \\ 0 \end{bmatrix} \text{ and } \vec{m}_{cf} = -M_{cf} \begin{bmatrix} \cos(\phi) \\ \sin(\phi) \\ 0 \end{bmatrix}. \tag{7.9}$$

In line with Equation (6.17) (Chapter 6), the control rule for the torsional mode is defined by

$$\theta = \Delta\theta \tanh(\beta\dot{\phi}), \text{ with } \Delta\theta = \text{const.}, \tag{7.10}$$

where θ is the orientation angle that corresponds to the desired equilibrium $\phi_e = 0^\circ$, and $\Delta\theta$ the chosen fluctuation step for the total orientation θ. The parameter β controls the steepness of the transition between the values around zero.

The methodology can be employed for the derivation of the magnetically-induced torques, which act as external forcing to the system (Equation (6.5) to Equation (6.7)). The fully nonlinear equations of the system (Equation (7.4)) are rewritten with the additional terms to account for the magnetic interaction:

$$\left(\frac{ML^2}{4} + I_y\right)\ddot{\psi} + \frac{MgL}{2}\sin(\psi) + \frac{ML\ell_h}{2}\cos(\eta-\psi)\ddot{\eta} + \frac{ML\ell_s}{2}\cos(\zeta-\psi)\ddot{\zeta} \tag{7.11a}$$
$$= \frac{ML\ell_h}{2}\sin(\eta-\psi)\dot{\eta}^2 + \frac{ML\ell_s}{2}\sin(\zeta-\psi)\dot{\zeta}^2 - \frac{ML}{2}\cos(\psi)\ddot{h} + T_\psi$$

$$(M+m)\,\ell_h^2\ddot{\eta} + (M+m)g\ell_h\sin(\eta) + \frac{ML\ell_h}{2}\cos(\eta-\psi)\ddot{\psi} + M\ell_h\ell_s\cos(\eta-\zeta)\ddot{\zeta} \tag{7.11b}$$
$$= -\frac{ML\ell_h}{2}\sin(\eta-\psi)\dot{\psi}^2 + M\ell_h\ell_s\sin(\eta-\zeta)\dot{\zeta}^2 - (M+m)\ell_h\cos(\eta)\ddot{h} + T_\eta$$

$$M\ell_s^2\ddot{\zeta} + Mg\ell_s\sin(\zeta) + \frac{ML\ell_s}{2}\cos(\zeta-\psi)\ddot{\psi} + M\ell_h\ell_s\cos(\eta-\zeta)\ddot{\eta} \tag{7.11c}$$
$$= -\frac{ML\ell_s}{2}\sin(\zeta-\psi)\dot{\psi}^2 + M\ell_h\ell_s\sin(\eta-\zeta)\dot{\eta}^2 - M\ell_s\cos(\zeta)\ddot{h} + T_\zeta$$

$$I_z\ddot{\phi} + k_s\phi = T_\phi \tag{7.11d}$$

The additional magnetically-induced terms are defined by

$$\vec{T} = \begin{bmatrix} T_\psi & T_\eta & T_\zeta & T_\phi \end{bmatrix}^\mathrm{T} = -\begin{bmatrix} \frac{\partial W_m}{\partial \psi} & \frac{\partial W_m}{\partial \eta} & \frac{\partial W_m}{\partial \zeta} & \frac{\partial W_m}{\partial \phi} \end{bmatrix}^\mathrm{T}, \tag{7.12}$$

where the total potential energy due to the magnetic interactions W_m is given by

$$W_m = -\vec{m}_{cf} \cdot \vec{B}_f - \sum_{\kappa=1}^{2} \vec{m}_{ct_\kappa} \cdot \vec{B}_{t_n\kappa}, \tag{7.13}$$

in which $\vec{B}_f$ and $\vec{B}_{t_\kappa}$ are the magnetic fields exerted by the EMs ($\vec{m}_f$ or $\vec{m}_{t_\kappa}$) to the location of the respective dipoles on the cylindrical mass ($\vec{m}_{cf}$ or $\vec{m}_{ct_\kappa}$).

7.4.3. Stability requirement

Evaluating Equation (7.13) using the Taylor series expansions of the trigonometric terms of ϕ, ψ, η, ζ up to the second order around the equilibrium position 0° yields

$$W_m = K_1\phi^2 + K_2\phi + K_3\psi^2 + K_4\psi + K_5\eta^2 + K_6\eta + K_7\zeta^2 + K_8\zeta + C, \tag{7.14}$$

where the coefficients K_1 to K_8 and C are functions of the dipole moment magnitudes, the fluctuation angle the initial distances of the magnets, the geometry of the cylindrical structure and the crane tip motion. The full expressions of these coefficients can be found in Appendix B.

Evaluating Equation (7.11d) using Equation (7.14), a stability requirement is derived from the torsional equation of motion, expressed as

$$I_z\ddot{\phi} + (k_s + 2K_1)\phi = -K_2 \rightarrow k_s > -2K_1, \tag{7.15}$$

in which the coefficient K_1 is given by

$$\begin{aligned} K_1 =& -\frac{M_{ct_1}M_{t_1}\mu}{4\pi(d_1+h)^5}\left((d_1+h)^2 + 6R(d_1+h) + 6R^2\right) \\ & -\frac{M_{ct_2}M_{t_2}\mu}{4\pi(d_2+h)^5}\left((d_2+h)^2 + 6R(d_2+h) + 6R^2\right) \\ & +\frac{M_{cf}M_{f}\mu}{4\pi(d_f+h)^5}\left((d_f+h)^2 + 6R(d_f+h) + 6R^2\right) \end{aligned} \tag{7.16a}$$

$$K_1 = (-M_{t_1} - M_{t_2} + M_f)\tilde{K}_1, \tag{7.16b}$$

where $\tilde{K}_1 = \frac{\mu}{4\pi(d+h)^5}\left((d+h)^2 + 6R(d+h) + 6R^2\right)$ with $d_1 = d_2 = d_f = d$ and the mounted magnetic dipole moments $M_{ct_1} = M_{ct_2} = M_{cf} = 1$. The final stability condition reads

$$(M_{t_1} + M_{t_2} - M_f) < \frac{k_s}{2\tilde{K}_1}. \tag{7.17}$$

This condition implies that the magnetic dipole actuators for translation should be either equal to or weaker in strength than the torsional actuator.

7.5. Controlled response

The full nonlinear system is solved numerically in the time domain using MATLAB's function *ode45*, an explicit Runge-Kutta numerical method with a variable step. The dynamical system's parameters are listed in Table 7.2. In addition, the initial conditions for the planar rotations are trivial, namely $\eta_0 = \zeta_0 = \psi_0 = \dot{\eta}_0 = \dot{\zeta}_0 = \dot{\psi}_0 = 0$. The desired position of the suspended cylinder is the global equilibrium position, defined as $\phi = \psi = 0°$. An acceptable (operationally safe) limit is set for all planar rotational angles to remain within the range of $[-1°, 1°]$. The magnitude of the torsional magnetic dipole moment is chosen to be equal to $M_f = 10^{11}$ Am^2.

Table 7.2: System parameters for the full-scale controlled vibrations.

$M_{ct_{1,2}}, M_{c_f}$ [Am^2]	$d_{t_{1,2}}, d_f$ [m]	K_{p_1} [N/m]	K_{i_1} [N/ms]	K_{d_1} [Ns/m]	$\Delta\theta$ [°]
1	1	10^{11}	10^{9}	10^{11}	5
ϕ_0 [°]	$\dot{\phi}_0$ [°/s]	K_{p_2} [N/m]	K_{i_2} [N/ms]	K_{d_2} [Ns/m]	k_s [N/m]
10	0	10^{12}	10^{10}	10^{12}	10^{6}

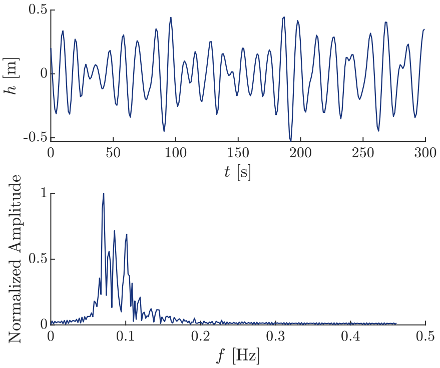

Figure 7.9: Amplitude time series and frequency content of the crane tip excitation signal.

A realistic signal is prescribed as external excitation for the pivot point h of the triple pendulum. This signal corresponds to a full-scale time series derived in Chapter 4 from the simulation of an OWT tower installation performed by the fictional semi-submersible vessel *Prometheus* ([44]). The simulation utilized a JONSWAP spectrum characterized by a significant wave height $H_s = 3\,\mathrm{m}$ and a peak period $T_p = 8\,\mathrm{s}$. The crane tip response is depicted in Figure 7.9, with its frequency content in close agreement with results recorded during the offshore campaign (Figure 7.3c).

7.5.1. Torsional vibrations

Figure 7.10 illustrates the response of the suspended cylinder with respect to the torsional mode of vibration, ϕ. The torsional controller effectively attenuates the motion induced by the non-trivial initial conditions, guiding the system to the desired position of $\phi = 0^\circ$. The envelope of the decaying motion (the line connecting the motion peaks) exhibits a slightly curved and gradual descent, as the torsional control employs a smoother approximation of the Coulomb friction scheme (Equation (7.10)). This behaviour is mirrored in the time series of the controller's magnetic field orientation, θ, which closely follows the decaying angular velocity, as anticipated.

The integration of the mechanical power, $P_f = T_f\dot{\phi}$, over the entire simulation yields the cumulative torsional actuation energy, which is $E_{f,\mathrm{tot}} = -15.2\,\mathrm{kJ}$. The negative sign indicates that energy was extracted from the system, which is consistent with the chosen control approach. The transient response is just over a minute, which is considered brief given the total duration of tower set-down (20 min).

7.5.2. Translational vibrations

The controlled response of the cylinder with respect to its movement in the xz-plane is detailed in Figure 7.11. The displacements of key points on the cylindrical payload are presented: X_{c_1} and X_{c_2} correspond to the positions of the mounted permanent magnets, while X_e and $X_{e,nc}$ represent the response of the free end of the cylinder with and without the application of magnetic forces, respectively. The results demonstrate effective vibration attenuation, with motion at all measured points converging to the desired position, $\xi = x_n = 0\,\mathrm{m}$ in the global reference frame.

A minor offset is observed in the displacement of the two points below the centre of gravity (X_{c_1} and X_e), reaching a maximum value of $-0.10\,\mathrm{m}$ in steady state. This small error could be reduced by slightly increasing the integral gain $K_{i,1}$ of the PID controller. The displacement error corresponds to a slight negative tilt of the cylinder (towards the controllers), as reflected in the angle time series in Figure 7.11b. Here, the mean value of the angle ψ is slightly negative but remains within acceptable bounds of $\pm 1^\circ$.

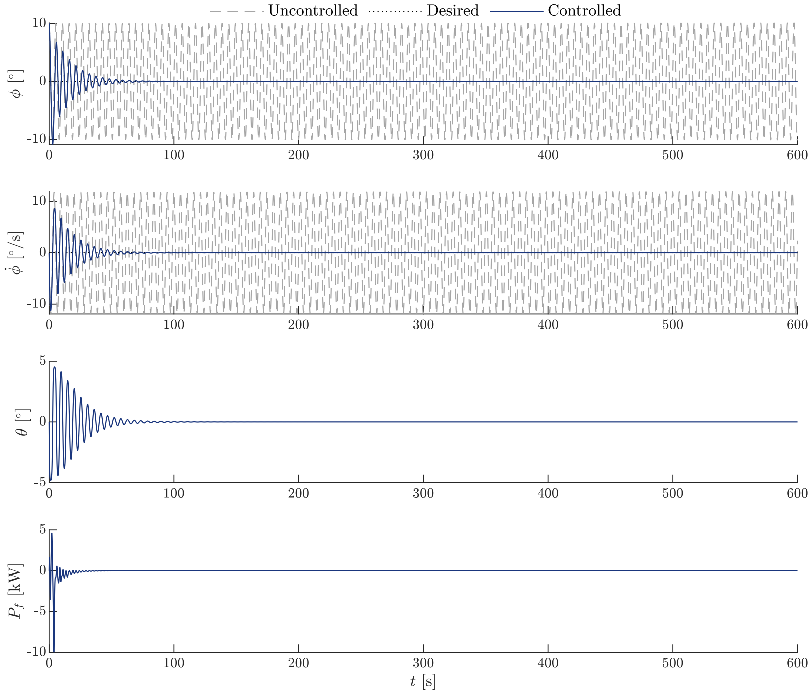

7

Figure 7.10: Controlled torsional vibrations of the crane-payload system: Time series of (a) angular displacement ϕ, (b) angular velocity $\dot{\phi}$, (c) orientation angle θ, and (d) control actuation power P_f.

In terms of magnetic dipole strengths, the electromagnet and its corresponding mounted magnet at $L_1 = 0.8L$ maintain a nearly constant combined dipole strength of approximately $M_{t_1}M_{ct} \approx 0.04\,\mathrm{TA}^2\mathrm{m}^4$. By contrast, the magnetic pair at $L_2 = 0.2L$ displays a more dynamic response in its effort to stabilize the cylinder. This is expected because the arm of the force with respect to its centre of rotation results in a smaller torque at this location necessitating higher force amplitudes, with a mean combined dipole strength of approximately $M_{t_2}M_{c_t} \approx 0.06\,\mathrm{TA}^2\mathrm{m}^4$. The magnetic strengths of the dipoles adhere to the stability criterion outlined in Equation (7.17), namely $M_f > M_{t_1} + M_{t_2}$.

The polarities, as determined by the mean values of the time series, indicate the two translational actuators generate repulsive forces. In the present control configuration, repulsion translates to a positive torque on the cylinder around its attachment point (tower top). The power demand for both actuators is shown in Figure 7.11d, revealing similar magnitudes. However, the upper actuator (M_{t_2}) requires slightly more effort to generate the necessary control torque.

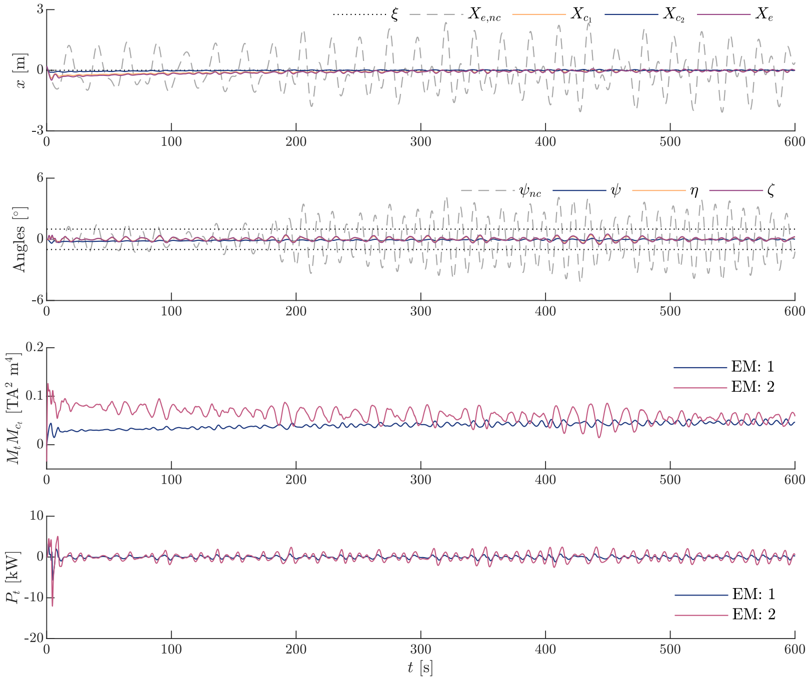

Figure 7.11: Controlled translational vibrations of the crane-payload system: Time series of (a) displacement of different locations on the cylinder against the desired position ξ, (b) angular displacements of the three components of the system against the uncontrolled response of the suspended cylinder, (c) magnetic dipole combined strength required $M_t M_{c_t}$, and (d) mechanical actuation power P_t for the two translational controllers.

The two magnetic control torques are compared in Figure 7.12a. The torsional controller exerts a torque that is one order of magnitude smaller than the total translational torque. Additionally, while the torsional torque tends to zero once the control objective is achieved, the translational control torque decreases more gradually, eventually oscillating around a steady-state value. This steady-state torque amplitude is approximately −120 kNm, reflecting a negative non-trivial value required to maintain the desired position.

The torques can be converted into actuation forces, enabling a direct comparison with the tension forces employed in conventional motion attenuation systems for suspended offshore loads, such as tugger lines. Figure 7.12b illustrates the time series of these forces, which vary depending on the actuator. For the torsional controller, the maximum force observed is approximately $F_{f,max} \approx -21$ kN. For the translational controllers, forces are applied at two different heights on the cylinder. The lower tower experiences a maximum force of $F_{t_1,max} \approx -40$ kN with a mean value of $F_{t_1,avg} \approx -12$ kN, while the upper tower experiences a significantly higher maximum force of $F_{t_2,max} \approx -338$ kN with a mean value of

$F_{t_2,avg} \approx -141\,\mathrm{kN}$. These forces correspond to controlling a suspended load weighing approximately 2260 kN. Even for these high forcing amplitudes, the ratio of the control force over the weight of the object remains low, with a maximum of approximately 15%.

A direct comparison of actuation results can be made with the offshore campaign of this project, as described earlier in the chapter, where an active tugger line attached to the crane's hook block had a capacity of 100 kN. However, this actuator's action was supplemented by manually handled passive tugger lines, as illustrated in Figure 7.4a, rendering the precise determination of its total capacity uncertain.

Furthermore, in the literature, tension forces of a comparable order of magnitude or higher are reported for floating offshore installations utilising tugger line systems. For example, Ren et al. [143] document the installation of a single blade weighing 177.4 kN, where its motion is controlled using three active tugger lines, each maintaining a mean tension of approximately 50 kN. This corresponds to a required force-to-weight ratio of 28%.

Andersen studied a lifting operation involving various configurations of tugger line systems under different environmental conditions [144]. In this study, for the free suspension of an offshore payload weighing 2000 kN, two tugger lines, each with a maximum capacity of 100 kN, were employed to control vibrations. This resulted in a required force-to-weight ratio of 10%. Although the actuation forces and the suspended load's mass in Andersen's work are comparable to those considered here for the contactless technique, it is important to note a key distinction: the load geometry in [144] was significantly simpler, i.e. it was modelled as a lumped mass. In contrast, the distributed mass in the present work introduces additional vibrational modes, making the control problem more complex.

Other studies have explored the integrated control of suspended offshore loads using active tugger systems combined with dynamic positioning (DP) control [133, 145]. In these operations, DP systems primarily address low-frequency motions, while wave-induced motions are managed by motion-compensation equipment, such as an active tugger line attached to the hook block. The authors found that employing integrated controllers reduced the reliance on motion-compensation devices across all evaluated wave conditions. Specifically, a 100 kN active tugger line was sufficient to control the motion of a hook block and a suspended load weighing 1200 kN and 6000 kN, respectively, modelled as a point-mass double pendulum. This suggests that investigating the combined use of the contactless motion control technique with the vessel's DP system could potentially reduce the actuation forces required for efficient control, further enhancing system performance.

Figure 7.12c shows an exemplary redistribution of the magnetic strengths of the dipoles. These strengths are divided almost equally amongst the interacting magnets resulting in the same combined magnetic strength (product of the magnetic dipole strengths). The mounted dipoles are permanent magnets with fixed magnetic strength. For the torsional actuator, the magnetic strength is predefined and matches the fixed strength of its corresponding permanent magnet on the cylinder. In contrast, the translational actuators exhibit a time-varying magnetic strength, governed by the PID controllers, which adjust based on the error relative to the desired set point. The magnetic field exerted by the three distinct actuators at the locations of the mounted magnetic dipoles is depicted in Figure 7.12d, aligning with the representative distribution of magnetic strength illustrated in Figure 7.12c. The magnetic field component B_x is calculated by [146]:

$$B_x = -\frac{\mu_0}{4\pi}\left(\frac{M_{t_1}}{{s_{t_1}}^3} - 3\frac{M_{t_1}(\vec{s}_{t_1}\cdot\vec{i})^2}{{s_{t_1}}^5}\right) - \frac{\mu_0}{4\pi}\left(\frac{M_{t_2}}{{s_{t_2}}^3} - 3\frac{M_{t_2}(\vec{s}_{t_2}\cdot\vec{i})^2}{{s_{t_2}}^5}\right) - \frac{\mu_0}{4\pi}\left(\frac{M_f}{{s_f}^3} + 3\frac{M_f(\vec{s}_f\cdot\vec{i})^2}{{s_f}^5}\right). \quad (7.18)$$

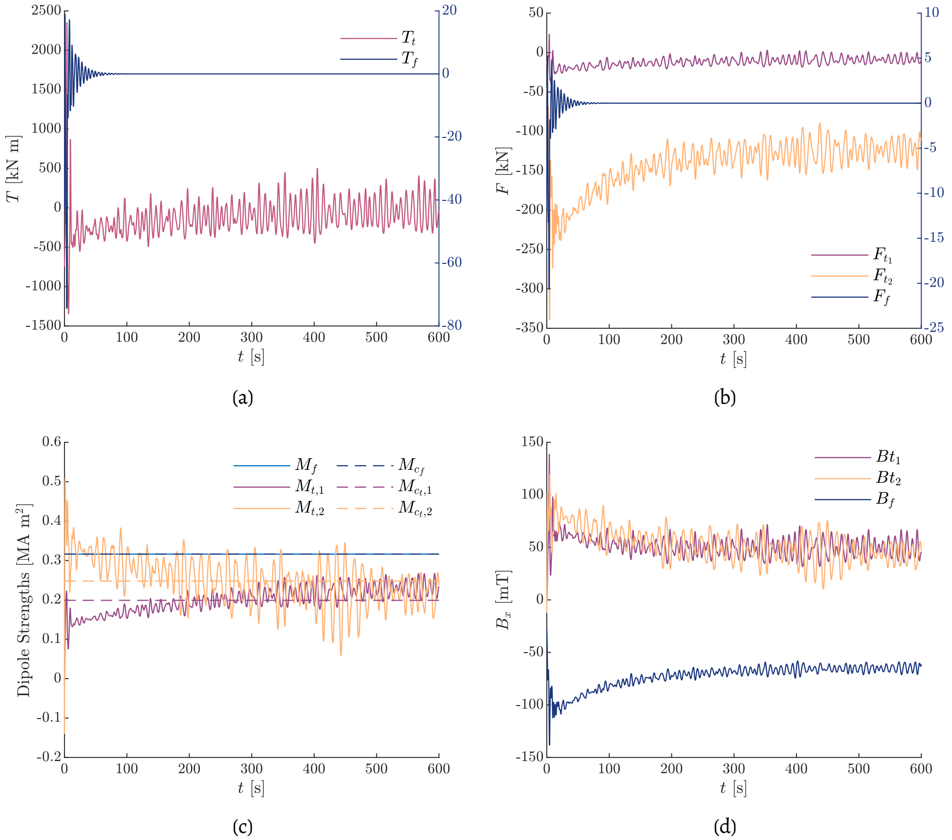

(a)

(b)

(c)

(d)

Figure 7.12: Time series of relevant control parameters: (a) Total actuation torques, (b) Actuator forces, (c) Dipole strengths, and (d) Magnetic field component B_x at the location of the three magnets mounted on the cylinder.

7.6. Conclusions

In this chapter, the development of a numerical model for controlling a full-scale suspended OWT tower using a floating crane was presented. Initially, the physical offshore campaign is detailed, analysing the tower's response during one of the lifting phases of the installation. The wave action is identified as the primary source of disturbance. The methods employed for attenuating undesired vibrations of the suspended load involved a passive tugger line attached to the tower and an active tugger line controlling the motion of the hook block.

By adopting the small-angle approximation, the equations of motion of a full 3D crane-payload system are simplified to two sets of planar pendulums. In each plane, there are three degrees of freedom: the hook pendulum angle, sling rope angle, and cylindrical payload angle. Next to that, one additional degree of freedom is relevant: the torsional angle around the payload's shaft. The derived equations of motion and subsequent modal analysis reveal the natural frequencies and mode shapes of the crane-payload system.

Building on the control techniques developed in earlier chapters, a control scheme is proposed to attenuate the motion of the tower. The scheme employs three actuators: one dedicated to mitigating torsional vibration and two targeting the planar motion. They are positioned at specific heights along the cylinder's length: one actuator at the centre and two actuators symmetrically placed on either side of the centre of gravity. This arrangement facilitates effective control of all vibration modes.

The control scheme successfully mitigates undesired motions of the suspended load caused by wave-induced crane excitations and initial conditions. Both planar and torsional motions stabilize at a steady state with minimal deviations from the desired position. Key factors influencing the control performance include the distance between interacting magnets and the tuning of PID controller gains, particularly the proportional gain, which is critically linked to the torsional actuator's effectiveness. Furthermore, the placement of the interaction points on the cylinder is crucial. While these points are constrained to the upper and lower towers (to generate a torque around the centre of mass), their exact positions significantly impact the magnitude of the required actuator force due to their effect on the arms of the resulting control torques.

In addition to attenuating motion, the two translational actuators compensate for the constant attracting force generated by the orientation of the torsional controller. The torsional control is less demanding in terms of force magnitude, as its main objective is to counteract the effects of the initial conditions. Since the crane tip motion does not directly excite the torsional vibrations, and the translational control remains effective, the coupling induced by magnetically-generated stiffness is not destabilising.

Regarding the resulting control forces, their magnitudes are of the same order as, yet lower than, the tension amplitudes typically required by conventional offshore tugger line control systems. Moreover, the direct control they introduce adds an additional level of controllability to the system. The maximum force values occur during the brief transient response phase, with the ratio of control force to the object's weight remaining low, peaking at approximately 15%.

This chapter concludes the proof-of-concept investigation of a contactless technique for controlling suspended loads through magnet-to-magnet interactions. The full-scale results further validate the effectiveness of this contactless motion control approach in efficiently managing the motion of the suspended component, thereby enabling a more precise and effective installation process.

8

Conclusions & Recommendations

As offshore wind turbines continue to increase in size to meet the ever-growing energy demands, heavy lift vessels with dynamic positioning capabilities are increasingly employed to install larger turbines in deeper waters. However, the success of these floating installations is often compromised by harsh offshore conditions, which result in undesired wave-induced motions of the crane-payload system. Thus, effective control of suspended loads is crucial for ensuring operational safety and installation efficiency.

Current motion compensation methods, such as active tugger lines, gripper frames, and crane motion compensators, typically rely on indirect control methods, mechanical attachments and human intervention. Due to the tight installation tolerances and the limited workability windows offshore, there exists a notable opportunity for further investigation into motion control methods, with non-contact techniques offering a promising area of research beyond the conventional approaches employed in the industry. The proposed method in this thesis leverages magnet-to-magnet interactions between the suspended component and an arrangement of electromagnetic actuators, utilizing both attractive and repulsive forces to achieve robust and reliable motion control.

8.1. Conclusions

The present thesis examined this contactless technique by investigating a set of dynamic system analogues through both experimental and numerical approaches, thereby providing a proof-of-concept for the proposed method.

Chapter 2 outlined the theoretical foundations of the methodologies used in the thesis. A review of the state-of-the-art in magnetically excited and controlled pendula, highlighted the potential of the use of magnet-to-magnet interactions to enhance motion controllability. A simplified crane-load analogue is then introduced, capturing the essential dynamics of the system. To simulate magnetic interactions, each magnet is modelled as a magnetic dipole.

Leveraging these foundations, in Chapter 3, an experimental setup and a mathematical model are developed to validate the contactless motion control concept. The external forces acting on the pendulum were identified and calibrated against physical experimental data. The damping force was represented by Coulomb's friction, while the magnet interaction followed an empirical nonlinear relationship with distance, consistent with an elementary dipole-to-dipole model. To validate the numerical model, forced vibrations were applied using an electromagnetic actuator with varying frequencies and amplitudes. The model successfully captured the system's dynamic behaviour, with minor discrepancies attributed to two primary nonlinearities: the friction force, which is influenced by memory effects and the physical experiment's conditions, and the operational constraints of the electromagnetic actuator, such as delays in polarity switching due to the magnetization of the magnet core.

With the model accurately calibrated and the interaction between magnets quantified, Chapter 4 explored the controlled response of the system, examining the control technique's limitations and influential parameters in greater detail. A modified PD controller regulated the motion by dynamically adjusting the intensity and polarity of an electromagnet. The technique was effective in two control modes: maintaining a desired motion with a fixed pivot and stabilizing a fixed global position with a moving pivot (disturbance rejection). Two key control parameters were identified: the saturation of the electromagnetic actuator and the separation distance between the magnets. Faster polarity transitions reduced the electromagnet's operational capacity, leading to poorer responses, while a smaller separation distance significantly improved control performance with lower errors and reduced saturation. These findings highlight the importance of setting upper and lower bounds for the separation distance to prevent saturation and control failure due to magnetic impact.

Analytical controllability curves were derived to optimize the magnet separation distance for various excitation conditions. Resonance behaviour was leveraged in the desired motion but was effectively suppressed in the disturbance rejection control mode. The transient response in the latter mode proved critical, as large errors and high saturation levels occurred until steady-state was reached, necessitating constraints on acceptable transient errors. Power considerations also influenced the optimal magnet separation choice, with mechanical actuation power favouring intermediate distances and electrical power suggesting smaller separations as more energy-efficient. The force amplitudes were on par with conventional tugger line control systems, but the ability to use both repulsive and attractive forces offered greater control.

Chapter 5 addressed another significant vibration mode, the torsional rotation around the shaft of the component, prevalent during the mating installation stage of OWT components, where aligning the pieces properly introduces challenges to the duration of the overall installation. A proof-of-concept for a contactless rotation control for cylindrical structures is developed. The proposed controller leverages magnetic interactions between a mounted permanent magnet and an electromagnetic actuator, but this time, the orientation of its magnetic field was the main control variable.

The control strategy, while based on linearised system analysis, proved effective in managing the full nonlinear system through numerical simulations. Three control modes were explored: the first attenuates rotation by generating a dissipative torque through a magnetically induced term resembling Coulomb friction; the second sets a new stable equilibrium position; and the third actively imposes a time-varying torsional vibration. Control performance depends on factors such as the magnet separation distance, the dipole orientation change, and the interplay between magnetic and spring stiffness.

The combined control of torsional and translational vibrations is investigated in Chapter 6, exploring the challenges and interactions between these degrees of freedom in a suspended point mass pendulum, integrating the separate control strategies developed in previous chapters. These degrees of freedom are coupled via the system's magnetically induced stiffness. Magnetic interactions of both controllers thus influence the equilibrium positions.

The performance and controllability of the combined control approach were evaluated under two scenarios: disturbance rejection for both translational and torsional motions, and desired motion control for translation combined with damping control for torsion. In both cases, the controllers effectively reduce vibrations, with translational control achieving a quick transition into the steady-state regime. The stability and success of the combined control method are primarily attributed to the translational actuator's ability to precisely control the separation distance of the torsional dipoles—a crucial factor for efficient torsional control. However, the controllability range for torsional vibrations in the combined system is narrower and time-dependent compared to stand-alone torsional control, studied in Chapter 5.

Chapter 7 presented a full-scale numerical model for controlling a suspended OWT tower from a floating crane, validated by analysing an offshore lifting phase. The proposed control scheme uses three actuators: one for torsional control and two for translational control, positioned along the cylinder's height. The method successfully mitigates undesired motions caused by crane excitation and initial conditions, stabilizing both planar and torsional rotations with minimal deviations. Apart from the separation distance of the interacting magnetic dipoles, other key performance factors include the PID controller tuning and the placement of actuators. The magnetically induced control forces are comparable to, or lower than, the conventional offshore tugger line forces while offering enhanced controllability of different vibrational modes.

Concluding this thesis and upon presenting a proof-of-concept analysis, the contactless technique proposed demonstrates effective motion control through magnet-to-magnet interactions, thus potentially enabling more precise, safe and efficient offshore installations.

8.2. Recommendations & Future outlook

In view of the findings presented in this study, the following recommendations and areas for future investigation are proposed to advance the development and application of the contactless motion control technique:

- **Magnetization Interference:**
  While this thesis does not consider the payload as ferromagnetic, the effects of the presence of ferromagnetic material around the mounted magnets should be investigated. Understanding the interference caused by the magnetization of such materials is crucial. Additionally, the feasibility of employing the contactless attractive forces on a ferromagnetic pendulum mass, without the use of a permanent magnet, should be studied as an alternative approach, akin to the tension applied by active tugger lines.
- **Advanced Control Strategies:**
  Further research should focus on developing and testing more advanced control algorithms for regulating magnetic parameters, including polarity, strength, and field orientation. A systematic study of time-varying separation distances, dynamically adjusted to optimize control performance and minimize power consumption, could also yield significant improvements in efficiency and reliability.
- **Optimization of the Control Arrangement:**
  Expanding the study to the full 3D problem is essential to comprehensively understand the system's dynamics and optimize the actuator configurations. Minimizing the number of required magnetic actuators while maintaining a satisfactory level of performance is an important goal. For instance, the attractive forces generated by the torsional controller could potentially be repurposed to induce the desired torque around the centre of mass, simplifying the actuator design.
- **Environmental Loads and Installation Phases:**
  The effects of environmental loads, such as wave and current action, and wind-induced vibrations (e.g., vortex-induced vibrations), should be incorporated into future studies. These factors are particularly critical during different installation phases, such as free suspension, semi-submersion, and penetration stages for bottom-founded installations. Additionally, a contactless alternative to gripper frames should be explored to mitigate impact-induced defects on the structure during installations under rough sea conditions.
- **Holistic Crane-Vessel Interaction Simulations:**
  A holistic simulation integrating the crane-payload system, controllers, and a float-

ing vessel should be conducted. This would allow for a detailed investigation of the coupling effects between dynamic positioning system and crane-payload controlled motions. Moreover, the potential for heave parametric resonance should be assessed to determine whether it is adequately mitigated by existing crane heave compensation systems.

- **Contactless Motion Control Experimental Campaign:**
  Conducting physical experiments of the contactless technique with a suspended distributed mass on a floating crane mechanical analogue (e.g. tower crane mounted on hexapod base) at lab- and meso-scales could provide valuable insights for further refining the control schemes. Additionally, integrating spatial actuators (robotic arms or drones) to maintain the desired separation distance during operation would improve the controllability of the system, addressing both fine and coarse control requirements.

By addressing these areas, future studies can further advance the contactless motion control technique and enhance its practical application, particularly for challenging offshore operations like the installation of large wind turbines (Figure 8.1).

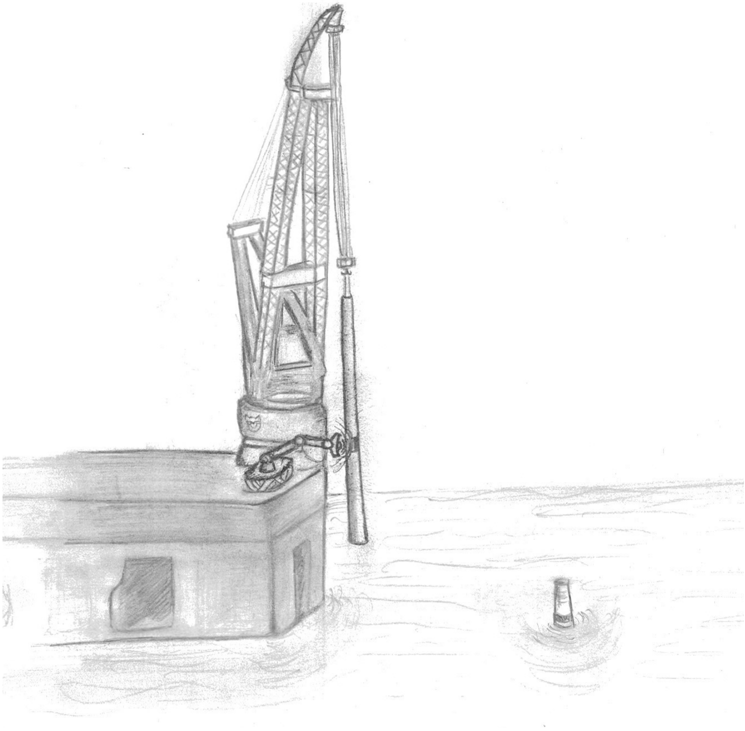

Figure 8.1: Floating vessel OWT installation with contactless motion control.

Bibliography

References for Chapter 1

[1] U. Shahzad, “The need for renewable energy sources,” *International Journal of Information Technology and Electrical Engineering*, vol. 2, pp. 16–18, 2012.

[2] D. Hartley and D. Schueler, “Perspectives on renewable energy and the environment,” *Energy and the Environment in the 21st Century*, 1990.

[3] I. Dincer, “Renewable energy and sustainable development: A crucial review,” *Renewable and sustainable energy reviews*, vol. 4, no. 2, pp. 157–175, 2000.

[4] O. Demirtas, “Evaluating the best renewable energy technology for sustainable energy planning,” *International Journal of Energy Economics and Policy*, vol. 3, no. 4, pp. 23–33, 2013.

[5] J. Zhao, A. K. Patwary, A. Qayyum, M. Alharthi, F. Bashir, M. Mohsin, I. Hanif, and Q. Abbas, “The determinants of renewable energy sources for the fueling of green and sustainable economy,” *Energy*, vol. 238, p. 122 029, Jan. 2022, ISSN: 0360-5442.

[6] S.-P. Breton and G. Moe, “Status, plans and technologies for offshore wind turbines in europe and north america,” *Renewable energy*, vol. 34, no. 3, pp. 646–654, 2009.

[7] M. Bilgili, A. Yasar, and E. Simsek, “Offshore wind power development in europe and its comparison with onshore counterpart,” *Renewable and Sustainable Energy Reviews*, vol. 15, no. 2, pp. 905–915, 2011.

[8] “Offshore wind outlook 2019: World energy outlook special report,” *International Energy Agency*, 2019. [Online]. Available: `https://www.iea.org/reports/offshore-wind-outlook-2019`.

[9] H. Díaz and C. G. Soares, “Review of the current status, technology and future trends of offshore wind farms,” *Ocean Engineering*, vol. 209, p. 107 381, 2020.

[10] L. Riefolo, C. Lanfredi, A. Azzellino, G. R. Tomasicchio, D. Felice, V. Penchev, and D. Vicinanza, “Offshore wind turbines: An overview of the effects on the marine environment,” in *ISOPE International Ocean and Polar Engineering Conference*, ISOPE, 2016.

[11] H. Bailey, K. L. Brookes, and P. M. Thompson, “Assessing environmental impacts of offshore wind farms: Lessons learned and recommendations for the future,” *Aquatic biosystems*, vol. 10, pp. 1–13, 2014.

[12] B. Snyder and M. J. Kaiser, “Ecological and economic cost-benefit analysis of offshore wind energy,” *Renewable energy*, vol. 34, no. 6, pp. 1567–1578, 2009.

[13] A. Tsetas, E. Kementzetzidis, S. Gómez, T. Molenkamp, A. Elkadi, F. Pisanò, A. Tsouvalas, and A. Metrikine, “Gentle driving of piles: Field observations, quantitative analysis and further development,” in *Offshore Technology Conference*, OTC, 2024, D021S019R001.

[14] Y. Peng, A. Tsouvalas, T. Stampoultzoglou, and A. Metrikine, “Study of the sound escape with the use of an air bubble curtain in offshore pile driving,” *Journal of Marine Science and Engineering*, vol. 9, no. 2, p. 232, 2021.

[15] Z. L. Hutchison, A. B. Gill, P. Sigray, H. He, and J. W. King, “A modelling evaluation of electromagnetic fields emitted by buried subsea power cables and encountered by marine animals: Considerations for marine renewable energy development,” *Renewable Energy*, vol. 177, pp. 72–81, 2021.

[16] U. N. C. C. C. (COP21), *The paris agreement*, 2015. [Online]. Available: `https://unfccc.int/process-and-meetings/the-paris-agreement`.

[17] European Commission, *European green deal - consilium*, 2020. [Online]. Available: `https://www.consilium.europa.eu/en/policies/green-deal/`.

[18] Wind Europe, *Wind energy in europe: 2021 statistics and the outlook for 2022-2026*. [Online]. Available: `https://windeurope.org/intelligence-platform/product/wind-energy-in-europe-2021-statistics-and-the-outlook-for-2022-2026/`.

[19] P. Chen, T. Grünewald, J. Noffsinger, and E. Samseth, *Global energy perspective 2023: Power outlook*, 2024. [Online]. Available: `https://www.mckinsey.com/industries/oil-and-gas/our-insights/global-energy-perspective-2023-power-outlook`.

[20] E. Barlow, D. Tezcaner Ozturk, S. Day, E. Boulougouris, M. Revie, and K. Akartunali, “An assessment of vessel characteristics for the installation of offshore wind farms,” *ICMT 2014*, 2014.

[21] Van Oord, *Van oord orders mega ship to install 20 mw offshore wind foundations and turbines*. [Online]. Available: `https://www.vanoord.com/en/updates/van-oord-orders-mega-ship/`.

[22] Y. Guo, H. Wang, and J. Lian, “Review of integrated installation technologies for offshore wind turbines: Current progress and future development trends,” *Energy Conversion and Management*, vol. 255, p. 115 319, Mar. 2022, ISSN: 0196-8904.

[23] M. J. Kaiser and B. Snyder, “Offshore wind energy installation and decommissioning cost estimation in the us outer continental shelf,” *US Dept. of the Interior, Bureau of Ocean Energy Management, Regulation and Enforcement, Herndon, VA TA&R*, vol. 648, 2010.

[24] R. Lacal-Arántegui, J. M. Yusta, and J. A. Domínguez-Navarro, "Offshore wind installation: Analysing the evidence behind improvements in installation time," *Renewable and Sustainable Energy Reviews*, vol. 92, pp. 133–145, Sep. 2018, ISSN: 1364-0321.

[25] Westwood and Douglas, "Assessment of vessel requirements for the us offshore wind sector," *U.S. Offshore Wind: Removing Market Barriers*, 2013.

[26] Y. Dalgic, I. Lazakis, O. Turan, and S. Judah, "Investigation of optimum jack-up vessel chartering strategy for offshore wind farm o&m activities," *Ocean Engineering*, vol. 95, pp. 106–115, 2015.

[27] M. Stålhane, M. Christiansen, O. Kirkeby, and A. J. Mikkelsen, "Optimizing jack-up vessel strategies for maintaining offshore wind farms," *Energy Procedia*, vol. 137, pp. 291–298, 2017.

[28] E. Uraz, *Offshore wind turbine transportation & installation analyses planning optimal marine operations for offshore wind projects*, 2011.

[29] Y. Zhao, Z. Cheng, Z. Gao, P. C. Sandvik, and T. Moan, "Numerical study on the feasibility of offshore single blade installation by floating crane vessels," *Marine Structures*, vol. 64, pp. 442–462, 2019.

[30] K. Ellermann, E. Kreuzer, and M. Markiewicz, "Nonlinear dynamics of floating cranes," *Nonlinear dynamics*, vol. 27, pp. 107–183, 2002.

[31] Z. Gao, A. Verma, Y. Zhao, Z. Jiang, and Z. Ren, "A summary of the recent work at ntnu on marine operations related to installation of offshore wind turbines," in *International Conference on Offshore Mechanics and Arctic Engineering*, American Society of Mechanical Engineers, vol. 51326, 2018, V11AT12A044.

[32] C. van Lynden, I. van Winsen, C. Westland, and A. Kana, "Offshore wind installation vessels: Generating insight about the driving factors behind the future design," *International Journal of Maritime Engineering*, vol. 164, no. A2, pp. 221–236, 2022.

[33] Z. Jiang, "Installation of offshore wind turbines: A technical review," *Renewable and Sustainable Energy Reviews*, vol. 139, p. 110 576, Apr. 2021, ISSN: 1364-0321.

[34] W. Sonnema, "3d fe analysis of four legged jack-up vessels during preloading in cohesive soil," 2019.

[35] J. Ye, S. Roy, M. Godjevac, V. Reppa, and S. Baldi, "Robustifying dynamic positioning of crane vessels for heavy lifting operation," *IEEE/CAA Journal of Automatica Sinica*, vol. 8, pp. 753–765, 4 Apr. 2021, ISSN: 23299274.

[36] H. Faÿ, *Dynamic Positioning Systems: Principles, Design, and Applications*. Editions OPHRYS, 1990.

[37] N. Ku and M.-I. Roh, “Dynamic response simulation of an offshore wind turbine suspended by a floating crane,” *Ships and Offshore Structures*, vol. 10, no. 6, pp. 621–634, 2015, ISSN: 1744-5302.

[38] J.-H. Cha, M.-I. Roh, and K.-Y. Lee, “Dynamic response simulation of a heavy cargo suspended by a floating crane based on multibody system dynamics,” *Ocean Engineering*, vol. 37, no. 14-15, pp. 1273–1291, 2010.

[39] Z. Ren, A. S. Verma, B. Ataei, K. H. Halse, and H. P. Hildre, “Model-free anti-swing control of complex-shaped payload with offshore floating cranes and a large number of lift wires,” *Ocean Engineering*, vol. 228, p. 108 868, May 2021, ISSN: 0029-8018.

[40] F. Liu, J. Yang, J. Wang, and C. Liu, “Swing characteristics and vibration feature of tower cranes under compound working condition,” *Shock and Vibration*, vol. 2021, no. 1, p. 8 997 396, 2021.

[41] A. Brkic, S. Tošic, D. Ostric, and N. Zrnic, “Influence of load swinging to the dynamic behaviour of tower crane,” in *TEHNO’98: Proceedings of the Conference of Manufacturing Engineering,, Timisoara, Romania*, 1998, pp. 581–588.

[42] Van Oord, *Van oord voltooit installatie gemini offshore windpark*. [Online]. Available: `https://www.vanoord.com/nl/updates/van-oord-voltooit-installatie-gemini-offshore-windpark/`.

[43] DOB-Academy, *Fox project video - offshore campaign*, `https://www.youtube.com/watch?v=BGcLoREJI-c`, 2022.

[44] D. Domingos, P. Wellens, and van Wingerden, J.W., “Prometheus: An open-source SSCV,” *4TU.ResearchData*, 2023.

[45] Z. Ren, Z. Jiang, Z. Gao, and R. Skjetne, “Active tugger line force control for single blade installation,” *Wind Energy*, vol. 21, pp. 1344–1358, 12 Dec. 2018, ISSN: 10991824.

[46] S. Wang, Y. Sun, H. Chen, and J. Du, “Dynamic modelling and analysis of 3-axis motion compensated offshore cranes,” *Ships and Offshore Structures*, vol. 13, no. 3, pp. 265–272, 2018, ISSN: 17445302.

[47] W. O’Connor and H. Habibi, “Gantry crane control of a double-pendulum, distributed-mass load, using mechanical wave concepts,” *Mechanical Sciences*, vol. 4, pp. 251–261, 2 2013, ISSN: 2191916X.

[48] D. H. Lee, T. W. Kim, S. W. Ji, and Y. B. Kim, “A study on load position control and vibration attenuation in crane operation using sub-actuator,” *Measurement and Control*, vol. 52, pp. 794–803, 7-8 Sep. 2019, ISSN: 00202940.

[49] M. Richter, S. Schaut, D. Walser, K. Schneider, and O. Sawodny, “Experimental validation of an active heave compensation system: Estimation, prediction and control,” *Control Engineering Practice*, vol. 66, pp. 1–12, 2017.

[50] N. Xianliang, Z. Jiawen, and X. Jianan, “The heave motion estimation for active heave compensation system in offshore crane,” in *2016 IEEE International Conference on Mechatronics and Automation*, IEEE, 2016, pp. 1327–1332.

[51] J. Hatleskog and M. Dunnigan, “Heave compensation simulation for non-contact operations in deep water,” in *OCEANS 2006*, IEEE, 2006, pp. 1–6.

[52] J. Woodacre, R. Bauer, and R. Irani, “A review of vertical motion heave compensation systems,” *Ocean Engineering*, vol. 104, pp. 140–154, 2015.

[53] J. Neupert, T. Mahl, B. Haessig, O. Sawodny, and K. Schneider, “A heave compensation approach for offshore cranes,” *Proceedings of the American Control Conference*, pp. 538–543, 2008, ISSN: 07431619.

[54] N.-B. Le, B.-G. Kim, and Y.-B. Kim, “Heave compensation system design for offshore crane based on input-output linearization,” *Journal of Power System Engineering*, vol. 21, no. 2, pp. 27–34, 2017.

[55] *Gripper system supports installation of offshore taiwan wind farm monopiles | offshore*, 2022. [Online]. Available: `https://www.offshore-mag.com/regional-reports/asia/article/14270857/gripper-system-supports-installation-of-offshore-taiwan-wind-farm-monopiles`.

[56] *Dot6000-floating installation offshore xxl wind turbines - topsector energie*. [Online]. Available: `https://projecten.topsectorenergie.nl/projecten/dot6000-floating-installation-offshore-xxl-wind-turbines-33169`.

[57] *This is what makes the cranes of the sleipnir special | swz|maritime*. [Online]. Available: `https://swzmaritime.nl/news/2020/04/02/this-is-what-makes-the-cranes-of-the-sleipnir-special/`.

References for Chapter 2

[37] N. Ku and M.-I. Roh, “Dynamic response simulation of an offshore wind turbine suspended by a floating crane,” *Ships and Offshore Structures*, vol. 10, no. 6, pp. 621–634, 2015, ISSN: 1744-5302.

[38] J.-H. Cha, M.-I. Roh, and K.-Y. Lee, “Dynamic response simulation of a heavy cargo suspended by a floating crane based on multibody system dynamics,” *Ocean Engineering*, vol. 37, no. 14-15, pp. 1273–1291, 2010.

[58] Y. Kraftmakher, “Experiments with a magnetically controlled pendulum,” *European journal of physics*, vol. 28, no. 5, p. 1007, 2007.

[59] L. B. Zhang, A. Abdelkefi, H. L. Dai, R. Naseer, and L. Wang, “Design and experimental analysis of broadband energy harvesting from vortex-induced vibrations,” *Journal of Sound and Vibration*, vol. 408, pp. 210–219, Nov. 2017, ISSN: 0022-460X.

[60] T. G. Larsen, Z. Zhang, and J. Høgsberg, “Vibration damping of an offshore wind turbine by optimally calibrated pendulum absorber with shunted electromagnetic transducer,” *Journal of Sound and Vibration*, vol. 505, p. 116 144, 2021.

[61] V. N. Pilipchuk, K. Polczyński, M. Bednarek, and J. Awrejcewicz, “Guidance of the resonance energy flow in the mechanism of coupled magnetic pendulums,” *Mechanism and Machine Theory*, vol. 176, p. 105 019, 2022.

[62] A. N. Kadjie and P. Woafo, “Effects of springs on a pendulum electromechanical energy harvester,” *Theoretical and Applied Mechanics Letters*, vol. 4, p. 063 001, 6 Jan. 2014, ISSN: 2095-0349.

[63] R. Kumar, S. Gupta, and S. F. Ali, “Energy harvesting from chaos in base excited double pendulum,” *Mechanical Systems and Signal Processing*, vol. 124, pp. 49–64, Jun. 2019, ISSN: 0888-3270.

[64] B. Mann, “Energy criterion for potential well escapes in a bistable magnetic pendulum,” *Journal of Sound and Vibration*, vol. 323, no. 3-5, pp. 864–876, 2009.

[65] M. Wojna, A. Wijata, G. Wasilewski, and J. Awrejcewicz, “Numerical and experimental study of a double physical pendulum with magnetic interaction,” *Journal of Sound and Vibration*, vol. 430, pp. 214–230, Sep. 2018, ISSN: 0022-460X.

[66] A. Wijata, K. Polczyński, and J. Awrejcewicz, “Theoretical and numerical analysis of regular one-side oscillations in a single pendulum system driven by a magnetic field,” *Mechanical Systems and Signal Processing*, vol. 150, p. 107 229, Mar. 2021, ISSN: 0888-3270.

[67] S. Skurativskyi, K. Polczyński, M. Wojna, and J. Awrejcewicz, “Quantifying periodic, multi-periodic, hidden and unstable regimes of a magnetic pendulum via semi-analytical, numerical and experimental methods,” *Journal of Sound and Vibration*, vol. 524, p. 116 710, 2022.

[68] A. Siahmakoun, V. A. French, and J. Patterson, “Nonlinear dynamics of a sinusoidally driven pendulum in a repulsive magnetic field,” *American Journal of Physics*, vol. 65, p. 393, 5 Jun. 1998, ISSN: 0002-9505. [Online]. Available: `https://aapt.scitation.org/doi/abs/10.1119/1.18546`.

[69] K. R. Austin and J. R. Wagner, “Development of an electromagnet excited mass-pendulum system modeling and control laboratory experiment - theory and test,” *2013 European Control Conference, ECC 2013*, pp. 256–261, 2013.

[70] N. Ida, “Design and control of a magnetic pendulum actuator,” *Proceedings of the International Conference on Optimisation of Electrical and Electronic Equipment, OPTIM*, pp. 439–443, 2012, ISSN: 18420133.

[71] A. Fradkov, B. Andrievsky, and K. Boykov, “Control of the coupled double pendulums system,” *Mechatronics*, vol. 15, no. 10, pp. 1289–1303, 2005.

[72] Y. Kraftmakher, "Demonstrations with a magnetically controlled pendulum," *American Journal of Physics*, vol. 78, p. 532, 5 Apr. 2010, ISSN: 0002-9505. [Online]. Available: `https://aapt.scitation.org/doi/abs/10.1119/1.3276412`.

[73] E. M. Abdel-Rahman, A. H. Nayfeh, and Z. N. Masoud, "Dynamics and control of cranes: A review," *Journal of Vibration and control*, vol. 9, no. 7, pp. 863–908, 2003.

[74] R. Campa, I. Soto, and O. Martínez, "Modelling and control of a spherical pendulum via a non–minimal state representation," *Mathematical and Computer Modelling of Dynamical Systems*, vol. 27, no. 1, pp. 3–30, 2021.

[75] V. Jivkov and R. Mitrev, "Motion analysis of a spherical pendulum with a movable pivot," in *AIP Conference Proceedings*, AIP Publishing, vol. 3064, 2024.

[76] A. Weinstein, "The spherical pendulum and complex integration," *The American Mathematical Monthly*, vol. 49, no. 8, pp. 521–523, 1942.

[77] H. Essén and N. Apazidis, "Turning points of the spherical pendulum and the golden ratio," *European journal of physics*, vol. 30, no. 2, p. 427, 2009.

[78] P. Cumber, "There is more than one way to force a pendulum," *International Journal of Mathematical Education in Science and Technology*, vol. 54, no. 4, pp. 579–613, 2023.

[79] S. Nedelcu and J. Watson, "Magnetic dipole model of a permanent magnet based device," *Journal of Physics D: Applied Physics*, vol. 34, no. 17, p. 2622, 2001.

[80] A. J. Petruska and J. J. Abbott, "Optimal permanent-magnet geometries for dipole field approximation," *IEEE transactions on magnetics*, vol. 49, no. 2, pp. 811–819, 2012.

[81] T. H. Boyer *et al.*, "The force on a magnetic dipole," *American Journal of Physics*, vol. 56, no. 8, pp. 688–692, 1988.

[82] R. P. Borase, D. Maghade, S. Sondkar, and S. Pawar, "A review of pid control, tuning methods and applications," *International Journal of Dynamics and Control*, vol. 9, pp. 818–827, 2021.

[83] K. J. Åström and R. M. Murray, *Feedback Systems: An Introduction for Scientists and Engineers*. 2008. [Online]. Available: `https://www.researchgate.net/publication/36721090_Feedback_Systems_An_Introduction_for_Scientists_and_Engineers`.

[84] K. H. Ang, G. Chong, and Y. Li, "Pid control system analysis, design, and technology," *IEEE transactions on control systems technology*, vol. 13, no. 4, pp. 559–576, 2005.

[85] I. D. Díaz-Rodríguez, S. Han, and S. P. Bhattacharyya, *Analytical design of PID controllers*. Springer, 2019.

[86] K. J. Åström and T. Hägglund, *PID Controllers: Theory, Design, and Tuning*. 1995.

[87] Y.-C. Tian, M. O. Tadé, and J. Tang, "A nonlinear pid controller with applications," *IFAC Proceedings Volumes*, vol. 32, no. 2, pp. 2657–2661, 1999.

[88] H. K. Khalil, *Nonlinear Systems*, en, 3rd ed. Upper Saddle River, NJ: Pearson, Dec. 2001.

References for Chapter 3

[89] P. Atzampou, P. C. Meijers, A. Tsouvalas, and A. V. Metrikine, "Contactless control of suspended loads for offshore installations: Proof of concept using magnetic interaction," *Journal of Sound and Vibration*, vol. 575, p. 118 246, 2024.

[90] G. Torzo and P. Peranzoni, "The real pendulum: Theory, simulation, experiment," *Lat. Am. J. Phys. Educ. Vol*, Jan. 2009. [Online]. Available: `https://www.academia.edu/835053/The_real_pendulum_theory_simulation_experiment`.

[91] A. Cabboi and J. Woodhouse, "Validation of a constitutive law for friction-induced vibration under different wear conditions," *Wear*, vol. 396-397, pp. 107–125, Feb. 2018, ISSN: 0043-1648.

[92] D. J. Griffiths, *Introduction to Electrodynamics, The Science of Microfabrication*. Cambridge University Press, 2017, ISBN: 9781108333511.

[93] M. S. Sarma, *Introduction to electrical engineering*. Oxford University Press, 2001.

[94] G. L. Baker, "Probability, pendulums, and pedagogy," *American journal of physics*, vol. 74, no. 6, pp. 482–489, 2006.

References for Chapter 4

[44] D. Domingos, P. Wellens, and van Wingerden, J.W., "Prometheus: An open-source SSCV," *4TU.ResearchData*, 2023.

[45] Z. Ren, Z. Jiang, Z. Gao, and R. Skjetne, "Active tugger line force control for single blade installation," *Wind Energy*, vol. 21, pp. 1344–1358, 12 Dec. 2018, ISSN: 10991824.

[89] P. Atzampou, P. C. Meijers, A. Tsouvalas, and A. V. Metrikine, "Contactless control of suspended loads for offshore installations: Proof of concept using magnetic interaction," *Journal of Sound and Vibration*, vol. 575, p. 118 246, 2024.

[95] J. Dormand and P. Prince, "Practical runge–kutta processes," *SIAM Journal on Scientific and Statistical Computing*, vol. 10, no. 5, pp. 977–989, 1989.

[96] P. Atzampou, P. Meijers, A. Tsouvalas, and A. Metrikine, "Motion control of a pendulum via magnetic interaction," in *International Conference on Nonlinear Dynamics and Applications*, Springer, 2023, pp. 49–59.

[97] T. Chai and R. R. Draxler, "Root mean square error (rmse) or mean absolute error (mae)," *Geoscientific model development discussions*, vol. 7, no. 1, pp. 1525–1534, 2014.

[98] V. Negro, J.-S. López-Gutiérrez, M. D. Esteban, P. Alberdi, M. Imaz, and J.-M. Serraclara, "Monopiles in offshore wind: Preliminary estimate of main dimensions," *Ocean Engineering*, vol. 133, pp. 253–261, 2017.

[99] L. Wan, Z. Gao, and T. Moan, "Model test of the stc concept in survival modes," in *International Conference on Offshore Mechanics and Arctic Engineering*, American Society of Mechanical Engineers, vol. 45530, 2014, V09AT09A010.

References for Chapter 5

[90] G. Torzo and P. Peranzoni, "The real pendulum: Theory, simulation, experiment," *Lat. Am. J. Phys. Educ. Vol*, Jan. 2009. [Online]. Available: `https://www.academia.edu/835053/The_real_pendulum_theory_simulation_experiment`.

[100] P. Atzampou, P. C. Meijers, A. Tsouvalas, and A. V. Metrikine, "Non-contact electromagnetic control of torsional vibrations of a rigid cylinder," *Nonlinear Dynamics*, vol. 113, no. 3, pp. 2001–2016, 2025.

[101] A. Mehmanparast, S. Lotfian, and S. P. Vipin, "A review of challenges and opportunities associated with bolted flange connections in the offshore wind industry," *Metals*, vol. 10, no. 6, p. 732, 2020.

[102] P. Allaire, M. Kasarda, R. Humphris, and D. Lewis, "Vibration reduction in a multimass flexible rotor using a midspan magnetic damper," *Magnetic Bearings: Proceedings of the First International Symposium*, pp. 149–158, 1988.

[103] A. Filatov, L. Hawkins, and P. McMullen, "Homopolar permanent-magnet-biased actuators and their application in rotational active magnetic bearing systems," *Actuators*, vol. 5, p. 26, 2016.

[104] T. Du, H. Geng, B. Wang, H. Lin, and L. Yu, "Nonlinear oscillation of active magnetic bearing–rotor systems with a time-delayed proportional–derivative controller," *Nonlinear Dynamics*, vol. 109, no. 4, pp. 2499–2523, 2022.

[105] N. Saeed and A. Kandil, "Lateral vibration control and stabilization of the quasiperiodic oscillations for rotor-active magnetic bearings system," *Nonlinear dynamics*, vol. 98, no. 2, pp. 1191–1218, 2019.

[106] W. S. Takam, A. M. Kongne, and D. Yemélé, "Nonlinear dynamics of two dimensional rotor-active magnetic bearing system with generalized-pole legs: Stability state diagram and control strategy," *Nonlinear Dynamics*, vol. 111, no. 19, pp. 17 909–17 937, 2023.

[107] A. S. Puttewar, N. U. Kakde, H. A. Fidvi, and B. Nandeshwar, "Enhancement of braking system in automobile using electromagnetic braking," *IOSR Journal of Mechanical and Civil Engineering*, vol. 11, pp. 54–59, 2014.

[108] F.-M. Ou, Y.-C. Wu, and C.-F. Wu, "Conceptual design and analysis of a novel magnetic braking descent device," *IFToMM World Congress on Mechanism and Machine Science*, pp. 269–278, 2023.

[109] M. Jou, J.-K. Shiau, and C.-C. Sun, "Design of a magnetic braking system," *Journal of Magnetism and Magnetic Materials*, vol. 304, Sep. 2006.

[110] E. Galardi, E. Meli, D. Nocciolini, L. Pugi, and A. Rindi, “Development of efficient models of magnetic braking systems of railway vehicles,” *International Journal of Rail Transportation*, vol. 3, no. 2, pp. 97–118, 2015.

[111] H. Zhang, Z. Chen, X. Hua, Z. Huang, and H. Niu, “Design and dynamic characterization of a large-scale eddy current damper with enhanced performance for vibration control,” *Mechanical Systems and Signal Processing*, vol. 145, p. 106 879, 2020.

[112] F. Mazza and R. Labernarda, “Magnetic damped links to reduce internal seismic pounding in base-isolated buildings,” *Bulletin of Earthquake Engineering*, vol. 18, no. 15, pp. 6795–6824, 2020.

[113] H. Sakuma, “Three-dimensional motion control of an untethered magnetic object using three rotating permanent magnets,” *Scientific Reports*, vol. 13, no. 1, p. 18 052, 2023.

[114] Y. Shao, A. Fahmy, M. Li, C. Li, W. Zhao, and J. Sienz, “Study on magnetic control systems of micro-robots,” *Frontiers in Neuroscience*, vol. 15, p. 736 730, 2021.

[115] A. Ranzoni, X. J. Janssen, M. Ovsyanko, L. J. van IJzendoorn, and M. W. Prins, “Magnetically controlled rotation and torque of uniaxial microactuators for lab-on-a-chip applications,” *Lab on a Chip*, vol. 10, no. 2, pp. 179–188, 2010.

[116] A. W. Mahoney and J. J. Abbott, “5-dof manipulation of an untethered magnetic device in fluid using a single permanent magnet.,” *Robotics: Science and Systems*, 2014.

[117] E. Silani and M. Lovera, “Magnetic spacecraft attitude control: A survey and some new results,” *Control engineering practice*, vol. 13, no. 3, pp. 357–371, 2005.

[118] M. Y. Ovchinnikov and D. Roldugin, “A survey on active magnetic attitude control algorithms for small satellites,” *Progress in Aerospace Sciences*, vol. 109, p. 100 546, 2019.

[119] P. Ryan and E. Diller, “Magnetic actuation for full dexterity microrobotic control using rotating permanent magnets,” *IEEE Transactions on Robotics*, vol. 33, no. 6, pp. 1398–1409, 2017.

[120] T. Inamori, J. Wang, P. Saisutjarit, and S. Nakasuka, “Jitter reduction of a reaction wheel by management of angular momentum using magnetic torquers in nano- and micro-satellites,” *Advances in Space Research*, vol. 52, no. 1, pp. 222–231, 2013.

[121] A. Kanj, R. P. Thanalakshme, C. Li, J. Kulikowski, G. Bahl, and S. Tawfick, “Design, dynamics, and dissipation of a torsional-magnetic spring mechanism,” *Mechanical Systems and Signal Processing*, vol. 179, p. 109 307, 2022.

[122] P. Meijers, P. Atzampou, and A. Metrikine, “Experimental and numerical study of a magnetic pendulum,” *Third International Nonlinear Dynamics Conference - NODYCON2023*, 2023.

[123] P. Atzampou, P. C. Meijers, A. Tsouvalas, and A. V. Metrikine, “Contactless control of suspended loads for offshore installations: Proof of concept using magnetic interaction,” *Journal of Sound and Vibration*, p. 118 246, 2024.

[124] K. W. Yung, P. B. Landecker, and D. D. Villani, “An analytic solution for the force between two magnetic dipoles,” *Magnetic and electrical Separation*, vol. 9, 1970.

[125] P. B. Landecker, D. D. Villani, and K. W. Yung, “An analytic solution for the torque between two magnetic dipoles,” *Magnetic and Electrical Separation*, vol. 10, 1970.

[126] E. Sulollari, K. van Dalen, and A. Cabboi, “Vibration-induced friction modulation for a general frequency of excitation,” *Journal of Sound and Vibration*, vol. 573, p. 118 200, 2024.

[127] A. Tsetas, A. Tsouvalas, and A. V. Metrikine, “The mechanics of the gentle driving of piles,” *International Journal of Solids and Structures*, vol. 282, p. 112 466, 2023.

References for Chapter 6

[96] P. Atzampou, P. Meijers, A. Tsouvalas, and A. Metrikine, “Motion control of a pendulum via magnetic interaction,” in *International Conference on Nonlinear Dynamics and Applications*, Springer, 2023, pp. 49–59.

[128] P. Atzampou, P. C. Meijers, A. Tsouvalas, and A. V. Metrikine, “Motion control of suspended loads via magnetic interaction,” in *Nonlinear Systems - Practical Applications and Contemporary Challenges*, (soon to be published), IntechOpen, 2025.

[129] A. K. Chopra, *Dynamics of structures*. Pearson Education India, 2007.

[130] D. Omale, P. Ojih, and M. Ogwo, “Mathematical analysis of stiff and non-stiff initial value problems of ordinary differential equation using matlab,” *International journal of scientific & engineering research*, vol. 5, no. 9, pp. 49–59, 2014.

References for Chapter 7

[29] Y. Zhao, Z. Cheng, Z. Gao, P. C. Sandvik, and T. Moan, “Numerical study on the feasibility of offshore single blade installation by floating crane vessels,” *Marine Structures*, vol. 64, pp. 442–462, 2019.

[30] K. Ellermann, E. Kreuzer, and M. Markiewicz, “Nonlinear dynamics of floating cranes,” *Nonlinear dynamics*, vol. 27, pp. 107–183, 2002.

[37] N. Ku and M.-I. Roh, “Dynamic response simulation of an offshore wind turbine suspended by a floating crane,” *Ships and Offshore Structures*, vol. 10, no. 6, pp. 621–634, 2015, ISSN: 1744-5302.

[43] DOB-Academy, *Fox project video - offshore campaign*, `https://www.youtube.com/watch?v=BGcLoREJI-c`, 2022.

[44] D. Domingos, P. Wellens, and van Wingerden, J.W., “Prometheus: An open-source SSCV,” *4TU.ResearchData*, 2023.

[47] W. O’Connor and H. Habibi, “Gantry crane control of a double-pendulum, distributed-mass load, using mechanical wave concepts,” *Mechanical Sciences*, vol. 4, pp. 251–261, 2 2013, ISSN: 2191916X.

[129] A. K. Chopra, *Dynamics of structures*. Pearson Education India, 2007.

[131] Z. Ren, A. S. Verma, B. Ataei, K. H. Halse, and H. P. Hildre, “Model-free anti-swing control of complex-shaped payload with offshore floating cranes and a large number of lift wires,” *Ocean Engineering*, vol. 228, p. 108 868, 2021.

[132] Y. Zhao, Z. Cheng, P. C. Sandvik, Z. Gao, T. Moan, and E. Van Buren, “Numerical modeling and analysis of the dynamic motion response of an offshore wind turbine blade during installation by a jack-up crane vessel,” *Ocean Engineering*, vol. 165, pp. 353–364, 2018.

[133] B. J. de Kruif and B. Rossin, “Pendulation control for dynamical positioning capable ship; considerations on actuator usage,” *IFAC-PapersOnLine*, vol. 54, no. 16, pp. 120–125, 2021.

[134] Z. Li, X. Ma, and Y. Li, “Anti-swing control for a double-pendulum offshore boom crane with ship roll and heave movements,” in *2020 IEEE 16th International Conference on Control & Automation (ICCA)*, Ieee, 2020, pp. 165–170.

[135] A. S. Verma, N. P. Vedvik, and Z. Gao, “A comprehensive numerical investigation of the impact behaviour of an offshore wind turbine blade due to impact loads during installation,” *Ocean Engineering*, vol. 172, pp. 127–145, 2019.

[136] G. Meskers and R. van Dijk, “A damping tugger system for offshore heavy lifts,” in *International Conference on Offshore Mechanics and Arctic Engineering*, American Society of Mechanical Engineers, vol. 44885, 2012, pp. 315–323.

[137] L. Li, A. M. Amer, and X. Zhu, “Numerical analysis of an over-boarding operation for a subsea template,” *Journal of Ocean Engineering and Science*, vol. 6, no. 2, pp. 146–159, 2021.

[138] A. Cabboi, M. Segeren, H. Hendrikse, and A. Metrikine, “Vibration-assisted installation and decommissioning of a slip-joint,” *Engineering Structures*, vol. 209, p. 109 949, 2020, ISSN: 0141-0296.

[139] L. Larsson, “Ship resistance and flow,” *Published by The Society of Naval Architects and Marine Engineers, SNAME, The Principles of Naval Architecture Series, ISBN: 978-0-939773-76-3*, 2010.

[140] D. F. Domingos, P. Atzampou, P. C. Meijers, S. H. Beirão, A. V. Metrikine, J.-W. van Wingerden, and P. Wellens, “Full-scale measurements and analysis of the floating installation of an offshore wind turbine tower,” *Ocean Engineering*, vol. 310, p. 118 670, 2024.

[141] S. Al-Sanad, J. Parol, L. Wang, and A. Kolios, “Design optimisation of wind turbine towers with reliability-based calibration of partial safety factors,” *Energy Reports*, vol. 9, pp. 2548–2556, 2023.

[142] D. F. Domingos, P. Wellens, and J.-W. van Wingerden, “Frequency-domain framework for floating installation of wind-turbine towers,” *Ocean Engineering*, vol. 297, p. 116 952, 2024.

[143] Z. Ren, Z. Jiang, R. Skjetne, and Z. Gao, “Single blade installation using active control of three tugger lines,” in *ISOPE International Ocean and Polar Engineering Conference*, ISOPE, 2018, ISOPE–I.

[144] S. M. G. Andersen, “Motion control during offshore lift operations,” M.S. thesis, NTNU, 2017.

[145] B. Rossin, A. Sreenivasan, and B. De Kruif, “Coupled control for motion compensated offshore operations,” in *SNAME Offshore Symposium*, SNAME, 2022, D011S001R004.

[146] K. W. Yung, P. B. Landecker, and D. D. Villani, “An analytic solution for the force between two magnetic dipoles,” *Physical Separation in Science and Engineering*, vol. 9, no. 1, pp. 39–52, 1998.

A

Governing equations of a suspended OWT tower

The triple pendulum illustrated in Figure A1 has seven degrees of freedom (DOFs), corresponding to the various angles of the pendulum components in two planes, namely the *xz*- and *yz*-planes. These include the point mass pendulum angles, η_x and η_y, the sling angles, ζ_x and ζ_y, and the rotational angles of the cylinder around its top point, ψ_x and ψ_y, in the respective planes. The seventh DOF pertains to the torsional rotation ϕ around the cylinder's longitudinal axis.

The coordinates that describe the motion of the pendulum are given in terms of its three moving components as follows:

$$\vec{P}_h = \begin{bmatrix} \ell_h \sin(\eta_x) \\ \ell_h \cos(\eta_x)\sin(\eta_y) \\ \ell_h \cos(\eta_x)\cos(\eta_y) \end{bmatrix} + \begin{bmatrix} h_x \\ h_y \\ h_z \end{bmatrix}, \tag{A.1a}$$

$$\vec{P}_s = \begin{bmatrix} \ell_s \sin(\zeta_x) \\ \ell_s \cos(\zeta_x)\sin(\zeta_y) \\ \ell_s \cos(\zeta_x)\cos(\zeta_y) \end{bmatrix} + \vec{P}_h, \text{ and} \tag{A.1b}$$

$$\vec{P}_L = \begin{bmatrix} \frac{L}{2} \sin(\psi_x) \\ \frac{L}{2} \cos(\psi_x)\sin(\psi_y) \\ \frac{L}{2} \cos(\psi_x)\cos(\psi_y) \end{bmatrix} + \vec{P}_s, \tag{A.1c}$$

where $\vec{P}_L$, $\vec{P}_s$ and $\vec{P}_h$ are the position vectors of the hanging cylinder, the sling endpoint, and hook mass, respectively.

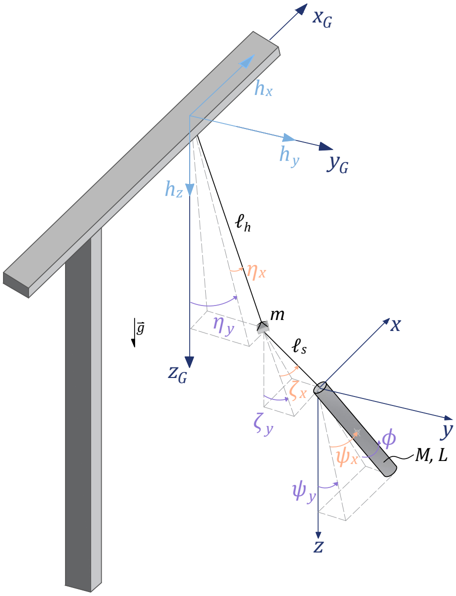

Figure A1: Schematic of the triple 3D pendulum of the crane-payload sub-system.

The kinetic $\mathcal{K}$ and potential $\mathcal{U}$ energy of the dynamical system are given by

$$\mathcal{K} = \frac{1}{2}M\left\|\vec{P}_L\right\|^2 + \frac{1}{2}m\left\|\vec{P}_h\right\|^2 + \frac{1}{2}I_z\vec{\dot{\phi}}^2 + \mathcal{K}_\omega, \tag{A.2a}$$

$$\mathcal{U} = Mg\left(\ell_h + \ell_s + L - \vec{k}\vec{P}_L\right) + mg\left(\ell_h - \vec{k}\vec{P}_h\right) + \frac{1}{2}k_s\phi^2, \tag{A.2b}$$

where $\vec{k}$ represents the unit vector of the vertical z-axis. $\mathcal{K}_\omega$ represents the rotational kinetic energy of the hanging load [147] and can be expressed as

$$\mathcal{K}_\omega = \frac{1}{2}I_x(\dot{\psi}_y)^2(\cos\psi_x)^2 + \frac{1}{2}I_z(\dot{\psi}_y)^2(\sin\psi_x)^2 + \frac{1}{2}I_y(\dot{\psi}_x)^2, \tag{A.3}$$

where I_x, I_y, and I_z are the moments of inertia of the rotation of the cylinder around its three axes.

For the derivation of the equation of motion, the Lagrangian $\mathcal{L}$ is formulated as follows:

$$\frac{\mathrm{d}}{\mathrm{d}t}\left(\frac{\partial\mathcal{L}}{\partial\dot{q}}\right) - \frac{\partial\mathcal{L}}{\partial q} = 0, \text{ and } \vec{q} = \left[\psi, \eta, \zeta, \phi\right]^{\mathrm{T}} \tag{A.4}$$

where $\mathcal{L} = \mathcal{K} - \mathcal{U}$. To simplify the simulation of the system, the following assumptions are made: 1) the cable lengths of the hook (ℓ_h) and sling (ℓ_s) are considered rigid massless elements in the derivation, and 2) the displacements of the hanging components are small compared to the lengths of the pendulum, resulting in the small angle approximation ($\sin(q) \approx q$ and $\cos(q) \approx 1$). With assumptions, evaluating Equation (A.4) gives the following linearized equations of motion (EOMs) of the free vibrations of the dynamical system:

$$\left(\begin{bmatrix} I_y \\ I_x \end{bmatrix} + \frac{ML^2}{4}\right)\begin{bmatrix} \ddot{\psi}_x \\ \ddot{\psi}_y \end{bmatrix} + \frac{ML\ell_h}{2}\begin{bmatrix} \ddot{\eta}_x \\ \ddot{\eta}_y \end{bmatrix} + \frac{ML_{\ell s}}{2}\begin{bmatrix} \ddot{\zeta}_x \\ \ddot{\zeta}_y \end{bmatrix} + \frac{ML}{2}g\begin{bmatrix} \psi_x \\ \psi_y \end{bmatrix} = -\frac{ML}{2}\begin{bmatrix} \ddot{h}_x \\ \ddot{h} y \end{bmatrix}, \tag{A.5a}$$

$$(M+m)\,\ell_h^2\begin{bmatrix} \ddot{\eta}_x \\ \ddot{\eta}_y \end{bmatrix} + M\,\ell_s\ell_h\begin{bmatrix} \ddot{\zeta}_x \\ \ddot{\zeta}_y \end{bmatrix} + \frac{ML\ell_h}{2}\begin{bmatrix} \ddot{\psi}_x \\ \ddot{\psi}_y \end{bmatrix} + (M+m)\,\ell_h\,g\begin{bmatrix} \eta_x \\ \eta_y \end{bmatrix} = -(M+m)\ell_h\begin{bmatrix} \ddot{h}_x \\ \ddot{h}_y \end{bmatrix}, \tag{A.5b}$$

$$M\ell_s^2\begin{bmatrix} \ddot{\zeta}_x \\ \ddot{\zeta}_y \end{bmatrix} + M\,\ell_s\ell_h\begin{bmatrix} \ddot{\eta}_x \\ \ddot{\eta}_y \end{bmatrix} + \frac{ML_c\ell_s}{2}\begin{bmatrix} \ddot{\psi}_x \\ \ddot{\psi}_y \end{bmatrix} + M\,\ell_s\,g\begin{bmatrix} \zeta_x \\ \zeta_y \end{bmatrix} = -M\ell_s\begin{bmatrix} \ddot{h}_x \\ \ddot{h}_y \end{bmatrix}, \tag{A.5c}$$

$$I_z\ddot{\phi} + k_s\phi = 0. \tag{A.5d}$$

B

Linearised magnetically-induced potential energy

The potential energy of the magnetic interaction linearised around the global equilibrium position $\eta = \zeta = \psi = \phi = 0^\circ$ is formulated as

$$W_m = K_1\phi^2 + K_2\phi + K_3\psi^2 + K_4\psi + K_5\eta^2 + K_6\eta + K_7\zeta^2 + K_8\zeta + C, \tag{B.1}$$

where the coefficients are given by

$$\begin{aligned} K_1 = &-\frac{M_{ct_1}M_{t_1}\mu}{4\pi(d_1+h)^5}\left((d_1+h)^2 + 6R(d_1+h) + 6R^2\right) \\ &-\frac{M_{ct_2}M_{t_2}\mu}{4\pi(d_2+h)^5}\left((d_2+h)^2 + 6R(d_2+h) + 6R^2\right) \\ &+\frac{M_{cf}M_f\mu}{4\pi(d_f+h)^5}\left((d_f+h)^2 + 6R(d_f+h) + 6R^2\right) \end{aligned} \tag{B.2a}$$

$$K_2 = \frac{M_{cf}M_f\mu}{4\pi(d_f+h)^4}\sin(\theta)\left(d_f + h + 3R\right) \tag{B.2b}$$

$$K_3 = \frac{M_{ct_1}M_{t_1}\mu}{4\pi(d_1+h)^5}\left(12{n_1}^2{L_c}^2\right) + \frac{M_{ct_2}M_{t_2}\mu}{4\pi(d_2+h)^5}\left(12{n_2}^2{L_c}^2\right) - \frac{M_{cf}M_f\mu}{4\pi(d_f+h)^5}\cos(\theta)\left(3{L_c}^2\right) \tag{B.2c}$$

$$K_4 = -\frac{M_{ct_1}M_{t_1}\mu}{4\pi(d_1+h)^4}(6n_1L_c) - \frac{M_{ct_2}M_{t_2}\mu}{4\pi(d_2+h)^5}(6n_2L_c) + \frac{M_{cf}M_f\mu}{4\pi(d_f+h)^5}\cos(\theta)(3L_c) \tag{B.2d}$$

$$K_5 = \frac{M_{ct_1}M_{t_1}\mu}{4\pi(d_1+h)^5}\left(12{\ell_h}^2\right) + \frac{M_{ct_2}M_{t_2}\mu}{4\pi(d_2+h)^5}\left(12{\ell_h}^2\right) - \frac{M_{cf}M_f\mu}{4\pi(d_f+h)^5}\cos(\theta)\left(12{\ell_h}^2\right) \tag{B.2e}$$

$$K_6 = -\frac{M_{ct_1}M_{t_1}\mu}{4\pi(d_1+h)^4}(6\ell_h) - \frac{M_{ct_2}M_{t_2}\mu}{4\pi(d_2+h)^4}(6\ell_h) + \frac{M_{cf}M_f\mu}{4\pi(d_f+h)^4}\cos(\theta)(6\ell_h) \tag{B.2f}$$

$$K_7 = \frac{M_{ct_1} M_{t_1} \mu}{4\pi(d_1+h)^5}\left(12{\ell_s}^2\right) + \frac{M_{ct_2} M_{t_2} \mu}{4\pi(d_2+h)^5}\left(12{\ell_s}^2\right) - \frac{M_{cf} M_f \mu}{4\pi(d_f+h)^5}\cos(\theta)\left(12{\ell_s}^2\right) \tag{B.2g}$$

$$K_8 = -\frac{M_{ct_1} M_{t_1} \mu}{4\pi(d_1+h)^4}(6\ell_s) - \frac{M_{ct_2} M_{t_2} \mu}{4\pi(d_2+h)^4}(6\ell_s) + \frac{M_{cf} M_f \mu}{4\pi(d_f+h)^4}\cos(\theta)(6\ell_s) \tag{B.2h}$$

$$C = \frac{M_{ct_1} M_{t_1} \mu}{2\pi(d_1+h)^3} + \frac{M_{ct_2} M_{t_2} \mu}{2\pi(d_2+h)^3} - \frac{M_{cf} M_f \mu}{2\pi(d_f+h)^3}\cos(\theta). \tag{B.2i}$$

$$\tag{B.2j}$$

Acknowledgements

The research carried out during a PhD is often sparked by a deep and personal journey of intellectual and introspective discovery. Yet it is never truly a solitary endeavour. I am deeply honoured to acknowledge the special people who have walked beside me through the highs and lows of the past five years and beyond.

My journey began with my mentors, to whom I extend my heartfelt gratitude. To help you, dear reader, visualise the significance of their contributions and the dynamics of our research group, I offer the analogy of a well-known dynamical system: a linear oscillator. Imagine me as a point mass—holding potential for motion, yet initially unaware of it, burdened by the inertia of the familiar and the resistance to change. **Peter**, the restoring spring, endowed the system with its defining characteristics, setting its natural frequency, providing structure, and offering a constant inflow of motivation. **Andrei**, the external excitation force, drove the system forward, fuelling curiosity and intellectual will, at times leading to resonance, moments of amplified motion and discovery. Yet, in instances when oscillations threatened to spiral beyond control, **Apostolos**, the damping device, ensured balance with his valuable and composed guidance, allowing the motion to remain purposeful and centred, leading the overall system to its safe steady-state response. Through their interplay, I experienced both motion and stability, challenge and control—a path that was dynamic yet convergent, leading me ever closer toward a meaningful equilibrium: the dissertation in your hands.

Specifically to you, **Peter**, thank you for being not only my daily supervisor but also a mentor. Your ever-encouraging words and calm demeanour have guided me through every stage of this journey. I deeply admire you—not only as a scientist, with your unquestionably brilliant mind, but also as an individual whom I look up to. As I so often tell you: Well done! You and **Daniëlle** have also brought into the world a tiny kryptonite—my soothing anchor—Prof. dr.ir. **Teije** J. N. Meijers (aka Sobek reincarnated).

Now, I want to address my two paranymphs, who played a pivotal role in my decision to take this leap of faith and embark on this transformative journey. Dr. **Anastasios**, my beloved half in this universe, thank you for relentlessly—if sometimes annoyingly—pushing me to explore. Without you, I would not have dared many things, but most importantly, I would not have had the courage to apply for this position, overcoming the whispers of my inner impostor syndrome. **Dimitra**, my flower, you have been the unexpected kindred spirit I was fortunate to find here in Delft, and I hope we will continue wandering and wondering together throughout our lives. You have guided me in all the right directions, showing me light when I was submerged in pitch-black darkness.

My deepest appreciation goes to my colleagues, who made working in the office a truly wholesome and cosy experience. Especially to my officemates, thank you for the laughter, the light-hearted moments, and the atmosphere filled with memes, vines and lots of teasing—**Jan** (& **Fiona**), **Rens**, and **Shagun**, I am grateful for every shared joke and cheerful exchange. Our adventures in India are most certainly a precious collective memory. To the guest star of our office, always brightening the mood between code runs, **Lukas**, you are a truly inspiring hooman (misspelling very much intended!). I cherished every *moutza* and every emphatic "actually" we shared in the final stretch of this journey. To my wonderful PhD council colleagues, thank you for our insightful meetings and for the shared perspectives and experiences that enriched this journey—**Angeliki**, **Abishek**, **Michele**, **Max**, **Giorgio**, **Jelle**, **Ali**, **Shozab**, **Longge**, **Yuanchen**, and **Enxhi**. Your support and camaraderie are much appreciated. I could not overlook my doctoral sibling, **David**—I deeply treasure our harmonious collaboration and the many insightful brainstorming sessions we had together. I am truly glad I walked a parallel path with you through our PhDs. Thank you once again for sharing our first offshore expedition with me and Peter, and for your thoughtful mentorship as we trekked up to the Ridge in Rocky Mountain National Park.

To some truly special hoomans who entered my life through work, but whose presence extended well beyond it: **Avni** (aka Sunflower), thank you for the beautiful chai and Indian delicacies you lovingly prepared for me, for our deep conversations, our eventful trips, and our not-so-movie nights. Your company, warmth and wisdom have been a gift. **Enxhi** (aka Xhi-xhi), you are a truly lovely, soft-hearted yet resilient hooman. I treasure every dinner (thank you, **Jord**!), sleep-over, temple visit (*de Bijenkorf*), *"për të vuajtur"* trip, and Aperol Spritz we shared. In Delft, I found a little bit of family-I feel truly blessed. **Ina** (aka Kitty Cat), though you're a more recent addition to my life, you've already become a cheeky, lovable golden nugget. You radiate pure cat energy, and I deeply admire both your cognitive and spiritual depth, as well as your calming presence. Thank you for all the things you teach me each day—I genuinely feel so lucky to have met you and **Yosu**. Lovely **Saghy** (aka Sunshine), your presence—gentle yet powerful—is truly remarkable. I cherish every moment of our adventures and explorations across the Netherlands, always accompanied by our inner *Gus-Gus*. I deeply admire your character, your unwavering positivity, emotional intelligence, and kindness.

To my lovely neighbor in Delft, **Konstantinos**—I thoroughly enjoyed our long conversations during our cooking sessions home, brunches at *Tazz*, and even over that unfortunate Peking duck at *Lychee*. You are a truly brilliant all-rounder hooman.

I want to thank my fairy godmother, my psychologist, **Gina**, and my amazing group—**Danai**, **Lefteris**, **Maria**, **Haris**, **Aris** and **Andreas**. Since 2022, you have been a safe space where I can share my honest self, connect, and reflect. Your precious personalities nourish my idealistic heart, and for that, I am endlessly grateful.

To three wonderful hoomans with whom I've already shared so much of my life—and who have stood by me through thick and thin: **Olympia**, my red-haired twin (physical, not digital); fellow **Panagiota** (π^2); and the sugar-coated (a mommy already!) **Elena**—you (& the little families you have built) are my sweet haven. Your friendship and love is truly a precious personal treasure. I can't wait to see what the future has in store for us and the beautiful adventures and stories we will unravel together.

Lastly, to my family, for giving me the opportunity to pursue my dreams, for believing in me more than anyone, and for teaching me the true meaning of love and kindness. Σας αγαπώ άπειρα, and I hope to make you as proud as you continuously make me. To my father, **Giorgos**, my mother, **Despoina**, my grandpa, **Tasos**, and my grandma, **Panagiota**, and my beloved godson, **Stylianos**, and his amazing family, **Marios**, **Vassilis**, and **Eleni**. You mean the world to me—the sun to my solar system.

Με πολλή αγάπη,
Γιούλη

Curriculum Vitæ

Panagiota Atzampou

18-11-1995 Born in Athens, Greece

Academic Experience

2013–2018 Diploma of Civil Engineering (MEng.)
University of Patras, Greece
Thesis: Structural analysis, assessment and retrofitting of a R/C building using Fiber Reinforced Polymers (FRP).
Supervisor: Prof. dr. A. Triantafillou

2018–2020 Master in Water Resources Science & Technology (MSc.)
National Technical University of Athens, Greece
Thesis: Wave-current interaction in 3rd generation spectral numerical model.
Supervisor: Prof. dr. V. Tsoukala

2020–2025 Ph.D. Research
Delft University of Technology, the Netherlands
Thesis: Contactless position control of offshore wind turbines during installation.
Promotor: Prof. dr. A.V. Metrikine & Dr. ir. A. Tsouvalas
Copromotor: Dr. ir. P.C. Meijers

2025– Post-doctoral Research
Delft University of Technology, the Netherlands

Work Experience

2019–2020 Civil Engineer Internship
ECOS Consulting S.A., Athens, Greece

List of Publications

Journal publications

🗎 3. **P. Atzampou**, P. C. Meijers, A. Tsouvalas, and A. V. Metrikine, “Non-contact electromagnetic control of torsional vibrations of a rigid cylinder,” *Nonlinear Dynamics*, vol. 113no. 3, pp. 2001–2016, 2025

🗎 2. D. F. Domingos, **P. Atzampou**, P. C. Meijers, S. H. Beirão, A. V. Metrikine, J.-W. van Wingerden, and P. Wellens, “Full-scale measurements and analysis of the floating installation of an offshore wind turbine tower,” *Ocean Engineering*, vol. 310, p. 118 670, 2024, (Awarded TUDelft *Best Wind Energy Paper* of 2024)

🗎 1. **P. Atzampou**, P. C. Meijers, A. Tsouvalas, and A. V. Metrikine, “Contactless control of suspended loads for offshore installations: Proof of concept using magnetic interaction,” *Journal of Sound and Vibration*, vol. 575, p. 118 246, 2024

Conference publications

🗎 4. **P. Atzampou**, P. C. Meijers, A. Tsouvalas, and A. V. Metrikine, “Magnetic control of translational and torsional motions of suspended loads,” *International Conference in Experimental Vibration Analysis for Civil Engineering Structures*, 2025

🗎 3. **P. Atzampou**, P. Meijers, A. Tsouvalas, and A. Metrikine, “Magnetic control of a simple pendulum with a moving pivot point,” *Journal of Physics: Conference Series*, vol. 26473, p. 032 010, 2024

🗎 2. P. C. Meijers, **P. Atzampou**, and A. V. Metrikine, “Experimental and numerical study of a magnetic pendulum,” *International Conference on Nonlinear Dynamics and Applications*, pp. 703–712, 2023

🗎 1. **P. Atzampou**, P. Meijers, A. Tsouvalas, and A. Metrikine, “Motion Control of a Pendulum via Magnetic Interaction,” *International Conference on Nonlinear Dynamics and Applications*, pp. 49–59, 2023

Book chapters

🗎 1. **P. Atzampou**, P. C. Meijers, A. Tsouvalas, and A. V. Metrikine, “Motion Control of Suspended Loads via Magnetic Interaction,” *Nonlinear Systems - Practical Applications and Contemporary Challenges*, 2025, (soon to be published)